UNIVERSITY OF OKLAHOMA

GRADUATE COLLEGE

SEISMIC ATTRIBUTE EXPRESSION OF FLUVIAL-DELTAIC AND TURBIDITE SYSTEMS

A DISSERTATION

SUBMITTED TO THE GRADUATE FACULTY

in partial fulfillment of the requirements for the

Degree of

DOCTOR OF PHILOSOPHY

By

BRADLEY C. WALLET
Norman, Oklahoma
2014

Downloaded from SHAREOK. Persistent Handle URL: https://hdl.handle.net/11244/13877

SEISMIC ATTRIBUTE EXPRESSION OF FLUVIAL-DELTAIC AND TURBIDITE SYSTEMS

A DISSERTATION APPROVED FOR THE
CONOCOPHILLIPS SCHOOL OF GEOLOGY AND GEOPHYSICS

BY

Prof. Kurt J. Marfurt, Chair

Dean Larry Grillot

Prof. Roger Slatt

Dr. Deepak Devegowda

Dr. Sergio Chávez-Pérez

© Copyright by BRADLEY C. WALLET 2014
All Rights Reserved.

I would like to dedicate this dissertation to daughter, Philippa (Pippi) Marie Deacon Wallet, and my spouse, Dr. Zermarie Deacon. They made me rethink everything about my world.

Contents

List of Tables **vii**

List of Figures **xvi**

Abstract **xvii**

1 Introduction **1**

2 Integrating Phase into the Interpretation of Spectral Decomposition Attributes **4**

2.1 Introduction 4

2.2 Geological background 6

2.3 Visualization 9

2.4 Interpreting phase and magnitude 14

2.5 Principal Component Analysis (PCA) 25

2.6 Statistical analysis of PCA 29

2.7 Conclusions 32

3 Using the Image Grand Tour to Visualize Fluvial Deltiac Architectural Elements in South Texas, USA **35**

3.1 Introduction 36

3.2 Methodology 38

3.2.1 Principal Component Analysis (PCA) 38

3.2.2 The Grand Tour 42

3.2.3 Image Grand Tour (IGT) 44
3.2.4 The View Locked Color Image Grand Tour (VLCIGT) 46
3.3 Application 47
3.3.1 Study area 47
3.3.2 Results 48
3.4 Limitations 50
3.5 Conclusions 50

4 Latent Space Modeling of Seismic Data: An Overview 60

4.1 Introduction 60
4.2 Self Organizing Maps 63
4.3 Generative Topological Maps 64
4.4 Diffusion Maps 65
4.5 Application 66
4.6 Conclusions 67

5 Attribute expression of channel-forms in a hybrid carbonate turbidite formation 75

5.1 Introduction 75
5.2 Geological and geophysical background 81
5.2.1 Regional geology 81
5.2.2 Data description 84
5.3 Seismic interpretation and 3D geomodeling 87
5.4 Seismic expression of channel-forms 87
5.4.1 Single attribute analysis 88
5.5 Geobody extraction 108

5.6 Conclusions 118

6 Conclusions **120**

Bibliography **124**

A The Curse of Dimensionality **128**

A.1 Geometric Analogy 128

A.2 Practical Implications 131

B Visualization of High Dimensional Data **132**

B.1 Cross plots 132

B.2 Parallel coordinates 132

B.3 Andrews' curves 134

B.4 Chernoff faces 135

B.5 Summary 136

List of Tables

2.1 Correlation between spectral components based upon Pearson's linear coefficient. 32

List of Figures

2.1 Well cross sections across the Red Fork showing the relative locations and the complexity of the various stages of events. 7

2.2 Location of the survey used in this work as well the previous interpretation 8

2.3 Phantom horizon slice of the seismic amplitude volume taken 90 ms below the Pink Lime horizon. Seismic data is courtesy of CGG Veritas. 9

2.4 Phantom horizon slice of the spectral magnitude volumes taken 90 ms below the Pink Lime horizon. 11

2.5 Phantom horizon slice of the spectral phase volumes taken 90 ms below the Pink Lime horizon. 12

2.6 HSV is a cylindrical-coordinate color representation model. Hue represents a pure color about the cylinder. Saturation represents a purity of color ranging from white to a pure color. Value represents an illumination from black to a bright color. (Wikimedia Commons) 13

2.7 Phantom horizon slice of the spectral magnitude and phase volumes taken 90 milliseconds below the Pink Lime horizon displayed using a HSV color map. Phase is displayed as hue while amplitude is displayed using the value channel. 15

2.8 Phantom horizon slice of the spectral magnitude and phase volumes taken 90 milliseconds below the Pink Lime horizon displayed using a HSV color map. Phase is displayed as hue while amplitude is displayed using the value channel. Saturation is set to a constant value of 0.5 to provide a more pastel image. 16

2.9 Peyton interpreted five stages of flooding and incision as shown in this Figure. These interpretations are overlain upon a 36 Hz spectral magnitude image. 17

2.10 10 Hz spectral phase and magnitude using a HSV color map for the phantom horizon taken 90 ms below the Pink Lime. Only broad features are visible, and considerable noise is evident in this image. . . . 18

2.11 20 Hz spectral phase and magnitude using a HSV color map for the phantom horizon taken 90 ms below the Pink Lime. Significant details are visible of the unknown stage, denoted by the red arrows. The white arrows highlight a number of meandering channels, and the black arrows show what appears to be oxbows and abandonment channels. 19

2.12 30 Hz spectral phase and magnitude using a HSV color map for the phantom horizon taken 90 ms below the Pink Lime. Increasing levels of detail are visible compared to the previous figures. The red arrows show areas of increasing detail in fine channel structure. The white arrows show what appears to be regional Red Fork channel bars or reefs. 20

2.13 40 Hz spectral phase and magnitude using a HSV color map for the phantom horizon taken 90 ms below the Pink Lime. Increasing frequency continues to provide increasing detail in the architectural elements. Interestingly, improved vertical resolution seems to lead to improved horizontal resolution. The unknown stage (white arrow) is seen in very high detail showing complexity not show by previous work. Stage 5, as shown by the red arrow is better defined in this image as well. 21

2.14 50 Hz spectral phase and magnitude using a HSV color map for the phantom horizon taken 90 ms below the Pink Lime. Stage 2 and 3 are well differentiated to the southwest (red arrow) while the unknown stage is better differentiated to the northeast (white arrow). 22

2.15 60 Hz spectral phase and magnitude using a HSV color map for the phantom horizon taken 90 ms below the Pink Lime. Many channel like features are well defined in this view as shown by the white arrows. . 23

2.16 70 Hz spectral phase and magnitude using a HSV color map for the phantom horizon taken 90 ms below the Pink Lime. Strong noise is becoming apparent. However, many small channel features are now visible as shown by the white arrows. 24

2.17 Phantom horizon slice of the spectral magnitude volumes with 20 Hertz displayed as red, 40 Hertz displayed as green, and 60 Hertz displayed as blue. 25

2.18 Horizon slices of the principal components of spectral phase and magnitude components. 27

2.19 Eigenvalue plot for the PCA of the complex spectral components. This suggests no information past the fourth principal component. 28

2.20 HSV plot of the phase and magnitude of the first principal component. Most of the architectural elements present in the spectral components are visible. The red arrows show the unknown stage. The blue arrow shows stage five. The white arrows a number of small meandering channels. The black arrows show abandonment channels. The cyan arrow shows separation between stage two and three. The green arrows show small, channel like features. The gold arrow shows stage one. . . 29

2.21 HSV plot of the phase and magnitude of the second principal component. The white arrow shows improved views of channels and channel like features over the first principal component. The red arrow highlights detail of the unknown stage that was not visible in the previous image. 30

2.22 Tenth principal component is very noisy as we would expect. However, considerable spatial patterns are still visible including interpretable features. The white arrow shows a channel like feature that was not visible in the first two principal components. 31

3.1 Four images representing four different spatial processes. The grayscale levels for all four images have similar ranges and thus would not be sufficient to separate these images if they were mixed. 40

3.2 Six simulated attributes created by random linear combinations of the images 41

3.3 Six principal components from the attributes shown. None of these images is well suited to recover the original images. Note that the sixth pc has more information from an interpretation standpoint than either the fourth or fifth pc. 42

3.4 In three dimensions, a donut is a torus. 43

3.5 A photograph consists of three input layers, representing the colors red, green, and blue (middle). For the typical color rendition, these layers are equally weighted and displayed in the RGB color space (left). In the IGT, the three layers obtain different weighting at each step of the tour and are projected into a one-dimensional gray-scale color space (right). This image was previously published and is republished with permission. 45

3.6 A horizon slice of the seismic data used in this study. Note the significant presence of channels including a prominent set of channels from the evolution of a meandering channel in the southwest portion of the image. 52

3.7 A representative view of a channel in the data set demonstrating the relatively poor data quality. 53

3.8 Two canonical attributes to establish a baseline of performance.(a) shows coherence while (b) shows the SRGB attributes. Both images shows some evidence of channels though the systems are like clearly evident. Furthermore, coherence appears heavily corrupted by the presence of acquisition footprint. 54

3.9 Horizon slices through eight spectral component volumes. Images indicate a large number of channels. Some of the information in the different images is likely redundant while other information may be complementary. Additionally, heavy aquisition footprint is quite evident throughout the images. 55

3.10 False color image composed of the first three principal components. Two large channels are indicated by the red and green arrows. Several smaller channels are indicated by the yellow arrows. Strong acquisition footprint is evident in the NS stripping across the image. 56

3.11 This grayscale image was discovered using the IGT. Note that all structure visible in the false color PCA image is visible in this single component image. The red arrows denote channels that are much more clearly imaged than previously. 57

3.12 This image resulted from continuing to run the IGT with the red channel fixed on the previously discovered image. Distinct channel structure, denoted by the yellow arrows, was found overlaying the previously known major channels. 58

3.13 Continuing to run the IGT with the red and the green channels fixed uncovered other, more subtle structure. In this view, small channels denoted by the yellow arrows are clearly seen. 59

4.1 This figure shows a pedagogical example of a one dimensional latent space manifold embedded in two dimensions. Note that while points A and B are relatively close in Euclidean distance in the attribute space, they are extremely distant when mapped into the latent space as points A' and B'. The green curve represents a possible latent space that might explain this data set. A point distant from this green line would be of very low probability and would be considered implausible. 69

4.2 Seismic waveforms (or vectors) representing two points in the set of possible seismic waveforms of 16 samples in length. The blue segment is taken from the real data set and is entirely plausible while the red segment is artificially created and is highly improbable. 70

4.3 Seismic data that were modeled using SOM and GTM. (a) Vertical section through the seismic data flattened on the continuous Pink Lime horizon. The interval denoted by the yellow lines shows the extent of the waveforms we modeled. (b) Phantom horizon slice 60 ms below the Pink Lime. This represents the tops of the modeled waveforms. . 71

4.4 The survey area corresponding to the seismic data modeled in this paper contains a series of incised channels with varying characteristics. These channels have been previously mapped using a combination of well logs, seismic interpretation, and seismic attribute analysis. 72

4.5 Images related to running SOM upon the data set. The new images agree with the previous interpretation while providing additional richness that promises to aid in future analysis. Additionally, the black arrows denote what we interpret to be a fan feature not previously seen. (a) The output a SOM with the latent space mapped vectors displayed as an image. (b) The SOM image blended with a coherency image. (c) The interpretation overlain on the SOM image. (d) The color map used in the display of the SOM image. Each hexagon represents a cluster with images (a) through (c) being colored with this color map. 73

4.6 Images related to running GTM upon the data set. The new images agree with the previous interpretation while providing additional richness that promises to aid in future analysis. Additionally, the black arrows denote what we interpret to be a fan feature not previously seen. (a) The output a GTM with the latent space mapped vectors displayed as an image. (b) The GTM image blended with a coherency image. (c) The interpretation overlain on the GTM image. (d) The color map used in the display of the SOM image. Each dot represents a cluster with the latent space thus expressed in a discrete two dimensional space 74

5.1 A vertical slice through the seismic data volume taken parallel to the paleo-shoreface. Evidence of channel-forms is clearly seen in this image. 77

5.2 A partial interpretation overlayed on the vertical slice. The green arrows denote the channel-forms in the prograding carbonates. 78

5.3 A vertical slice through the seismic data volume taken perpendicular to the paleo-shoreface. An experienced interpreter can glean considerable information regarding global eustatic sea levels from this view, but it does not clearly map the channel forms and other architectural elements of the turbidite system. 79

5.4 A vertical slice through the seismic data volume taken perpendicular to the paleo-shoreface with an interpretation overlain. Blues indicate the tops of high-stand events. Greens indication the tops of transgressive events. Reds indicate the tops of low-stand events. 80

5.5 Location of the Carnarvon Basin along the coast and offshore of Western Australia. ©Commonwealth of Australia (Geoscience Australia). Used with permission. 81

5.6 Relative sea level curve for the Rankin Platform from the Oligocene to the present. 82

5.7 Bypass margins are believed to form turbidity flows during low-stand events. a) Transgressive-stand event. b) High-stand event. c) Low-stand event. d) Drowning unconformity. 83

5.8 One modern analog for the Mandu Formation can be found on the Little Bahama Bank. Bypass margin slopes in this zone exhibit a similar channel-form architecture. 84

5.9 A modern analog for the Mandu Formation that is currently experiencing sub-aerial exposure is the Florida Keys, Florida USA. Similar channel-form architecture is readily visible in aerial images. (Courtesy of Google Earth ™.) 85

5.10 The location of the Rosie 3D survey that is used in this study. 86

5.11 Three distinct sets of channel forms are apparent in the data set. Approximate locations of these sets are designated by the blue lines. . . 89

5.12 The green line shows the horizon I interpreted to flatten the data volume for this study. 91

5.13 This is the flattened version of the data that was used in this study. . 92

5.14 Zooming in on a channel-form yields considerable information about the morphology of the features. Reflectors associated with the channel-forms tend to converge out toward the edges inside the channel-form (blue arrow) and in toward the edges outside the channel-form (red arrow). Also, there are considerable numbers of discontinuities associated with the channel-forms (green arrow). The overall shape of the channel-forms is concave as shown by the yellow line. 93

5.15 Phantom horizon slice through the seismic amplitude volume 52 ms above the flattening (green) horizon. The channel-forms are meandering in this horizon. I interpret this as being before the carbonate reef prograded into the region. 94

5.16 Phantom horizon slice through the seismic amplitude volume 152 ms above the flattening (green) horizon. The channel-forms are straighter and wider than they were at the shallower horizon corresponding to their deeper incisement. 95

5.17 Phantom horizon slice through the seismic amplitude volume 352 ms above the flattening (green) horizon. The extent and edges channel-forms are more difficult to interpret in this horizon as they are cutting through the internal geometry of the carbonates at a much higher angle. 96

5.18 The variance attribute for a vertical line. The expression of the channels is readily apparent, but edges are not clear. The image has a generally "blurry" appearance. 98

5.19 The variance attribute zoomed in upon a channel-form. Some boundaries are highlighted (green arrows) while others are not (red arrow). The bottom of the channel-form, however, is not highlighted (black arrow). 99

5.20 Variance attribute for 52 ms above the flattening horizon. 100

5.21 Variance for 152 ms above the flattening horizon. 101

5.22 Variance attribute for 352 ms above the flattening horizon. 102

5.23 K2 principal curvature for a vertical. Highly negative values appear to follow the centers of the channel-forms, but they do not appear to fully cover the lateral crosswise extent. 103

5.24 Most negative curvature zoomed in upon a channel-form. Highly negative values of k2 characterize the vertical extend of the channel-form, they do not reach the full lateral extent as shown by the green arrows. 104

5.25 K2 principal curvature for 52 ms above the flattening horizon. Highly negative values appear to map out the channel-forms. 105

5.26 K2 principal curvature for 152 ms above the flattening horizon. Highly negative values appear to map out the channel-forms. 106

5.27 K2 principal curvature for 352 ms above the flattening horizon. Highly negative values appear to map out the channel-forms. 107

5.28 Reflector convergence azimuth and magnitude for a vertical line. The reflectors converge on the edges of the channel-forms as well as the flanks. 109

5.29 Reflector convergence azimuth and magnitude for a zoomed portion of a vertical line. Green arrows denote the convergence associated with the edges of the channel-forms. Red arrows show the convergence associated with the flanks. 110

5.30 Reflectors on the flanks of an incised channel-form will tend to converge toward the edges. 111

5.31 A typical geobody extraction work-flow. 112

5.32 A spatial operator with a half wavelength of 600 m. 113

5.33 k2 curvature calculated using a spatial operator designed for 600 m wide features calculated for the extent of the Mandu formation. Highly negative values of k2 do a much better job of extending across the full lateral extent of the channel-forms. Note that several of the "interfluvials" or regions between the channel-forms have a dome shape which gives rise to a positive value (red) for k2. 114

5.34 In the thresholding process, highly negative values of k2 curvature are assumed to correspond with the channel-forms. 115

5.35 Values of k2 curvature below the selected threshold are candidates for inclusion in the geobody being extracted. 116

5.36 Extracted geobodies for the channel-forms modeled using k2 curvature. The results appear to be geologically feasible. 117

5.37 Extracted geobodies overlain on the seismic amplitude data. 118

A.1 A two-dimensional example of a hypersphere circumscribed within a hypercube. Any space within the hypercube that is not also within the hypersphere is contained within the corner regions. 129

A.2 A two-dimensional example of a hypersphere contained within a hypersphere of ϵ larger radius. Any space within the larger hypersphere that is not also within the smaller hypersphere is contained within within a thin shell. 131

B.1 A pairs plot shows all scatter or crossplots of all attributes displayed pair-wise. The center axis shows the histogram of the individual attributes. In this particular case, the data are fourdimensional with three classes. Color denotes class membership. 133

B.2 A parallel coordinates plot makes the axes parallel instead of orthogonal. Each observation is thus encoded as a piecewise linear curve. In this particular case, the data are four dimensional with three classes. Color denotes class membership. 134

B.3 Andrews curves encode multidimensional attributes as the coefficients of a Fourier series. In this particular case, the data are four dimensional with three classes. Color denotes class membership. 135

B.4 Chernoff faces plots encode each d-dimensional observation as a face with each of d attributions defining the shape or size of a particular feature of the face. 136

Abstract

Much of the world's conventional oil and gas production comes from fluvial deltaic and turbidite reservoirs. The ability to accurately interpret the architectural elements comprising these systems greatly reduces the risk in exploration and development in these environments. In addition to clastic environments, turbidites can also occur in carbonate environments, and formations of this type pose significant unanswered questions.

In this dissertation, I demonstrate methods for using attributes to improve the interpretation in fluvial deltaic using data from Middle Pennsylvanian age Red Fork Formation of Oklahoma and the Oligecene-Miocene age Frio Formation of south Texas. I show how spectral phase and magnitude attributes can be effectively combined using an HSV color map to produce images that have considerable interpretational value. I develop an interactive method using the skill of the interpreter to blend attributes dynamically. I also apply a statistical technique to integrate multiple attributes in a non-linear manner. Incorporating my methods in the interpretation process has the potential to improve the exploration and development in these systems.

I also look at the problem of mapping channel-forms the hybrid carbonate turbidite Oliogence age Mandu Formation in the Carnarvon Basin of Australia. I show how attributes tie to the geological features of the architectural elements. I demonstrate the capability to extract in 3-D the associated channel-forms. Further analysis using these methods has the potential to increase our understanding of how turbidites form in carbonate environments.

CHAPTER 1

Introduction

Seismic geomorpholgy is the study of buried rock formations by applying techniques typically used for remote sensing of modern land-form features. When combined with attribute analysis, seismic geomorphology implies the choice of views and attributes that make the past resemble the present in such a way that an interpreter can recognize architectural elements based upon the view presented. The goal is thus to present the data to the interpreter in the manner that best harnesses her expertise, experience, and talents.

Fluvial deltaic and turbidite systems particularly lend themselves to seismic geomorphological analysis. This is due to the large scale structures and their characteristic shapes. Rivers, streams, and other channel forming landscape elements are a common element of human society, and we are accustomed to their nature. As such, interpreters generally feel "comfortable" with visualizing channels, and considerable literature has been devoted to the seismic geomorphology of channelized systems (Bahorich et al., 2002; Coléou et al., 2003; Davogustto et al., 2013; Guo et al., 2006; Liu and Marfurt, 2007a; Partyka et al., 1999; Suarez et al., 2008; Wallet, 2013).

Key to this form of analysis is finding the right attribute to properly highlight the channels. A good attribute for visualization is one that presents the data in such a way that the interpreter can distinguish geologically reasonable geometries and interpret them effectively. Spectral decomposition (Liu and Marfurt, 2005; Castagna

and Sun, 2006) has been a common attribute used for this purpose. However, the high dimensional nature of spectral decomposition attributes present challenges as to their proper application (Guo et al., 2006). Furthermore, spectral decomposition results in both amplitude and phase information, but interpreters generally disregard the phase components.

My goal in writing this dissertation is to look at methods for dealing with these issues surrounding the visualization of spectral decomposition information. Additionally, I look at other attributes that are useful in the visualization of channels. Much of the focus of this dissertation is around the theme of "too many attributes" and how to select or combine them, and I use both objective and subjective approaches to this problem. I present this work in the form a series of scientific papers detailing the techniques I have developed or applied.

Chapter 2 looks as an innovated color mapping approach to the simultaneous visualization of both phase and magnitude. This chapter will be modify for submission to *Interpretation*.

Chapter 3 details an interactive technique for visualizing multiple attributes to construct interpretationally "interesting" images. This paper was previously published in *Interpretation* (Wallet, 2013).

Chapter 4 examines a method for combining multiple attributes using statistical based latent space learning. This paper was previously published in *The Leading Edge* (Wallet et al., 2009).

Chapter 5 examines the seismic attribute expression of a hybrid carbonate turbidite system. I further examine suitability of these attributes for 3-D geomodeling, and I used curvature to construct a 3-D model of the associated channel-forms. This chapter will be modify for submission to *Interpretation*.

Finally, chapter 6 details my conclusions drawn from this work, and I give recommendations for the further exploration of these topics.

At the conclusion of this dissertation, there are two appendices. Appendix A discusses mathematical considerations involved in working with higher dimensional data. It provides additional motivation to the dimensionality reduction focus of much of this dissertation. Appendix B discusses other techniques for visualizing multi-dimensional data. Both appendices were previously published in Wallet (2013).

Ceterum autem censeo Carthaginem esse delendam.

CHAPTER 2

Integrating Phase into the Interpretation of Spectral Decomposition Attributes

2.1 Introduction

Since it is sensitive to changes in thickness and velocity, spectral decomposition of seismic amplitude data has proven to be a powerful tool for tasks such as mapping channels, submarine fans, and other sedimentary features (Wallet, 2008). In the spectral decomposition process, a seismic amplitude trace is decomposed into time varying, localized frequency information. This process can be achieved by a number of means including the Discrete Fourier Transform (Partyka et al., 1999), continuous wavelet transform (Stockwell et al., 1997), and matching pursuit (Castagna et al., 2003; Liu and Marfurt, 2005). Each of these approaches has strengths and weaknesses based upon the desired application, and a number of papers have compared their relative merits (Castagna and Sun, 2006; Leppard et al., 2010).

In a typical application, an interpreter will generate a moderate to a large number of spectral attribute volumes. For instance, if an interpreter calculates components for 10 Hz - 100 Hz in one Hertz increments, the resultant data set contains 91 complex spectral components composed of frequency f, spectral magnitude (A_f) and phase (ϕ_f) components can be generated. This large amount of resultant data presents considerable challenges in terms of data management and visualization. Historically, an

interpreter would display a single magnitude component as a horizon slice, scrolling through frequencies to select the frequency that appeared to best delineate the architectural elements of interest. A number of differing approaches have been proposed in recent years to deal with this large amount of data. Guo et al. (2006) used principal component analysis (PCA) to reduce the dimensionality of the data. Wallet (2008, 2013) developed an interactive technique for searching for more optimal linear combinations of spectral components. Other possible approaches include Self Organizing Maps (SOM) (Kohonen, 2001), Generative Topographical Maps (GTM) (Bishop et al., 1998; Wallet et al., 2009), and Diffusion Maps (Wallet et al., 2009).

Thus far, most interpreters have focused upon using just the magnitude component from the spectral decomposition process. This is largely due to the well understood relationship between spectral magnitude and tuning effects of feature thickness. In contrast, phase information is generally underutilized despite the fact that phases can contain valuable information such as fault edges.

Incorporating phase information in the analysis and interpretation of spectral decomposition information presents a number of challenges. One challenge is understanding the relative relationship between the magnitude and phase information. Should they be considered separately or in tandem? Are they covariant or orthogonal in the information they represent?

Additionally, phase is circular in nature, typically represented as $-\pi < \phi \leq \pi$. In our analysis, we typically consider them as a 2-tuple, $\psi = (A, \phi)$. This is because of our desire to directly work with interpreting A and our attempts to interpret with φ Wallet et al. (2012) or as a complex number $\zeta = Ae^{i\varphi}$? What methods can be used to co-visualize magnitude and phase information as an image to allow for spatially oriented interpretation?

In this paper, I examine the above issues related to the integration of phase information into the analysis of spectral decomposition data using the data set from the Anadarko Basin, Oklahoma. Firstly, I briefly discuss the formation of interest. Then, I consider various display schemes including method for co-visualizing magnitude and phase information using a hue-saturation-value colormap. I further consider the visualization of spectral decomposition information combined with Principal Component Analysis (PCA). Next, I do statistical analysis of the results of PCA and show quantitatively that we do not achieve the informational independence we might naïvely expect. This an issue that I more fully explore in Wallet (2013). Finally, I summarize my findings and make suggestions for future work based upon my results.

2.2 Geological background

My study area is located in the Anadarko Basin, Oklahoma USA. The Middle Pennsylvania age Red Fork formation is an important gas producer in this region. The stratigraphy in this formation consists of fluvial deltaic architectural elements comprising of five stages of incisions which occurred during successive low-stand events. The channels and valleys have complicated and varying infill that results in significant differences in their spectral responses. The relative relationship of these events are shown in Figure 2.1.

The survey used in this paper involves the merge and reprocessing of surveys used in multiple previous studies including Peyton et al. (1998), Davogustto et al. (2013), Wallet et al. (2009), and Del Moro et al. (2013).

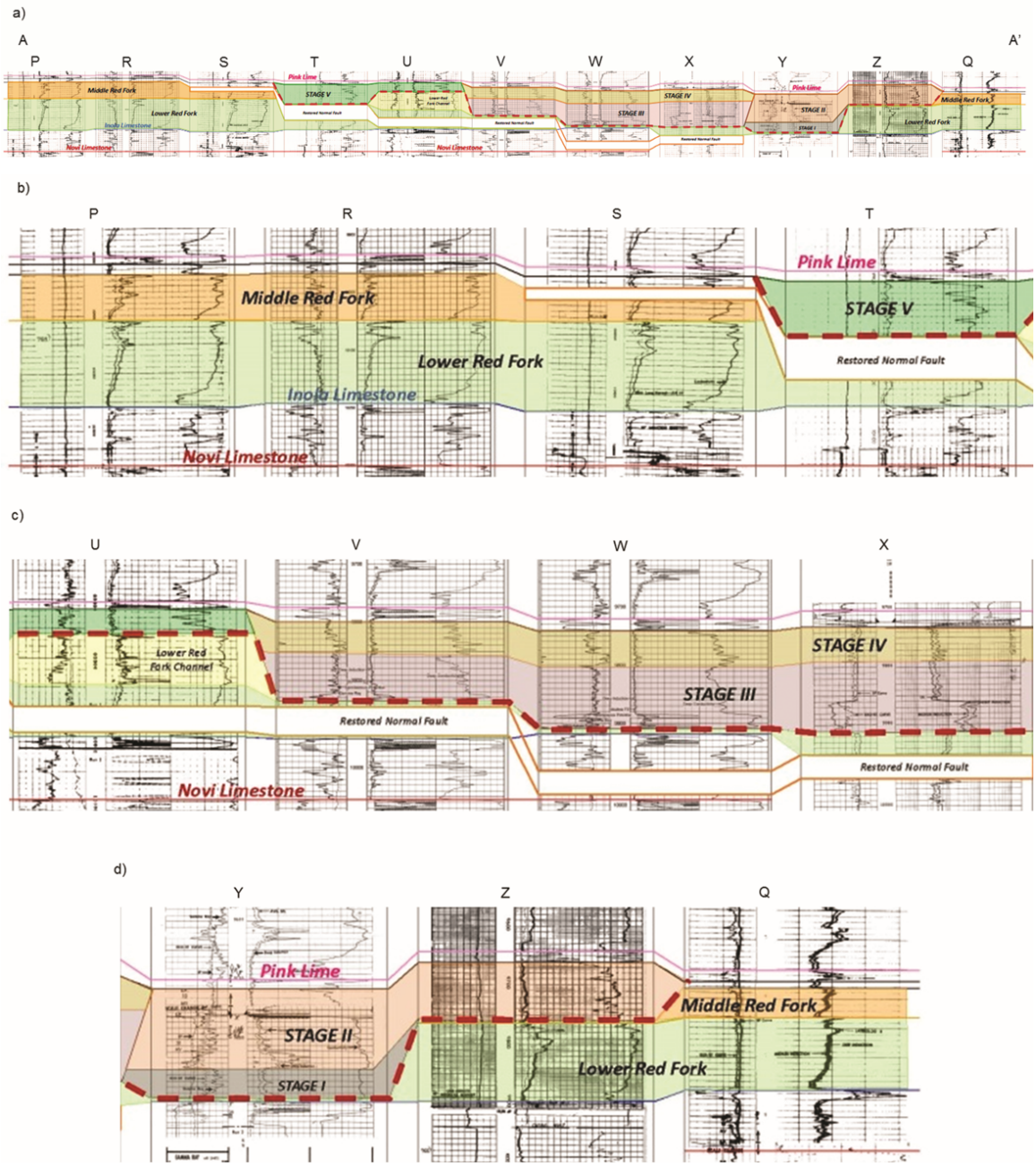


Figure 2.1: Well cross sections across the Red Fork showing the relative locations and the complexity of the various stages of events. (Davogustto et al., 2013)

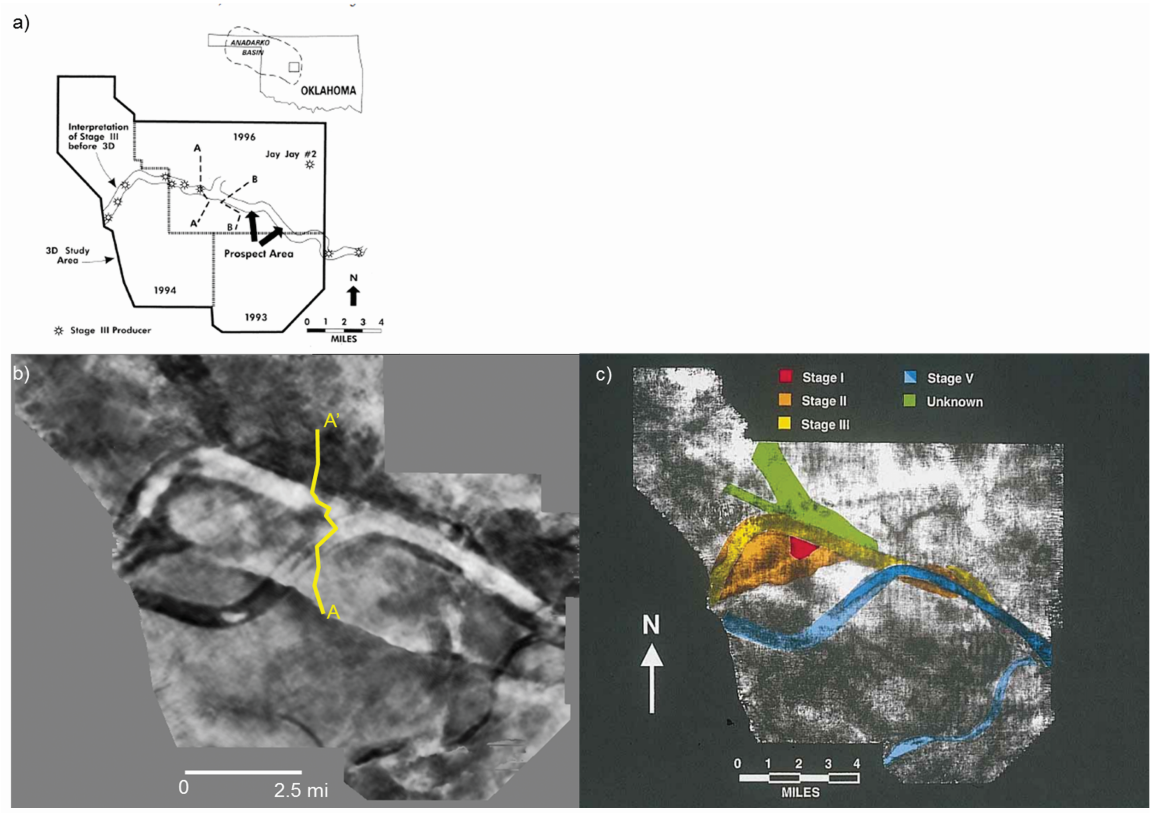


Figure 2.2: Location of the survey used in this work as well the previous interpretation from Peyton et al. (1998).

2.3 Visualization

For the purposes of this study, I calculated spectral magnitude and phase information for the Boilermaker survey previously described by Del Moro et al. (2013) using the Attribute Assisted Seismic Processing and Interpretation (AASPI) software suite (Davogustto et al., 2011). Using this software, I calculated ten spectral magnitude and phase volumes from 10 Hz to 100 Hz in 10 Hz increments. I then flattened the volumes based upon an interpretation of the Pink Lime horizon, and I extracted spectral information for a phantom horizon located 90 ms below the Pink Lime. The seismic amplitude associated with this horizon is shown in Figure 2.3.

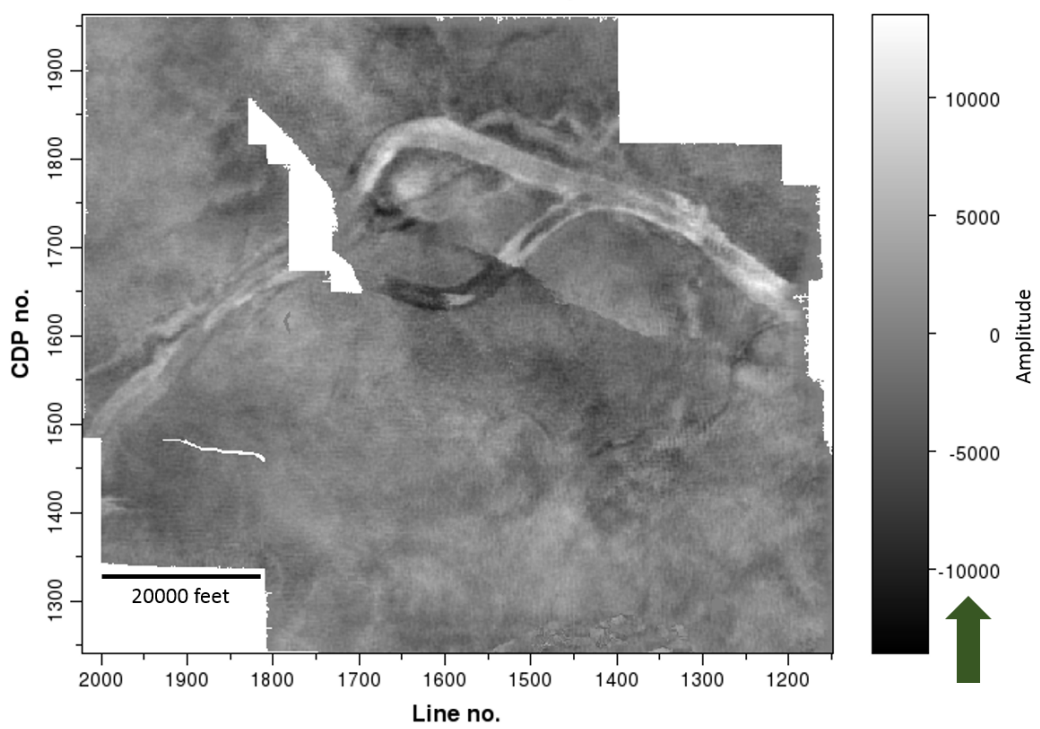


Figure 2.3: Phantom horizon slice of the seismic amplitude volume taken 90 ms below the Pink Lime horizon. Seismic data is courtesy of CGG Veritas.

Figure 2.4 shows the spectral magnitude components associated with this horizon slice. Note that there appears to be a considerable amount of redundant information

between frequencies. Figure 2.5 shows the related spectral phase components. Since phase information is circular, I have used a cyclical color map to display phase to allow for the wrapping values.

Both the spectral magnitude and phase volumes appear to present considerable information. Co-visualizing these attributes can be accomplished using an HSV colormap (Figure 2.6). The HSV color model is an alternative conceptual color space to the commonly used RGB model. In the RGB model, colors are decomposed into three values representing human color perceptions of light spectra corresponding to red, green, and blue. The RGB color model thus arises from a biological model of three sets of spectrum-specific detectors (cones) in the typical human eye.

The HSV color model can be considered a reorganization of the RGB color model. An HSV color model consists of three components: hue, saturation, and value (or brightness). Hue appears as a periodic value displayed about a color wheel. Saturation appears as a purity of color: completely saturated points are pure colors, less-saturated values appear pastel, and completely unsaturated points appear white under full brightness. Brightness appears as the amount of illumination of the colors. Lower brightness points are dimmer and points of zero brightness are black. A cylindrical representation of the HSV color space is shown in Figure 3.

Wallet et al. (2011) recently demonstrated how an HSV colormap can be used to effectively display two attributes where one attribute is circular and the other attribute is a magnitude related to the first one. Since spectral phase is circular, hue is the obvious choice for displaying this information. The choice as to whether to use saturation or value to represent spectral magnitude is subjective though my experience suggests that in this case, value is the better choice. Experientially, I believe interpreters are better at judging subtle differences in value than saturation. The resultant images of this display are shown in Figure 2.7. My experience has

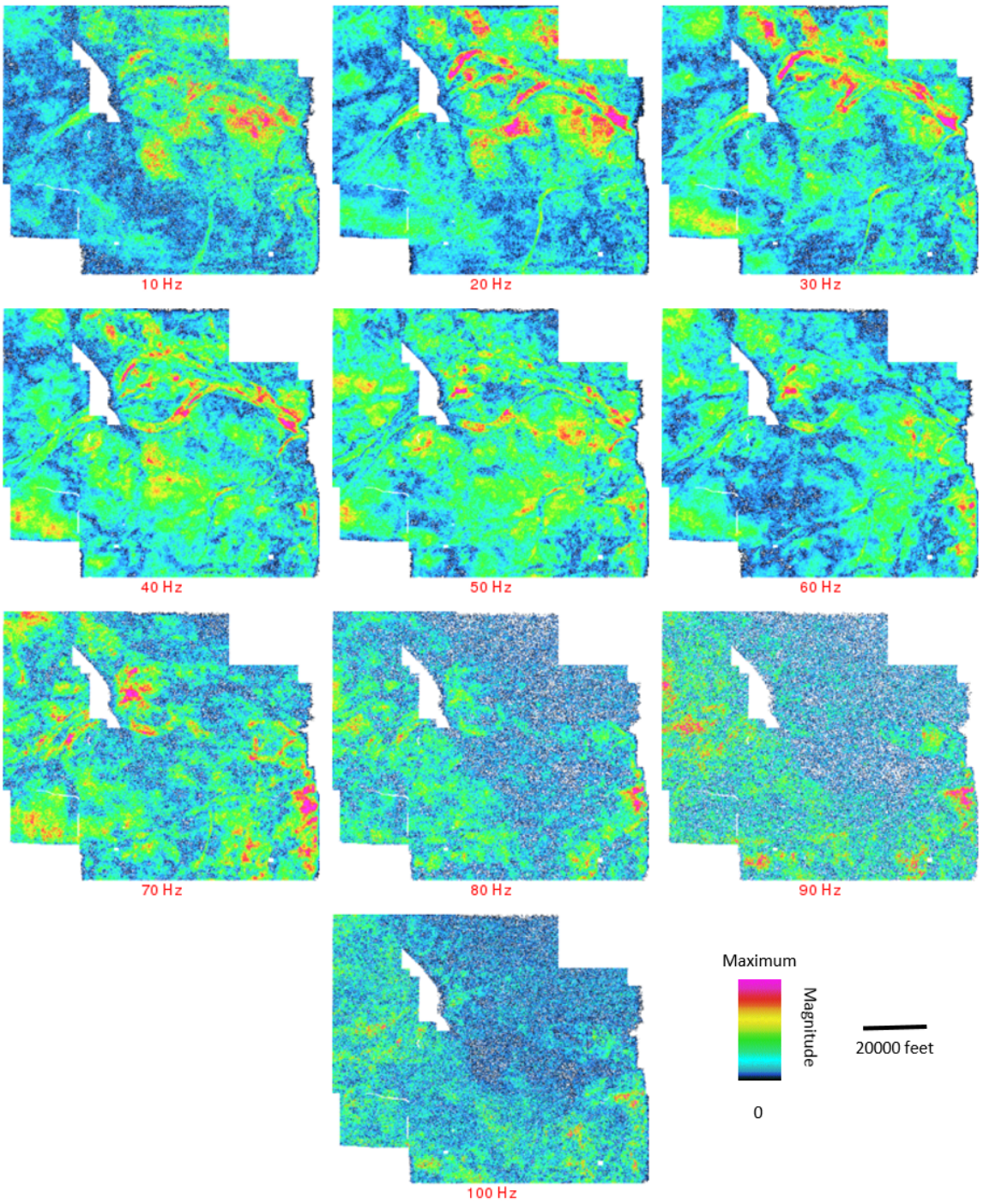


Figure 2.4: Phantom horizon slice of the spectral magnitude volumes taken 90 ms below the Pink Lime horizon.

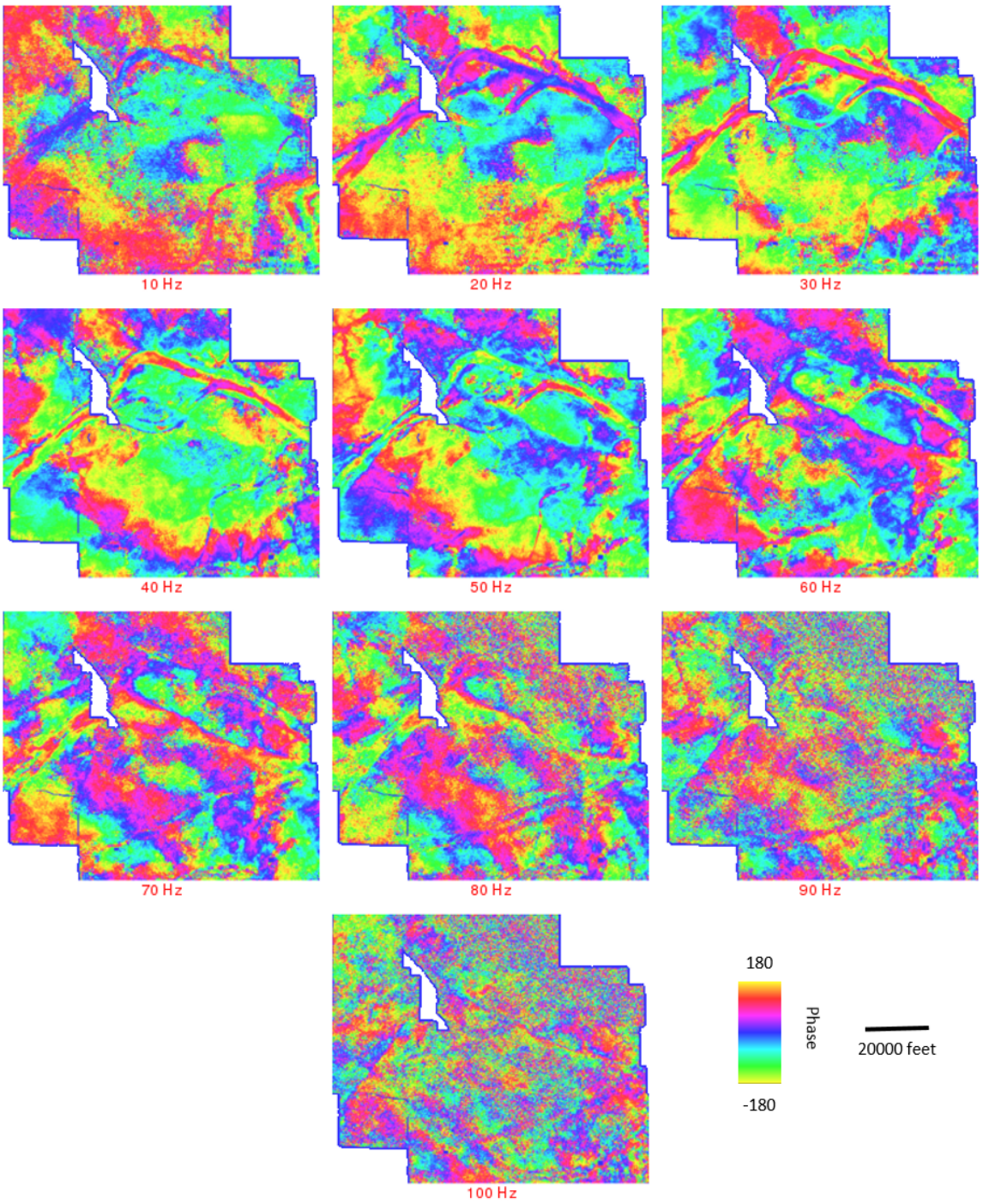


Figure 2.5: Phantom horizon slice of the spectral phase volumes taken 90 ms below the Pink Lime horizon.

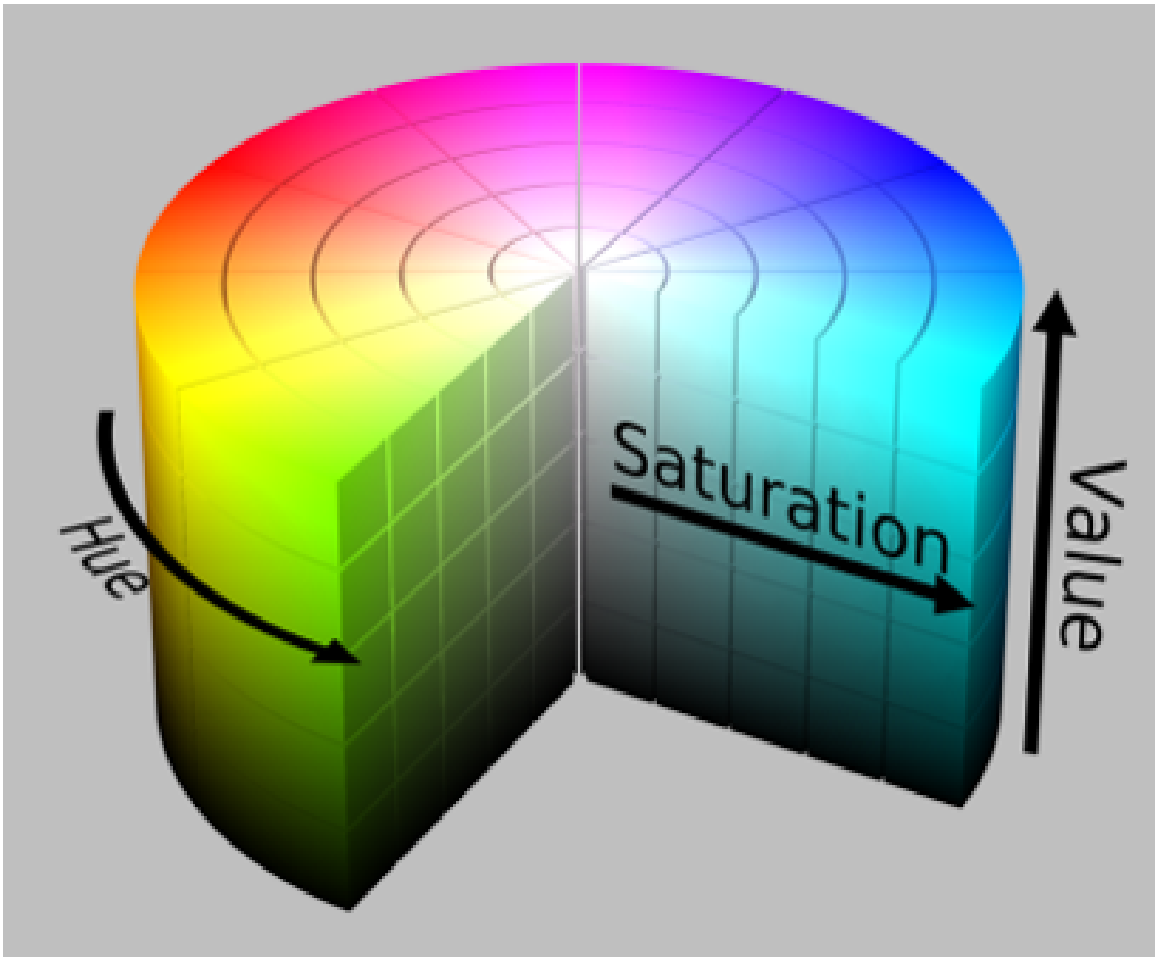


Figure 2.6: HSV is a cylindrical-coordinate color representation model. Hue represents a pure color about the cylinder. Saturation represents a purity of color ranging from white to a pure color. Value represents an illumination from black to a bright color. (Wikimedia Commons)

shown that images with more pastel palettes are often easier to interpret. Figure 2.8 shows the phase and magnitude HSV blended images with a constant saturation of 0.5. These images appear slightly more interpretable than those in Figure 2.7. These images appear very rich in the information they display, and I believe this to be a good visualization method. It is thus a qualitative choice that is up to the prejudices of the interpreter. However, I will choose to work with partially saturated HSV images for the remainder of this study.

2.4 Interpreting phase and magnitude

Having established my preferred method of visualizing phase and magnitude, I next choose to interpret with my images to assess the power and validity of this approach. Peyton et al. (1998) interpreted five stages of flooding and incision as shown in Figure 2.9.

Figures 2.10-2.16 show 10 Hz through 70 Hz respectively of spectral phase and magnitude using a HSV color map for the phantom horizon taken 90 ms below the Pink Lime.

As we can see, there are a large number of methods for visualizing spectral decomposition information besides the commonly accepted approach of just considering magnitude data. Furthermore, each method offers a large number of images to consider, typically equal to the number of frequencies computed. The number of possible images grows even further if we consider the use of RGB color blending to co-visualize different frequency components (see Figure 2.17). For instance, if we use this approach to co-visualize various frequency components of magnitude, we must consider $n!/(n-3)!$ different images where n is the number of frequencies. This number can be quite large indeed! Given just 10 frequencies, this results in 720 possible images.

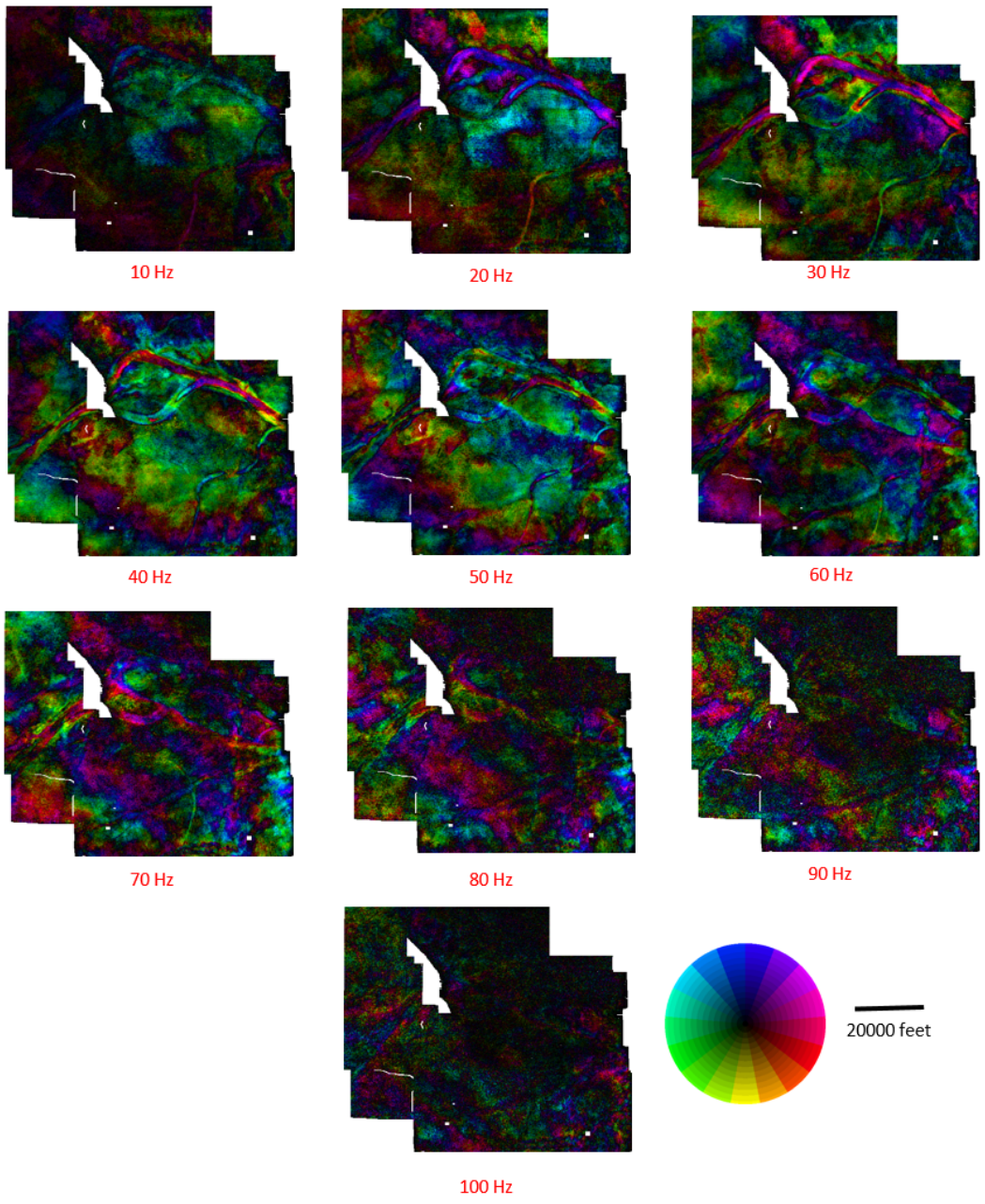


Figure 2.7: Phantom horizon slice of the spectral magnitude and phase volumes taken 90 milliseconds below the Pink Lime horizon displayed using a HSV color map. Phase is displayed as hue while amplitude is displayed using the value channel.

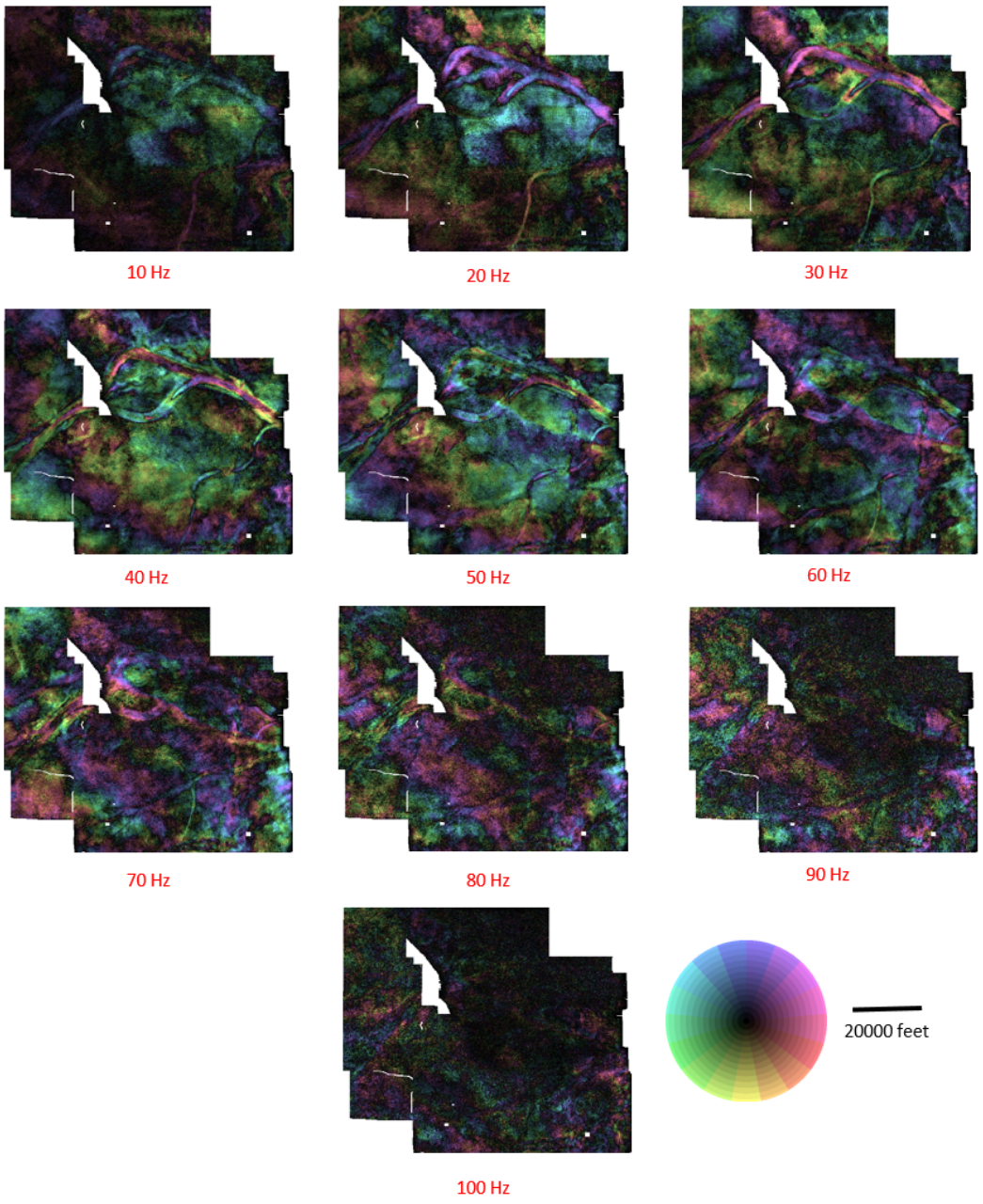


Figure 2.8: Phantom horizon slice of the spectral magnitude and phase volumes taken 90 milliseconds below the Pink Lime horizon displayed using a HSV color map. Phase is displayed as hue while amplitude is displayed using the value channel. Saturation is set to a constant value of 0.5 to provide a more pastel image.

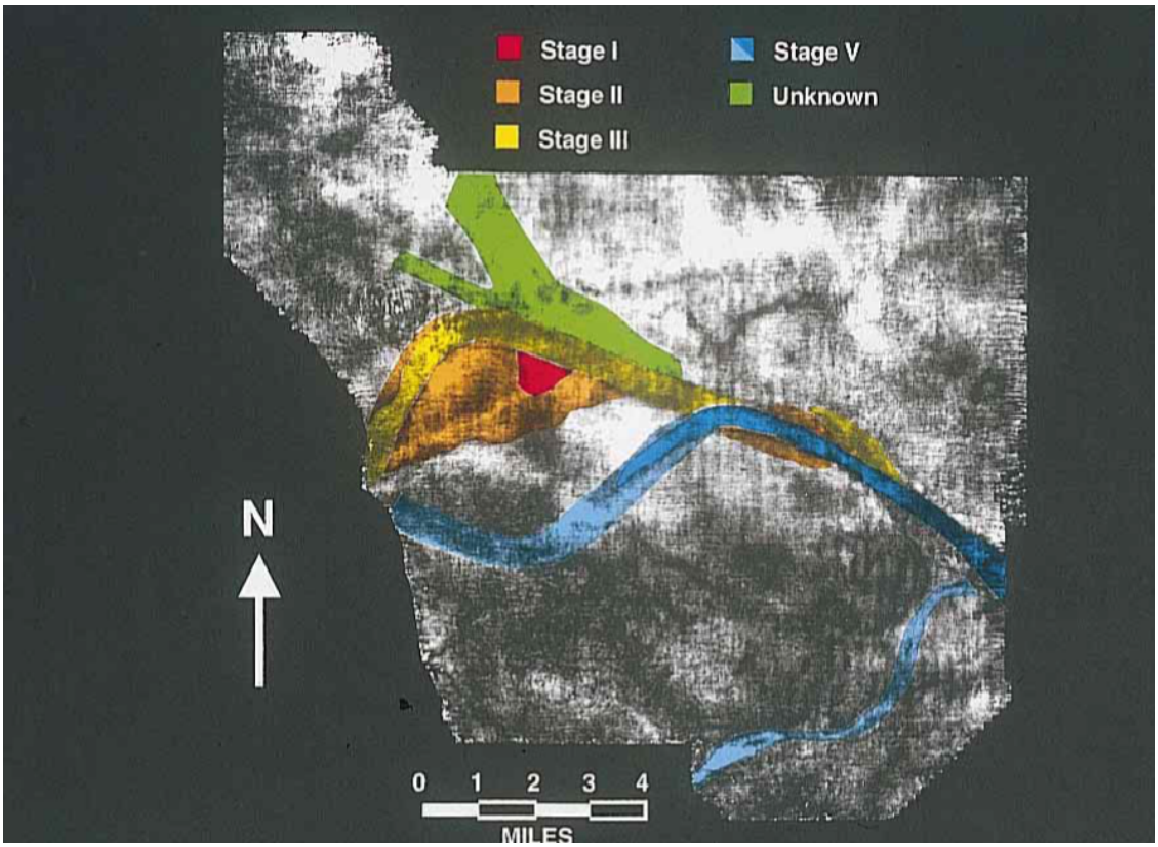


Figure 2.9: Peyton interpreted five stages of flooding and incision as shown in this Figure. These interpretations are overlain upon a 36 Hz spectral magnitude image. After Peyton et al. (1998)

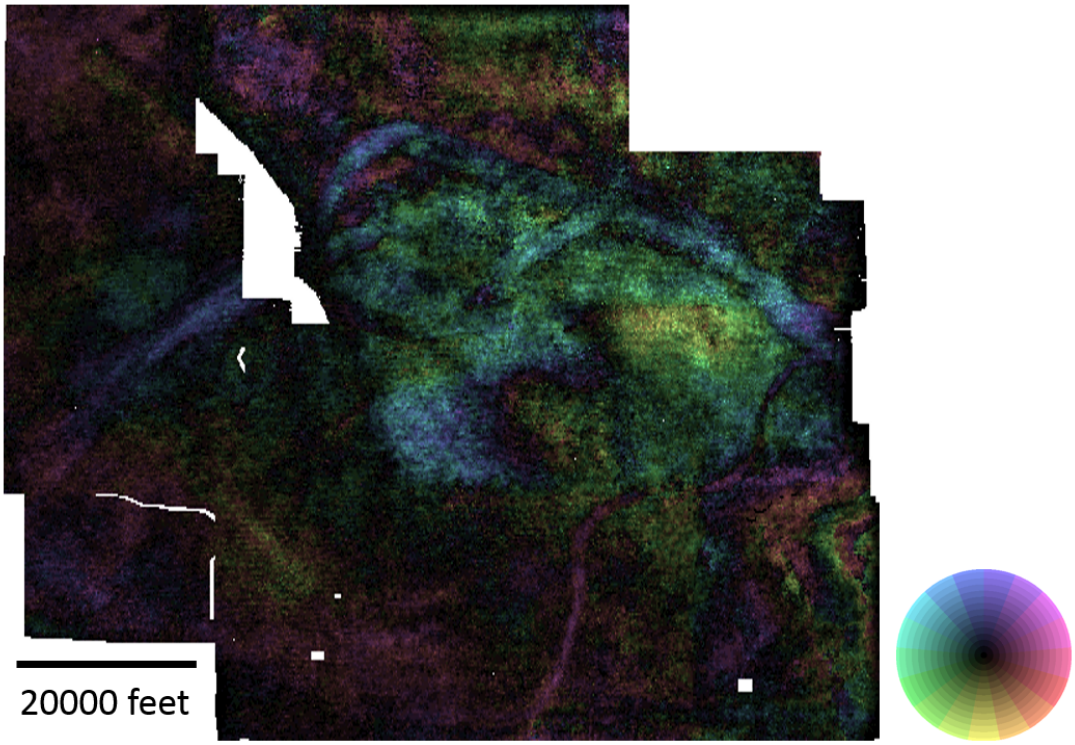


Figure 2.10: 10 Hz spectral phase and magnitude using a HSV color map for the phantom horizon taken 90 ms below the Pink Lime. Only broad features are visible, and considerable noise is evident in this image.

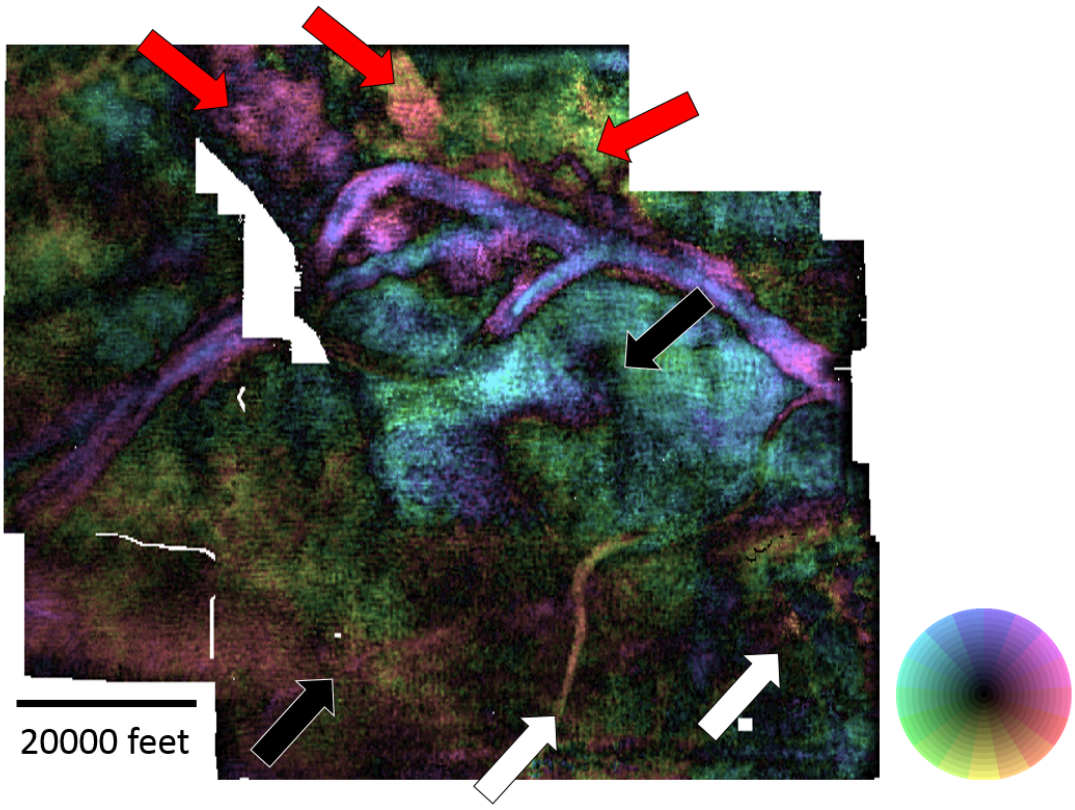


Figure 2.11: 20 Hz spectral phase and magnitude using a HSV color map for the phantom horizon taken 90 ms below the Pink Lime. Significant details are visible of the unknown stage (Peyton et al., 1998), denoted by the red arrows. The white arrows highlight a number of meandering channels, and the black arrows show what appears to be oxbows and abandonment channels.

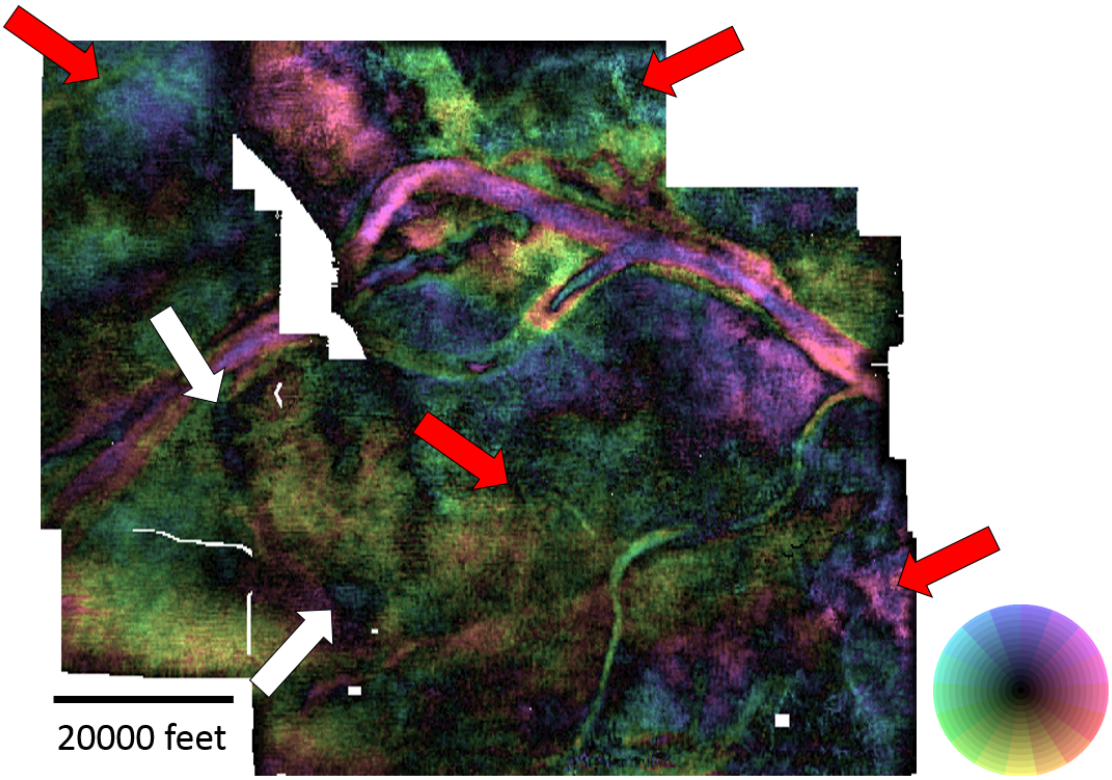


Figure 2.12: 30 Hz spectral phase and magnitude using a HSV color map for the phantom horizon taken 90 ms below the Pink Lime. Increasing levels of detail are visible compared to the previous figures. The red arrows show areas of increasing detail in fine channel structure. The white arrows show what appears to be regional Red Fork channel bars or reefs.

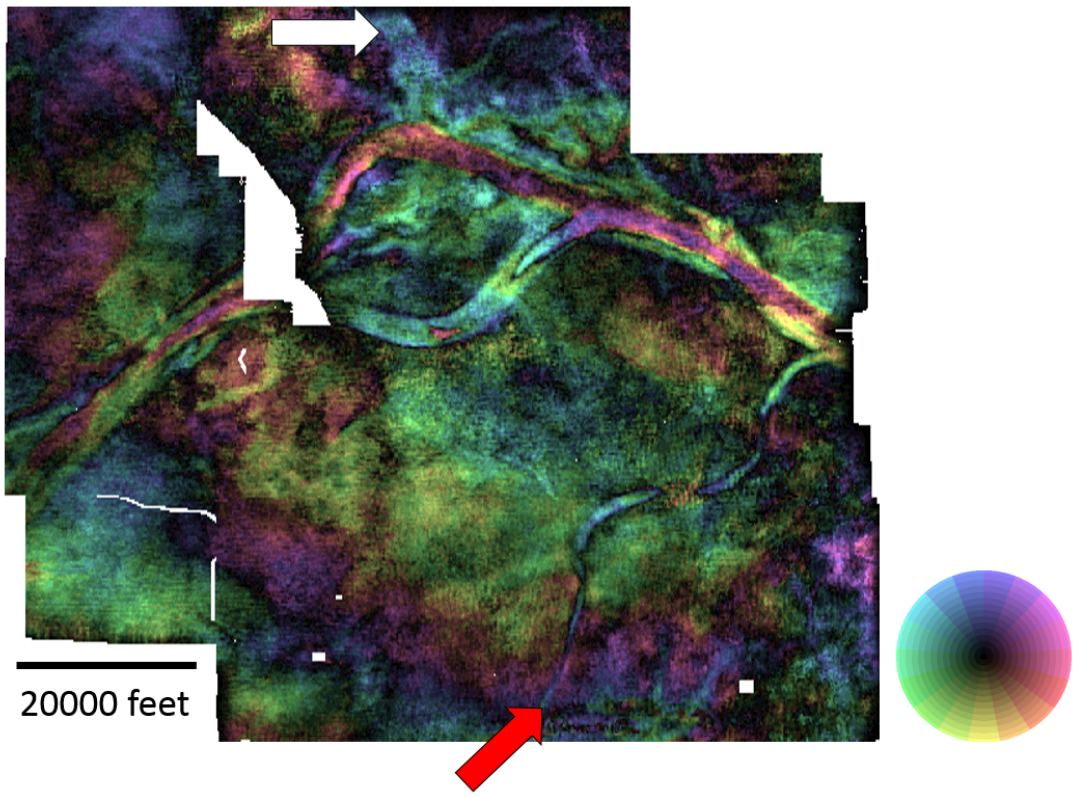


Figure 2.13: 40 Hz spectral phase and magnitude using a HSV color map for the phantom horizon taken 90 ms below the Pink Lime. Increasing frequency continues to provide increasing detail in the architectural elements. Interestingly, improved vertical resolution seems to lead to improved horizontal resolution. The unknown stage (white arrow) is seen in very high detail showing complexity not show by previous work. Stage 5, as shown by the red arrow is better defined in this image as well.

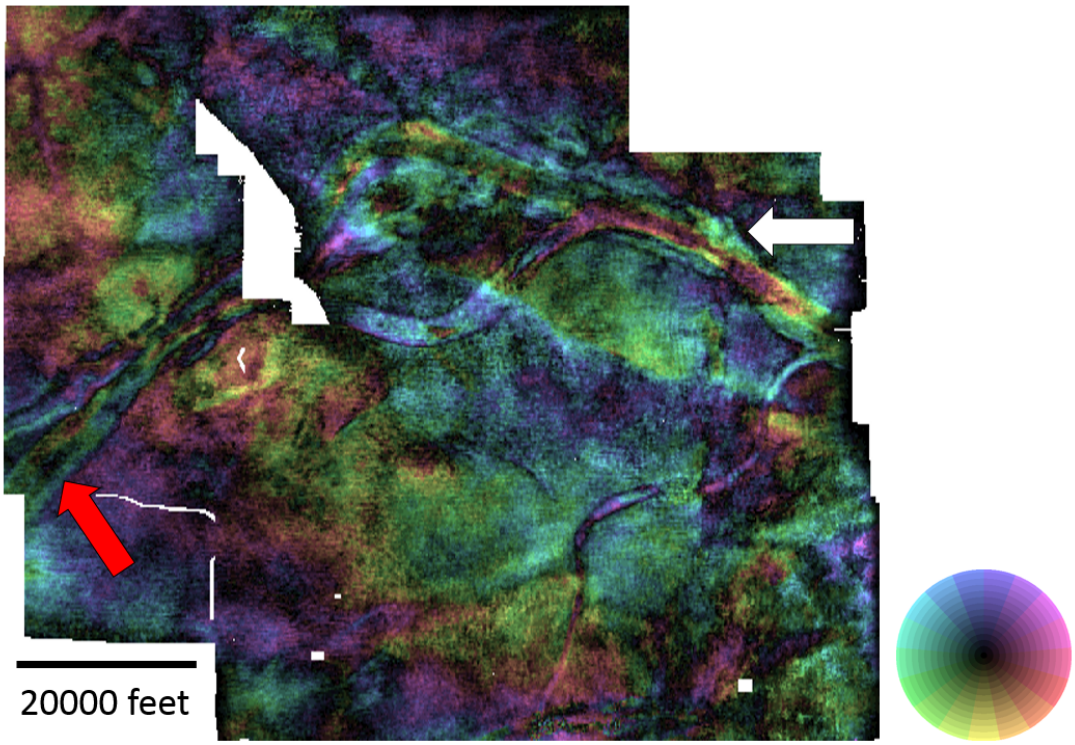


Figure 2.14: 50 Hz spectral phase and magnitude using a HSV color map for the phantom horizon taken 90 ms below the Pink Lime. Stage 2 and 3 are well differentiated to the southwest (red arrow) while the unknown stage is better differentiated to the northeast (white arrow).

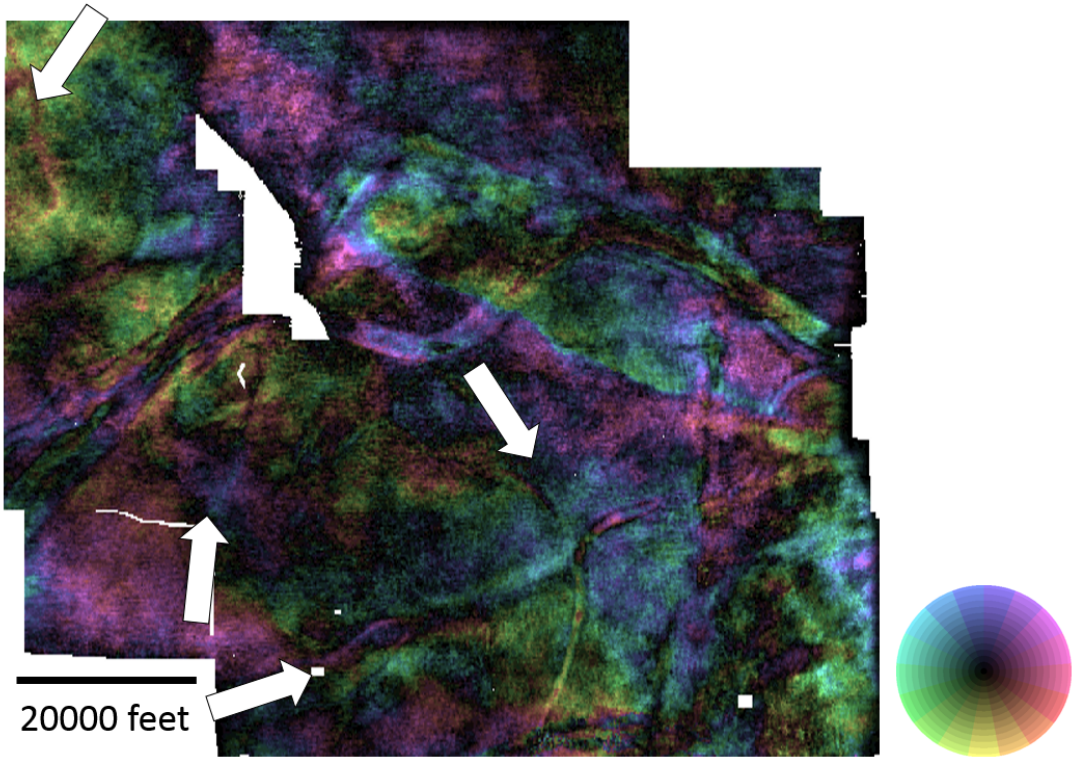


Figure 2.15: 60 Hz spectral phase and magnitude using a HSV color map for the phantom horizon taken 90 ms below the Pink Lime. Many channel like features are well defined in this view as shown by the white arrows.

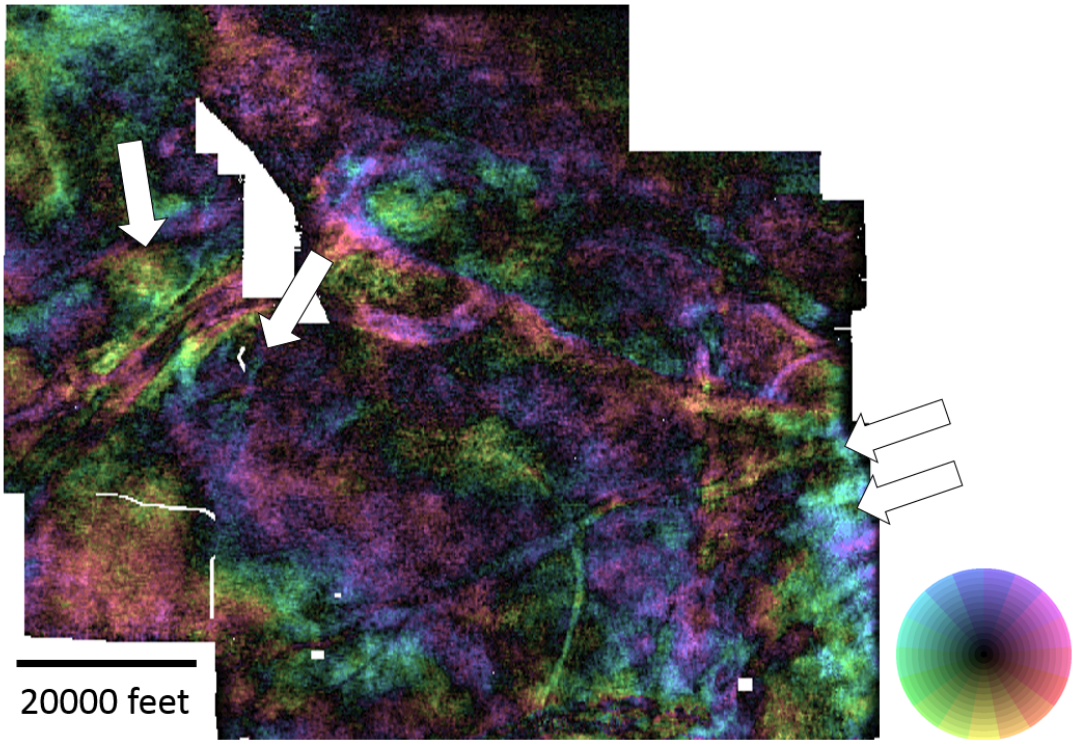


Figure 2.16: 70 Hz spectral phase and magnitude using a HSV color map for the phantom horizon taken 90 ms below the Pink Lime. Strong noise is becoming apparent. However, many small channel features are now visible as shown by the white arrows.

There are a number of approaches to dealing with this large set of possibly interesting images. One method uses an interactive approach called the image grand tour or IGT (Wallet and Marfurt, 2008; Wallet, 2013). In the next section, I use Principal Component Analysis (PCA) to further analyze representation schemes and visualization methods.

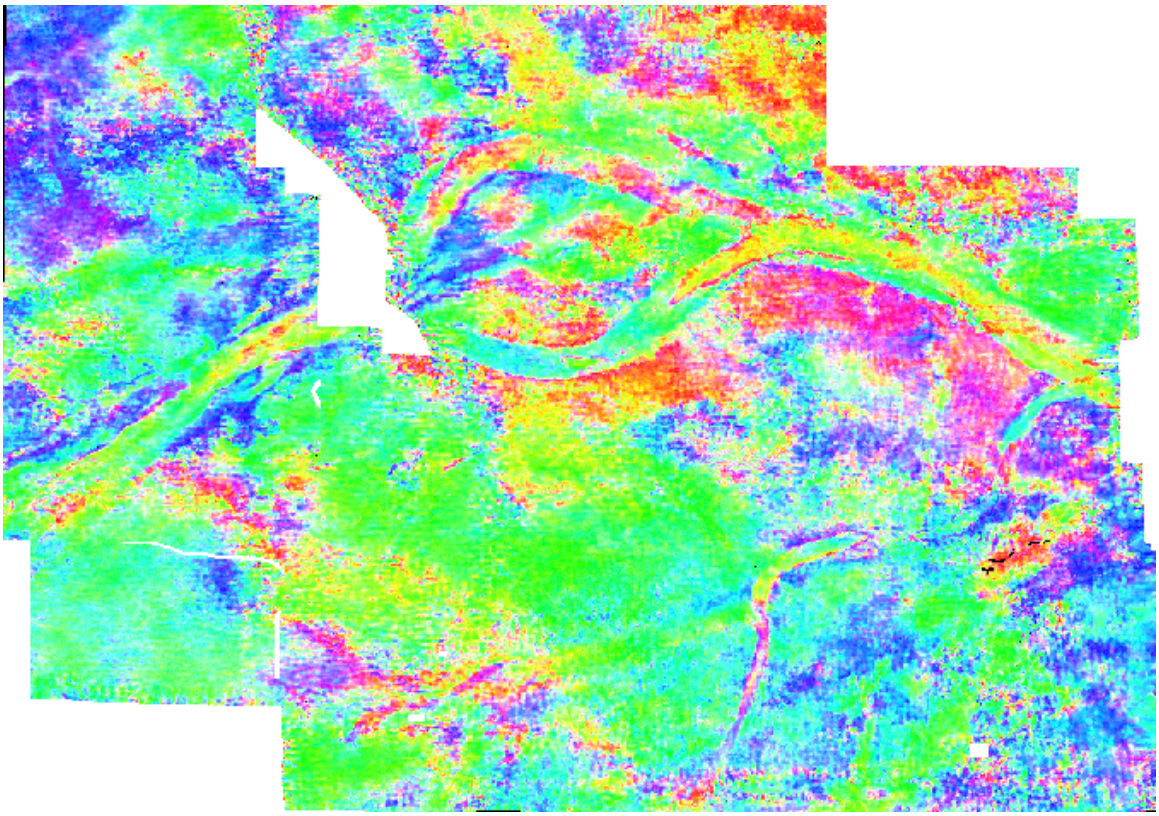


Figure 2.17: Phantom horizon slice of the spectral magnitude volumes with 20 Hertz displayed as red, 40 Hertz displayed as green, and 60 Hertz displayed as blue.

2.5 Principal Component Analysis (PCA)

PCA (Jackson, 2003) is an orthogonal transform designed to convert a d-dimensional data set of possibly correlated variables into a d-dimenional data set of linearly uncorrelated variable known as principal components. While these principal components are uncorrelated, the assumptions of PCA include that the original data are drawn

independent, identically distributed (*iid*) from a multivariate normal distribution. Theory suggests that spectral magnitude is drawn from a lognormal mixture distribution, violating part of the assumption. While reasons related to the *central limit theory* make normality reasonable, the *iid* assumption does not generally hold for spectral decomposition of seismic amplitude data since the data represent a variety of different processes related to the underlying geology (Wallet, 2013).

With PCA, the principal components are ordered such that the first principal component represents the highest possible amount of variance. Each successive principal component represents the highest possible variance of the remaining orthogonal dimensions. If we thus define variance as information, the principal components are thus ordered according to their information content. Commonly, a low number of principal components are retained while most are discarded as noise, providing a method of linear dimensionality reduction.

Guo et al. (2006) previously demonstrated that PCA was an effective way to reduce the number of spectral magnitude components to a number that could be visualized using a RGB color map. He was working with just the real, magnitude values. However, using the complex respresentation for spectral decomposition information, $\zeta_f = A_f e^{i\varphi_f}$, it is possible to perform PCA upon phase and magnitude information jointly. The resulting output is itself complex.

Figure 2.18 shows the phase and magnitude components for all ten principal components for our phantom horizon of interest. Note that most of the information appears in the first 2 principal components. This is in line with what is suggested by the eigenvalues (Figure 2.19).

Figure 2.20 shows the first principal component with an interpretation. Most of the architectural elements shown in Figures 2.10-2.16 appear in this image. Figure

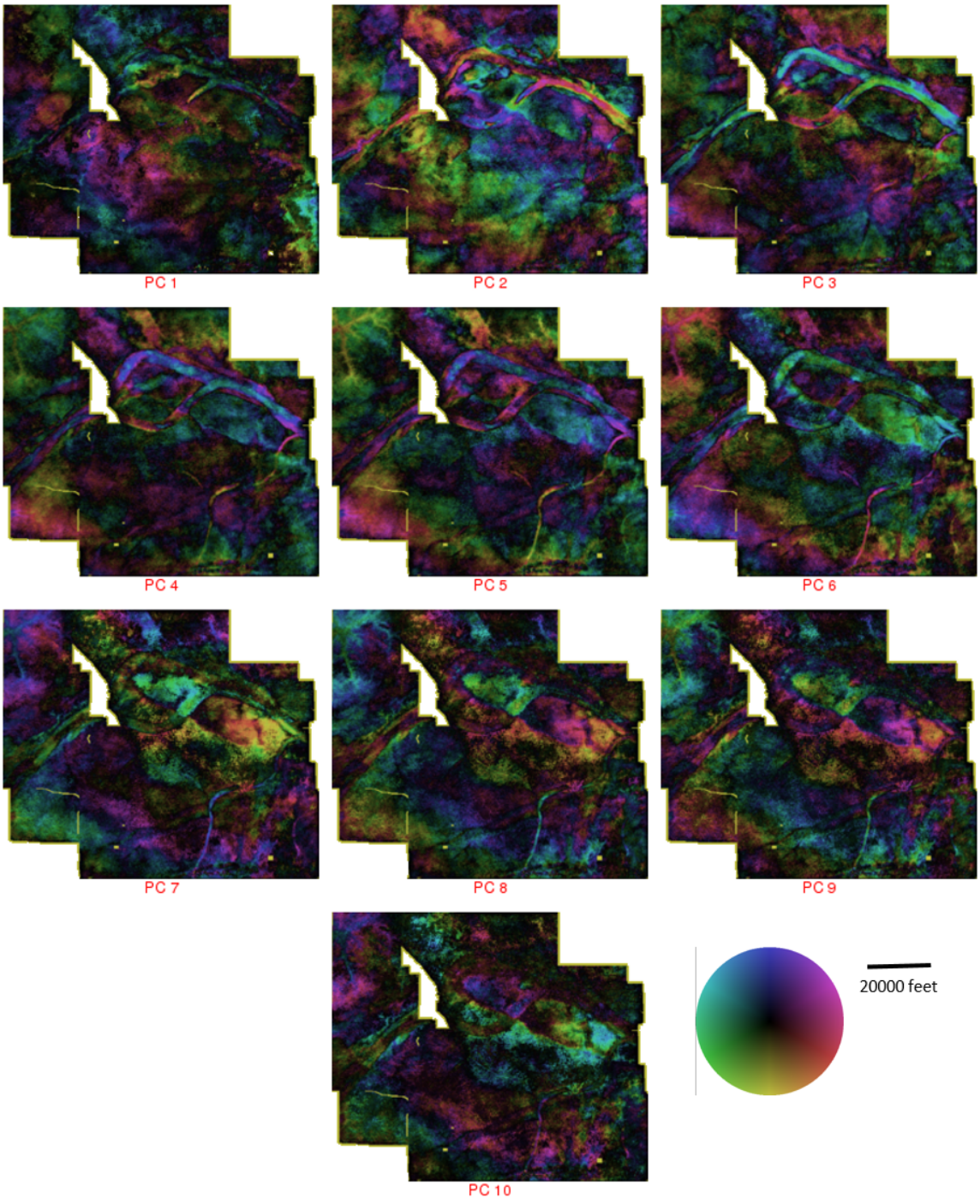


Figure 2.18: Horizon slices of the principal components of spectral phase and magnitude components.

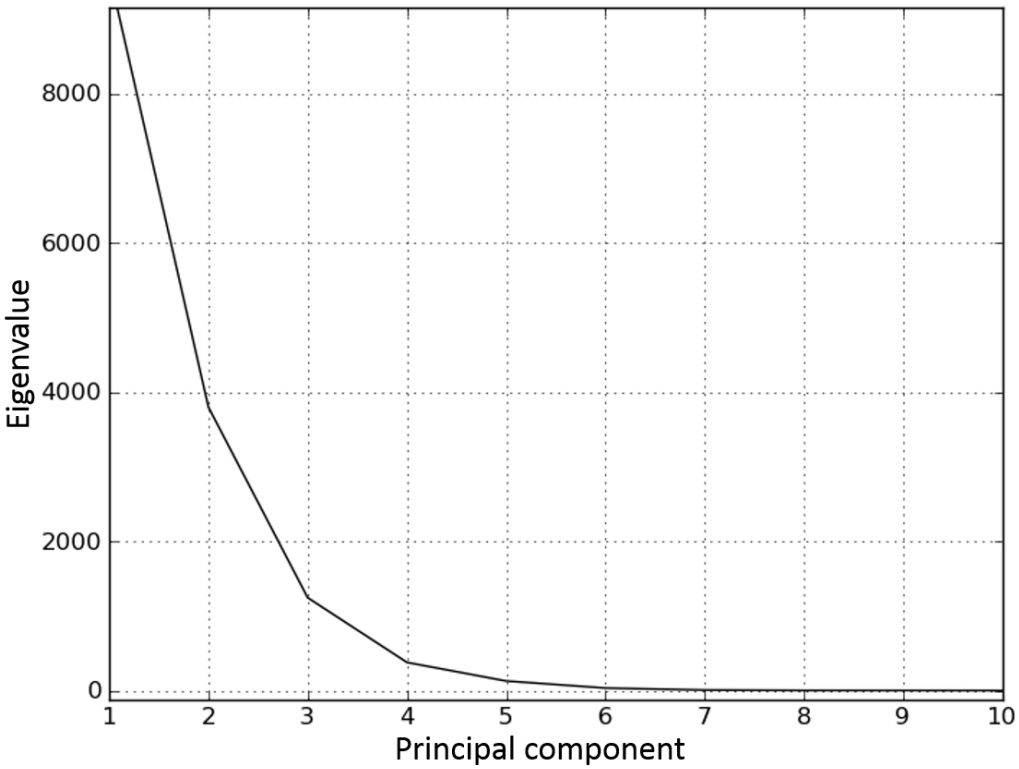


Figure 2.19: Eigenvalue plot for the PCA of the complex spectral components. This suggests no information past the fourth principal component.

2.21 shows the second principal component with an interpretation. The vast majority of the architectural elements are present in these first two principal components. However, as seen in Figure 2.22, even the tenth principal component is found to have information that is not present in the first two.

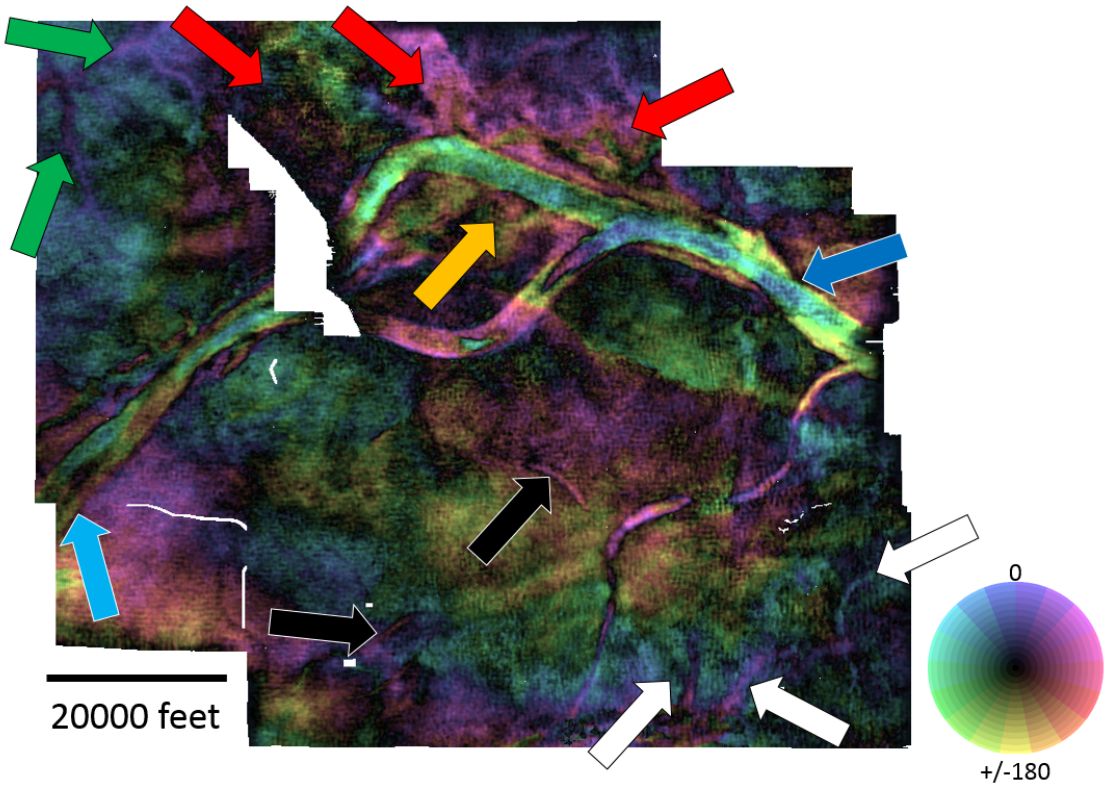


Figure 2.20: HSV plot of the phase and magnitude of the first principal component. Most of the architectural elements present in the spectral components are visible. The red arrows show the unknown stage. The blue arrow shows stage five. The white arrows a number of small meandering channels. The black arrows show abandonment channels. The cyan arrow shows separation between stage two and three. The green arrows show small, channel like features. The gold arrow shows stage one.

2.6 Statistical analysis of PCA

An examination of Figure 2.8 suggests considerable correlation between spectral components. For example, Table 2.1 shows the correlation matrix between the spectral

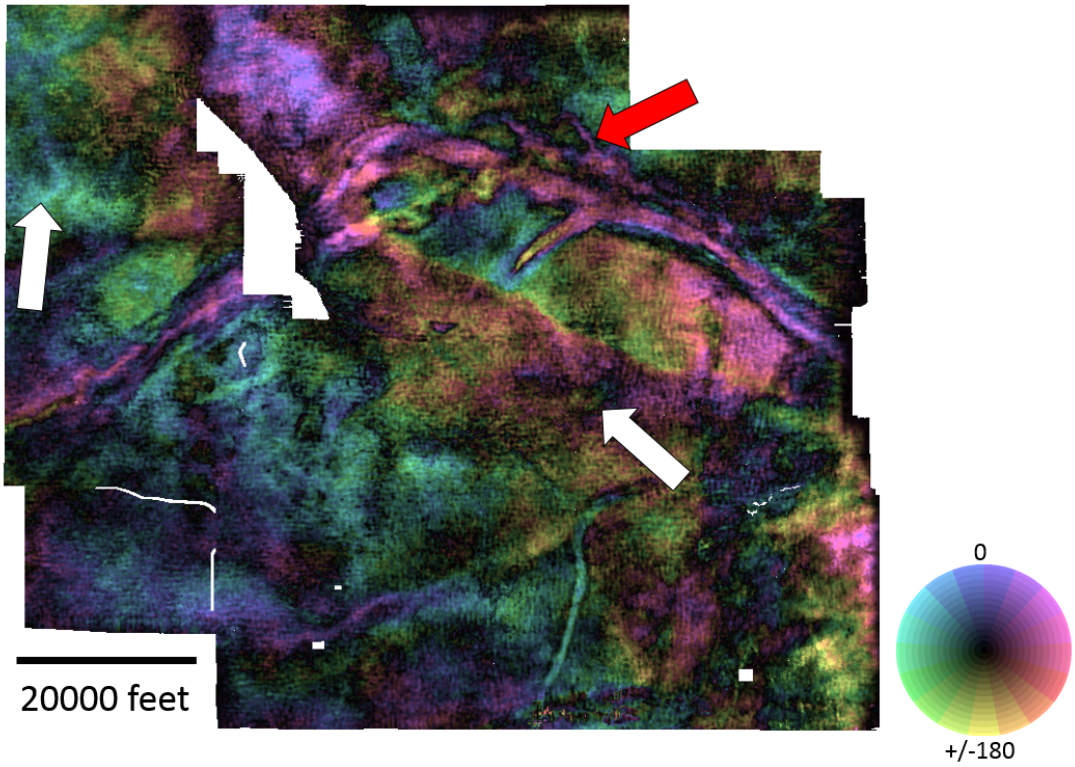


Figure 2.21: HSV plot of the phase and magnitude of the second principal component. The white arrow shows improved views of channels and channel like features over the first principal component. The red arrow highlights detail of the unknown stage that was not visible in the previous image.

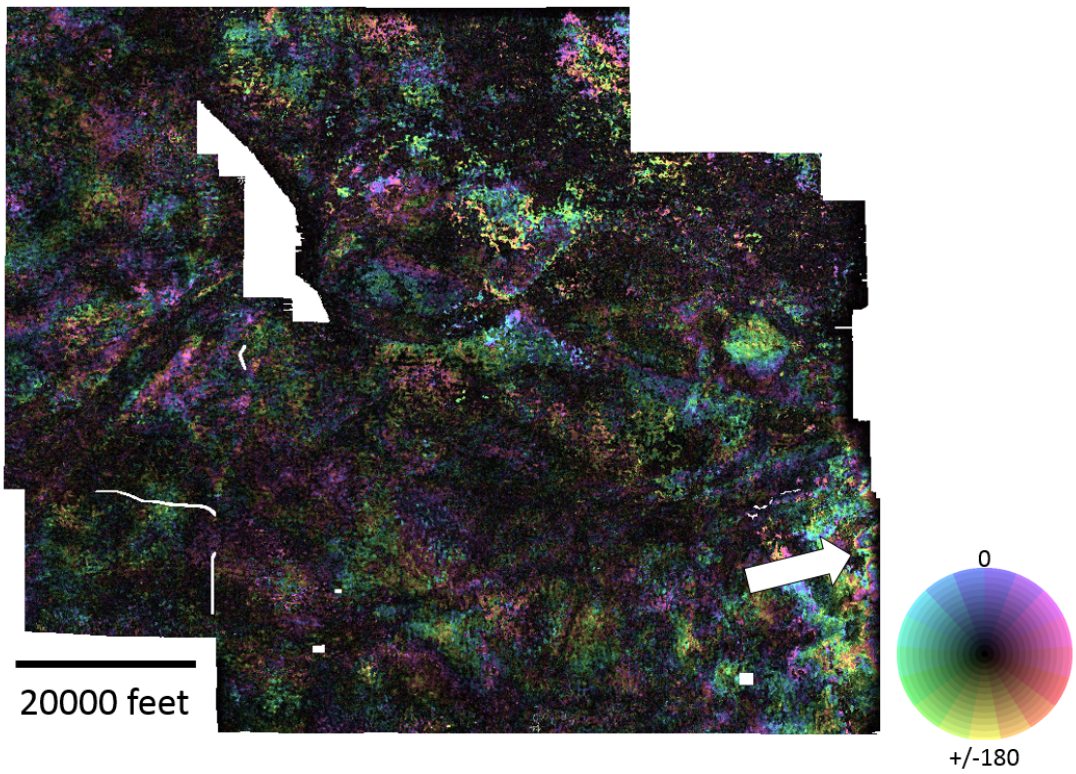


Figure 2.22: Tenth principal component is very noisy as we would expect. However, considerable spatial patterns are still visible including interpretable features. The white arrow shows a channel like feature that was not visible in the first two principal components.

components. This again bears out the strong correlation between components.

Frequency	10 Hz	20 Hz	30 Hz	40 Hz	50 Hz	60 Hz	70 Hz	80 Hz	90 Hz	100 Hz
10 Hz	1.0000	0.9951	0.9693	0.9087	0.8060	0.6638	0.4957	0.3224	0.1628	0.0285
20 Hz	0.9951	1.0000	0.9888	0.9445	0.8569	0.7260	0.5638	0.3910	0.2276	0.0869
30 Hz	0.9693	0.9888	1.0000	0.9826	0.9218	0.8133	0.6658	0.4990	0.3342	0.1866
40 Hz	0.9087	0.9445	0.9826	1.0000	0.9772	0.9040	0.7839	0.6336	0.4748	0.3246
50 Hz	0.8060	0.8569	0.9218	0.9772	1.0000	0.9735	0.8944	0.7742	0.6329	0.4889
60 Hz	0.6638	0.7260	0.8133	0.9040	0.9735	1.0000	0.9724	0.8952	0.7845	0.6581
70 Hz	0.4957	0.5638	0.6658	0.7839	0.8944	0.9724	1.0000	0.9740	0.9045	0.8071
80 Hz	0.3224	0.3910	0.4990	0.6336	0.7742	0.8952	0.9740	1.0000	0.9771	0.9166
90 Hz	0.1628	0.2276	0.3342	0.4748	0.6329	0.7845	0.9045	0.9771	1.0000	0.9800
100 Hz	0.0285	0.0869	0.1866	0.3246	0.4889	0.6581	0.8071	0.9166	0.9800	1.0000

Table 2.1: Correlation between spectral components based upon Pearson's linear coefficient.

This correlation is thus the motivation for doing PCA, and doing such will produce results that, on a point by point basis, are statistically independent. However, comparing the principal components shown in Figures 2.20-2.22 gives the impression of dependence. Specifically, the same structural elements are visible in many of the different images.

These images suggest a different definition of dependency based upon spatial information. In order to test this concept of spatial dependence, I applied a 3x3 Sobel filter to the first two principal components of the spectral magnitude. I then calculated the correlation between the two data sets, and found the correlation to be 0.312 corresponding to a moderate amount of agreement. Thus, even though the spectra have been rotated to be statistically independent, the resulting images still present much of the same spatial information.

2.7 Conclusions

In this paper, I have explored several methods for visualizing spectral components. Novel among these is a method for using an HSV colormap to simultaneously visualize both spectral magnitude and phase. This method provides rich images that appear

to capture considerable geologic detail. I used hue to represent phase since it has a circular presentation, and I used value to represent magnitude. I showed that images were more visually effective when using partially saturation rather than full saturation.

Additionally, I demonstrated the use of complex PCA upon both phase and magnitude information simultaneously by using a complex representation. This produced a single image that captured much of the interpretational value that was present in the higher dimensional data set. Finally, I used a spatial filtering and correlation workflow to demonstrate that while the principle components were statistically independent on a pixel by pixel basis, they were not informationally independent. This is because PCA does not consider the spatial information that is inherent in image or volume data.

The work that I have presented here leaves a number of interesting challenges for further study. One interesting problem is how to best display peak frequency plus the associated phase and magnitude components. The issue is the nature of the saturation and value components of the HSV colormap. Both tend to discount the represented observation at low values while providing emphasis at higher values. This is good when you have an end of the spectrum of an attribute which you wish to discount such as low magnitudes, low dips (Wallet et al., 2011), or low confidence values. However, neither phase nor frequency have this characteristic, and hence this attribute set is poorly suited for this form of visualization.

Additionally, I have raised concerns about the use of PCA for spatial data. The obvious challenge becomes to incorporate spatial information in dimensionality reduction of attributes. One possible solution is the use of task based metrics and an optimization method (Wallet et al., 1997). Another possible approach is to use interactive visualization to incorporate interpreter input (Wallet and Marfurt, 2008;

Wallet, 2013).

CHAPTER 3

Using the Image Grand Tour to Visualize Fluvial Deltiac Architectural Elements in South Texas, USA

This article was previously published in *Interpretation* (Wallet, 2013). It appears as published with minor formatting changes to accommodate the venue.

Abstract

Spectral decomposition can produce dozens of attributes for a single data set, far exceeding the ability for direct visualization. A number of solutions have been proposed. The state of the art approach is via the use of Principal Component Analysis (PCA). However, PCA has a number of significant inherent weaknesses such as a lack of inclusion of spatial information and a tendency to inflate noise.

Previous work has shown the ability of the Image Grand Tour (IGT) to construct lower dimensional views of spectral information resulting in multiple images showing distinct architectural components. In this chapter, I discuss a novel workflow for constructing color images to display multiple structures simultaneously. These images are constructed in a way that makes them complementary, leading to rich color images that are useful for interpretation. I demonstrate the value of this workflow though application to a land survey over Tertiary channels from south Texas.

3.1 Introduction

Seismic attributes have been the subject of considerable research where the most commonly used attributes are developed to highlight specific patterns in the seismic data that can be correlated to geology. In other cases, empirical or more rigorous statistical evidence suggests a relationship between an attribute and a physical process or rock property when relating the interpretation to well data. However, the exact mechanism of the relationship may not be readily apparent.

Spectral decomposition is an interesting variant on this taxonomy. In the case of spectral decomposition, the calculated attribute can be linked to a number of physical phenomena including channel thickness and fill velocity. However, since geobody thickness and contrast vary between and even within surveys, it is impossible to identify a single spectral decomposition based attribute that has universal interpretation utility (Wallet, 2008). The result of this lack of universality is that rather than a one- or three-dimensional attribute, an interpreter using spectral decomposition is left to interpret using an attribute that is commonly between 10 and 100 dimensional. While techniques exist for visualizing high dimensional data (see Appendix B), they are generally not applicable of the visualization of image or volumentric data such as seismic surveys (Wallet and Marfurt, 2008).

Given the limitations of visualizing high dimensional spatial data (see Appendix A), it is natural to suggest some form of dimensionality reduction in interpreting using spectral components. Using commercial software Bahorich et al. (2002) showed the value of displaying three different spectral components using an RGB color model. Marfurt and Kirlin (2001) respresented the spectrum by its peak magnitude, frequency, and phase at the peak magnitude. Zhang et al. (2009) estimated bandwidth and slope of the flattened spectra using histogram analysis. Guo et al. (2006) first

proposed the use of principal component analysis (PCA) (Jackson, 2003) for this purpose. They then displayed the first three principal components (pc) using an RGB color scheme with each pc mapped into the color components of an RGB image for display.

Liu and Marfurt (2007b) proposed a filtered approach to reducing the dimensionality of spectral decomposition information for visualization. They create new attributes by creating stacks of band-limited spectral components. These filters thus define sets of projection weights that are used to sum spectral components. The net result is a lower dimensional set of spectral attributes. They can then be interactively used as the color components of a RGB color display.

This filtered approach has been shown to be effective at visualizing channel systems. However, it assumes relatively simple relations between architectural elements and spectral components. All weighting parameters are required to be positive, and the relations between spectral components are primarily considered to be locally isolated in frequency space.

I begin with a detailed description of my methodology. In this paper, I provide details behind my previously published work on the image grand tour (Wallet and Marfurt, 2008; Wallet, 2008).I start with a discussion of principal component analysis with an emphasis upon the motivation for my approach. I then discuss the grand tour, an interactive approach to examining multi-dimensional data used by statisticians and data miners. I discuss the extension to spatial data, and I show how my color extensions can better detail complex systems that occur in hydrocarbon exploration.

After having defined the algorithm, I apply it to the interpretation of a fluvial deltaic system from the Middle Frio Formation of south Texas, USA. I conclude by comparing my results to those of the more conventional approach of principal

component analysis.

3.2 Methodology

3.2.1 Principal Component Analysis (PCA)

PCA, also known as a the Karhunen-Loève transform, is an orthogonal transform that maps an attribute space into a new attribute space of the same dimension called the principal components. PCA is designed in such a way that the first principal component (pc) has the maximum statistical variance with each successive pc having a lower variance until the last which has the lowest variance. These pc's correspond to the projections of the data using the eigenvectors of an eigenvalue decomposition of the estimated covariance matrix. The interpreter then decides how many pc's to keep based upon the values of these variance (represented by the eigenvalues from the transform) and perceived spatial information. Since seismic attributes are sensitive to the underlying geology, they are generally coupled such that a small number of principal components contain the vast majority of the variance present in the data. The end result of this transform and selection process is a new, lower-dimensional attribute space.

It is a common misconception that because dimensions of the transformed data are statistically independent, they are informationally independent. In fact, this is only the case if the original data were independently identically distributed (iid) according to a multivariate normal distribution. Since seismic data represent multiple geological and geophysical processes of a spatial nature, we generally do not expect this condition to hold. I will examine the failings with regards to spatial data later.

We should also note that the major and perhaps most troubling assumption of

PCA is that components having greater variance corresponds to those having greater information. While this assumption may have a theoretical basis, it does not match our general understanding of information. When interpreting, "information" is any data or knowledge that contributes to the task of assigning meaning to seismic data that results in improvement in the accomplishing some task of interest. Typical tasks may be such things as determining the location of a channel or predicting fluid content in a reservoir rock.

For example, acquisition footprint is generally considered as noise as it tends to impede the interpretation of faults and other geological lineaments. However, footprint is not random, and it represents knowledge about the acquisition process. In cases where the task is to remove acquisition footprint, it is considered information, and it can be used to characterize and quantify itself (Elis, 2011).

Understanding what is noise and what is information is thus the responsibility of the interpreter. In many cases, the interpreter chooses attributes and workflows that emphasize information and de-emphasize noise. In other cases, the interpreter will analyze in the presence of noise and use experience to disregard parts of the data.

In many tasks, including seismic exploration, noise often comprises the majority of the data. The uninteresting background is often dominant while the target (such as a productive reservoir) is something that must be located. In such a case, preserving the high variance principal components while supressing components that contribute relatively little to the representation of the overall variance of the data will enhance the strongest, most consitent geological features and suppress the low variance anomalies of interest. In this case, PCA could be optimally wrong!

In some cases, single or multiple attribute values by themselves are sufficient to identify features of interest. This is particularly prevalent in hyperspectral imagery



Figure 3.1: Four images representing four different spatial processes. The grayscale levels for all four images have similar ranges and thus would not be sufficient to separate these images if they were mixed.

where poor spatial resolution means that targets in an image are single or even sub-pixel in size (Manolakis et al., 2001). In most applications, including seismic interpretation, spatial information is very important in identifying features of interest.

Figure 3.1 shows four spatial processes defined by grayscale images. In this case, we will consider the pictured animals to be the features of interest to be interpreted. Note that the animals constitute a large percentage of the image. However, grayscale alone is not sufficient to identify the animals with all four images having similar ranges of grayscale values. Key to this task is how the pixels having different grayscale values are organized in the lattice that comprises the image. Merely looking at a histogram of values is not sufficient to identify the seismic facies of the features of interest.

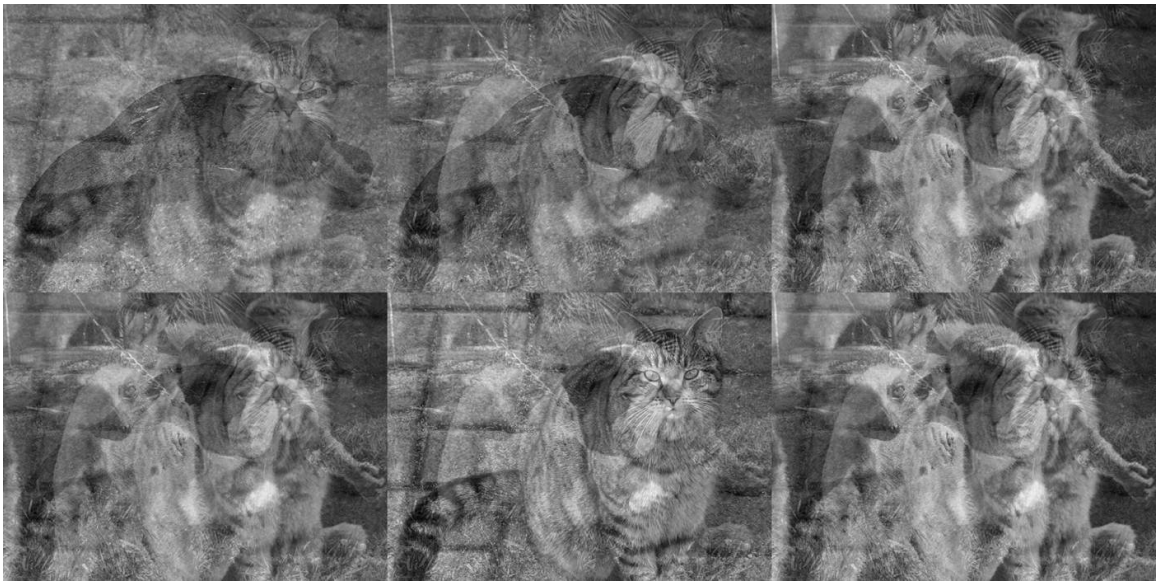


Figure 3.2: Six simulated attributes created by random linear combinations of the images in Figure 3.1.

To simulate the problem of extracting multiple spatial processes expressed as multiple attributes, I constructed a set of six attributes by creating random, linear combinations of the images shown in Figure 3.1. By randomly combining these four images, I created the six images shown in Figure 3.2. These images were created without the addition of any noise. Therefore, since they were created as linear combinations, a linear projection method should be able to perfectly recover the original images. The only source of additional noise would be some minor numerical roundoff related to the discrete nature of the computer system.

In order to evaluate PCA's ability to recover multiple spatial processes imbedded in multiple attributes, I applied PCA to the six images shown in Figure 3.2. The resulting output images are shown in Figure 3.3. These images show that PCA failed to recover the embedded images. These images do have some interpretive value. For instance, the third PC is useful for interpreting the bulldog. However, the images do not strongly extract the spatial processes. Based upon the images shown in Figure 3.3, it would be reasonable to truncate after the third PC. However, while the fourth

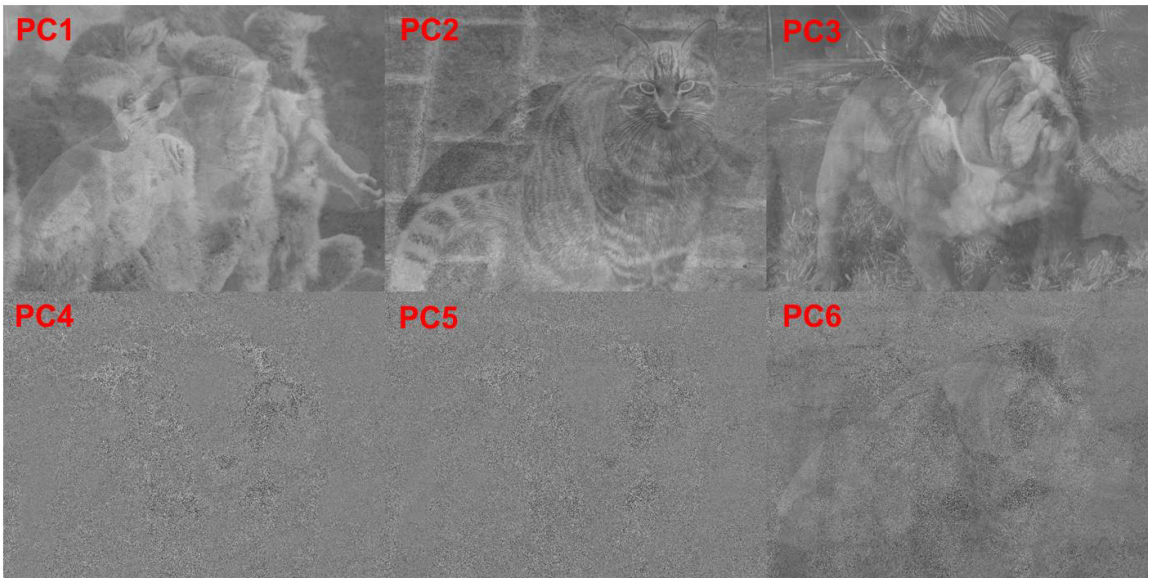


Figure 3.3: Six principal components from the attributes shown in Figure 3.2. None of these images is well suited to recover the original images (Figure 3.1). Note that the sixth pc has more information from an interpretation standpoint than either the fourth or fifth pc.

and fifth PC appear to be nothing but noise, the sixth PC clearly contains spatial information.

These images highlight a critical failing when dealing with spatial processes such as the geological structures that are imaged in seismic data. Since the processes are expressed in large part by the organization of the data in the spatial domain, dimensionality reduction methods that ignore this aspect do so at peril. Therefore, it would be better to use a method that retains this spatial information.

3.2.2 The Grand Tour

The grand tour (Asimov, 1985) is an interactive method of exploring high-dimensional data in a dynamic fashion. The premise of the grand tour is to look at many different projections of the data, allowing the analyst to then decide what is important and interesting structure. As first proposed by Asimov and further developed by Buja and



Figure 3.4: In three dimensions, a donut is a torus.

Asimov (1986), the grand tour presents crossplots of d-dimensional data projected linearly onto a 2D flat or plane. The set of all possible projections is a Grassmanian manifold (Wegman, 1992), and the original grand tour involved constructing a curve dense on the manifold of all possible projections. This works because a Grassmanian is topologically equivalent to a torus (Figure 3.4). It is thus possible to construct a curve wrapping around this torus and easily achieve a smooth path in the set of possible projections. The interpreter would then visualize a dynamic graph of the projected data utilizing this curve. By making the sequence of projections smooth, the grand tour creates the visual impression of watching a "data movie". The net result of the grand tour is analogous to looking at all sides of the data.

Wegman (1992) presents a method for constructing grand tours projected to arbitrary dimensions. By using this method, he projected $\mathbb{R}^d \longrightarrow \mathbb{R}^d$ with d being an arbitrary integer greater than two, in essence simply rotating the feature space in a

dense manner. He then visualized the data using parallel coordinates (see Appendix B). He thus sought to overcome parallel coordinates limitation that dimensions are order dependent. This work effectively demonstrated the utility of projecting to a richer set of projections and visualizing the results using a richer set of tools.

Wegman and Shen (1993) proposed an approximation method to Asimov's winding method that was simpler and more computationally efficient at projecting to either one or two dimensions. This is the tour method that I used in this work.

3.2.3 Image Grand Tour (IGT)

Wegman et al. (1998) provided the initial description of the image grand tour (IGT). The goal of this method is to preserve the original lattice topology when using the grand tour to explore multi-spectral image data. In this work, they examined eight-band electro-optical data with the goal of constructing a classifier for detecting unexploded ordinance or land mines. Since the mines were characterized by their shape in the image as well as by their spectral signature, it was critical to preserve the original topology of the data in order to understand the data.

Figure 3.5 shows an example of the application of the IGT to the problem of reconstructing and thereby recovering rock art created by paleo-Native Americans. In this example, we dealt with a photograph related to the painting of a human figure presented in Kirkland and Newcomb (1967). However, in this photograph, taken more than 30 years after the publication of the painting, the figure has almost completely faded and is no longer recognizable in the photograph (see left of Figure 3.5). While the IGT did a good job in recovering the original figure (see right of Figure 3.5), other methods for processing this photograph have also been successfully demonstrated.

Since 1998 the IGT has been applied to a number of domain areas, including

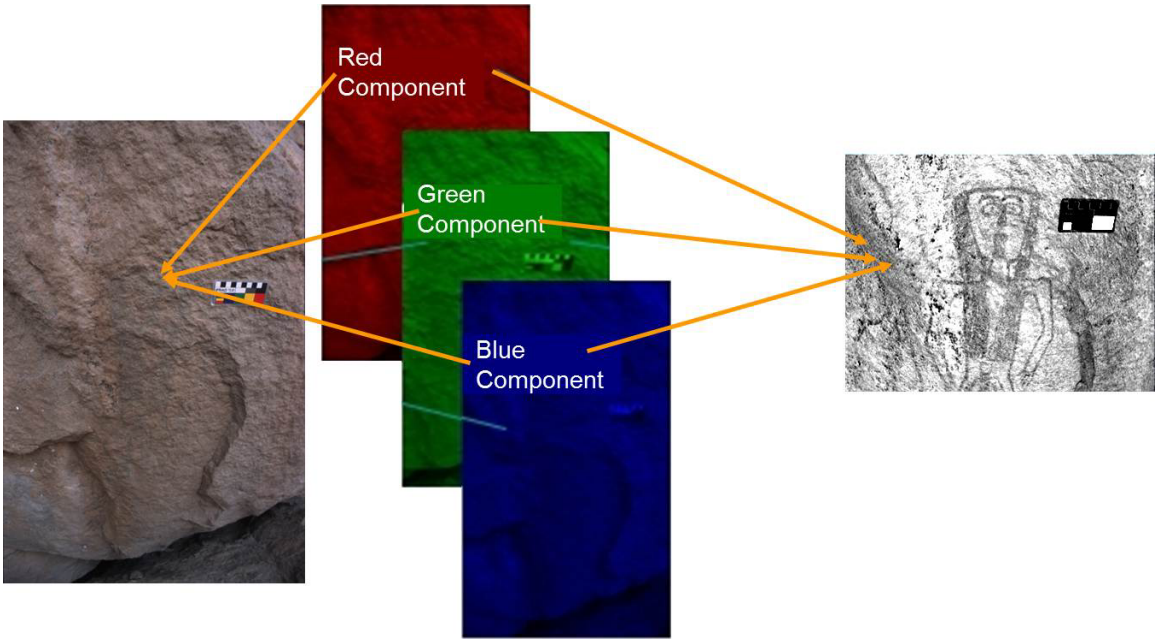


Figure 3.5: A photograph consists of three input layers, representing the colors red, green, and blue (middle). For the typical color rendition, these layers are equally weighted and displayed in the RGB color space (left). In the IGT, the three layers obtain different weighting at each step of the tour and are projected into a one-dimensional gray-scale color space (right). This image was previously published in Symanzik et al. (2007) and is republished with permission.

multi-angle imaging spectroradiometer (MISR) images as well as rock art images (Symanzik et al., 2002). Most recently, Symanzik et al. (2007) applied a version of IGT to visualize volumetric medical image data. Using the IGT, we were able to create a single gray-scale image that showed multiple structural phenomena that had not previously been visible in a single image.

The goal of most previous applications involved discovering a spectral signature and related projection that provided the ability to visualize a specific class or classes of structural phenomena in image data. As such, these tools were useful in laboratory settings to gain understanding of a general phenomenon and/or to construct a processing workflow such as an automated classifier. However, none of the previous applications were very useful to general practitioners of a field in a day-to-day sense.

Spectral decomposition presents a unique opportunity to fully utilize the power of the IGT. Individual spectral components are functions of local bed thickness and fill velocity, both of which are unknown prior to seismic analysis and drilling. As such, it is not possible to construct a single projection that is interesting across a broad range of depositional environments. In fact, it may not even be possible to construct a single linear projection that is useful across the entirety of a single data volume Given this fact, the IGT represents a useful tool not just for researchers and system developers; it has the potential to be useful as a daily tool for the practicing exploration geoscientist.

Given this opportunity, I applied the canonical IGT to interpret seismic data (Wallet and Marfurt, 2008). Using images from a spectral decomposition extracted about a picked seismic horizon, we demonstrated that the IGT was useful in mapping channels and other architectural elements of a fluvial-deltaic system. This work demonstrated one difficulty in applying the IGT to seismic interpretation. While multiple images were produced that were useful in understanding the channels, it was not clear how to best combine these separate images to produce a single, unified interpretation.

3.2.4 The View Locked Color Image Grand Tour (VLCIGT)

The problem of multiple images from the IGT was addressed by the development of the VLCIGT (Wallet, 2008). Designing a workflow that integrates the data from multiple views generated by the IGT is an important step in producing a useful method for geoscientists.

A straightforward method would be to discover views individually as is currently done, and then to integrate three views together as the component channels of a

RGB color model. Such a naïve approach is simple to develop, and it tends to lead to useful images. However, integration of separately derived images does not allow for the ready incorporation of previously found information in the continued search. Specifically, the interpreter would need to constantly refer to previous views to avoid rediscovering the same structure. Furthermore, it is difficult to understand the interaction of structure during the projection search process since the combined view is not presented until after the IGT is completed.

In the VLCIGT, the interpreter begins the process by doing a standard IGT, changing all three channels (RGB) in a like manner, in effect applying IGT to the gray component. Once a view that contains features that are useful in the interpretation process is discovered, the interpreter then fixes or "locks" that view to the red component. The IGT is then continued, changing the green and the blue components in a like manner, effectively doing a tour in the cyan component against a red component background of the previously locked view. In this manner, newly discovered features can be seen in the context of the previously discovered features. When a new view of interest is discovered, the interpreter then locks the view to the green component. The IGT is then continued with only the blue component being modified. By doing this, I am able to delineate subtle features by retaining previously interpreted features and accounting for this in the later stages of the workflow.

3.3 Application

3.3.1 Study area

The reservoir that is the subject of this study is a the Oligocene age Middle Frio formation of south Texas, USA. This reservoir is composed of a fluvial deltaic system

combined with primarily growth faults and associated rollover anticlines. The Middle Frio formation is characterized by complex fluvial systems. This system combined with significant growth faults has resulted in considerable bypassed pay.

Current work in this region is thus focused upon mapping previously untapped reservoir rocks to locate hydrocarbon reserves that are left in place. El-Mowafy and Marfurt (2008) focused upon the structural interpretation of the reservoir. My goal in this work was to provide and demonstrate a novel tool that when combined with a careful interpretation could be used to do a mapping of the complex architectural elements that comprise the fluvial system.

To demonstrate the utility of my methodology, I used a poststack, time-migrated 90 square-mile data set acquired by Union Pacific Resources (UPR) and processed by Western Geophysical. This dataset was provided for use by the University of Oklahoma thanks to the generousity of Anadarko Petroleum Corporation.

3.3.2 Results

I applied the VLCIGT to spectral decomposition attributes extracted from the UPR seismic data. To do this, I used an interpreted seismic horizon that was interpreted at the base of a sequence of significant channels. The data set was then flattened using this horizon, and horizon slice was extracted at approximately 300 ms above the interpreted horizon. This horizon slice of the seismic data is shown in Figure 3.6. Figure 3.7 shows a representative channel in the seismic data at the horizon of interest to demonstrate the quality of the data. Figure 3.8 shows the coherence and SRGB (Laake and Wallet, 2013) attributes calculated upon the horizon slice of interest. Spectral decomposition attributes were then extracted using a matching pursuit decomposition algorithm (Liu and Marfurt, 2005). I then chose to proceed

using spectral decomposition attributes from 10 to 80-Hz in 10-Hz increments. The corresponding spectral magnitudes were then extracted along the same seismic horizon shown in Figure 3.6. These images form the basis for the analysis and are shown in Figure 3.9.

The extracted images of the spectral components in Figure 3.9 exhibit considerable acquisition footprint. Footprint is common when dealing with many seismic attributes. We can also see a great deal of geological information including a large number of channels. These channels are apparent in all the images shown. It is unclear, however, what information in these images is redundant and what is complementary. The noise as well as the large number of images makes interpreting with this information a difficult task.

In order to develop a single, explainatory image for use in interpetation, I used the VLCIGT method with the images in Figure 3.9 as input. Figure 3.10 shows the first three principal components as a false color image and should be taken as the current state of the art prior to this work. The first iteration of the IGT process resulted in the image show in Figure 3.11. This single, grayscale image has captured most of the channels that are visible in the nine input images. However, when I constructed this image, I was aware that it did not completely capture all information that would be useful for interpretation.

In order to extract more information, I locked the first IGT image in the red component of the display, and I continued to run the IGT with the other two components being allowed to change. In doing this, I developed the image shown in Figure 3.12. This image preserves all of the detail visible in the previous image while revealing additional channels that had not yet been captured. Many of the previous channels are more clearly defined and thus easier to interpret.

After constructing the image shown in Figure 3.12, the final stage of the VLCIGT involved continuing the tour in the blue component of the display. The result is the image shown in Figure 3.13. This image clearly delineates many channels such that they are easy to track and interpret.

3.4 Limitations

The IGT and the derived VLCIGT rely upon the focus and attention of the interpreter. While the tour is running, the interpreter is required to entirely devote his or her effort to the task, potentionally leading to fatigue that may lead to errors in the process. Furthermore, the reliance upon the skill of the user also means that the deficiencies in skill can translate to shortcomings in the results. Color perception also varies with individuals with most interpreters better able to see edges in monochrome images. Additionally, approximately 10% of the male population suffer from some form of color blindness.

3.5 Conclusions

The results of spectral decomposition contain significant information that is valuable in seismic interpretation. However, capturing the key features imbedded in such is challenging. For this reason some form of dimensionality reduction that reduces multiple images that result from spectral decomposition and form a single image is required.

While principal component analysis (PCA) reduces dimensionality, it suffers a number of significant drawbacks. Its implied definition of signal and noise is not necessarily universally appropriate for all interpretation tasks. Additionally, since

valuable information related to the spatial nature of seismic data is ignored, the results do not necessarily capture features of interest.

The Image Grand Tour (IGT) offers a way to do dimensionality reduction of spectral decomposition components that captures the interpreters expertise and preserves the spatial information present in seismic data. My additional development of the View Locked Color Image Grand Tour (VLCIGT) provides a method to construct complex color images that elucidate a large amount of geological information in a clear and easy to interpret manners.

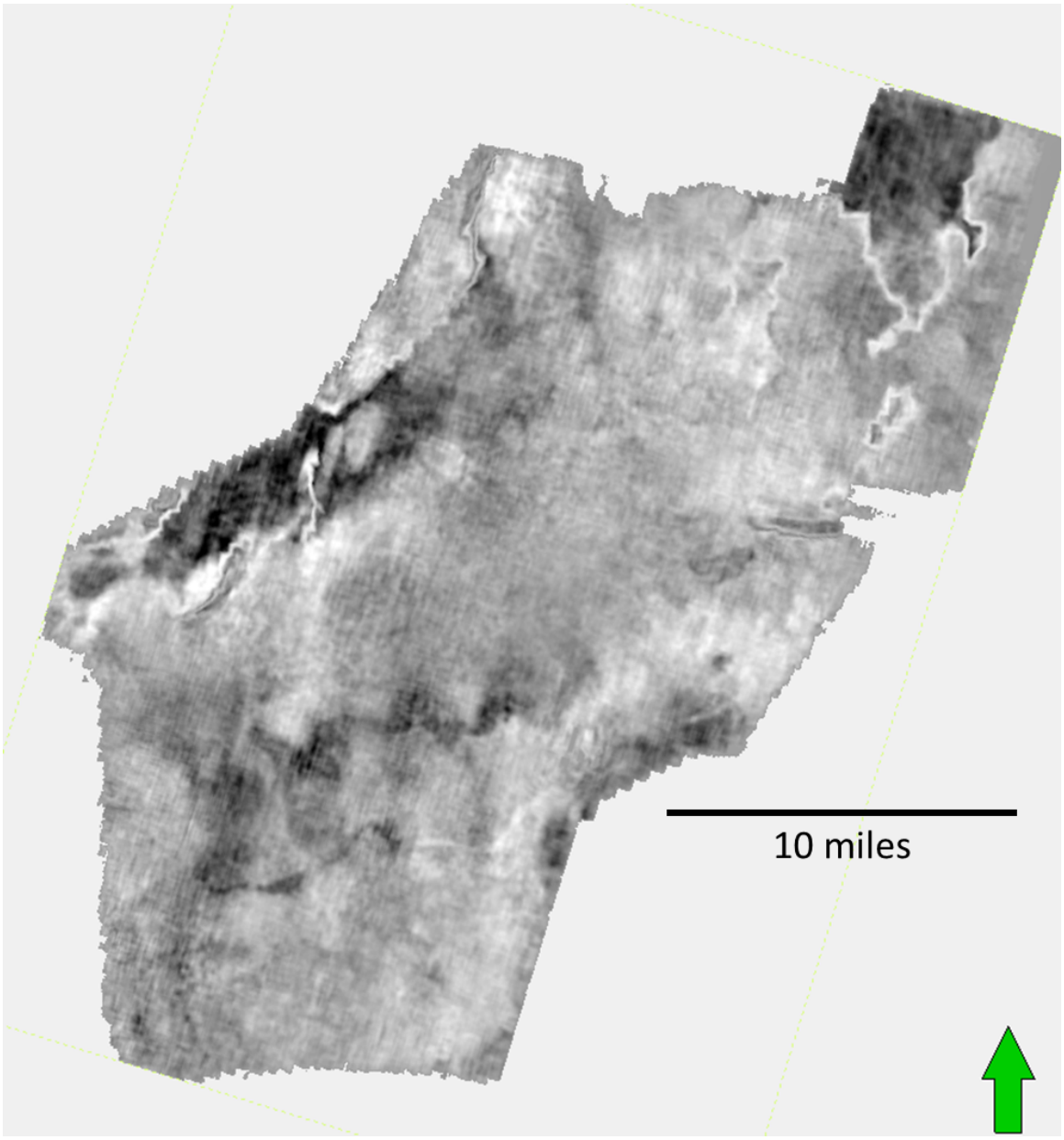


Figure 3.6: A horizon slice of the seismic data used in this study. Note the significant presence of channels including a prominent set of channels from the evolution of a meandering channel in the southwest portion of the image.

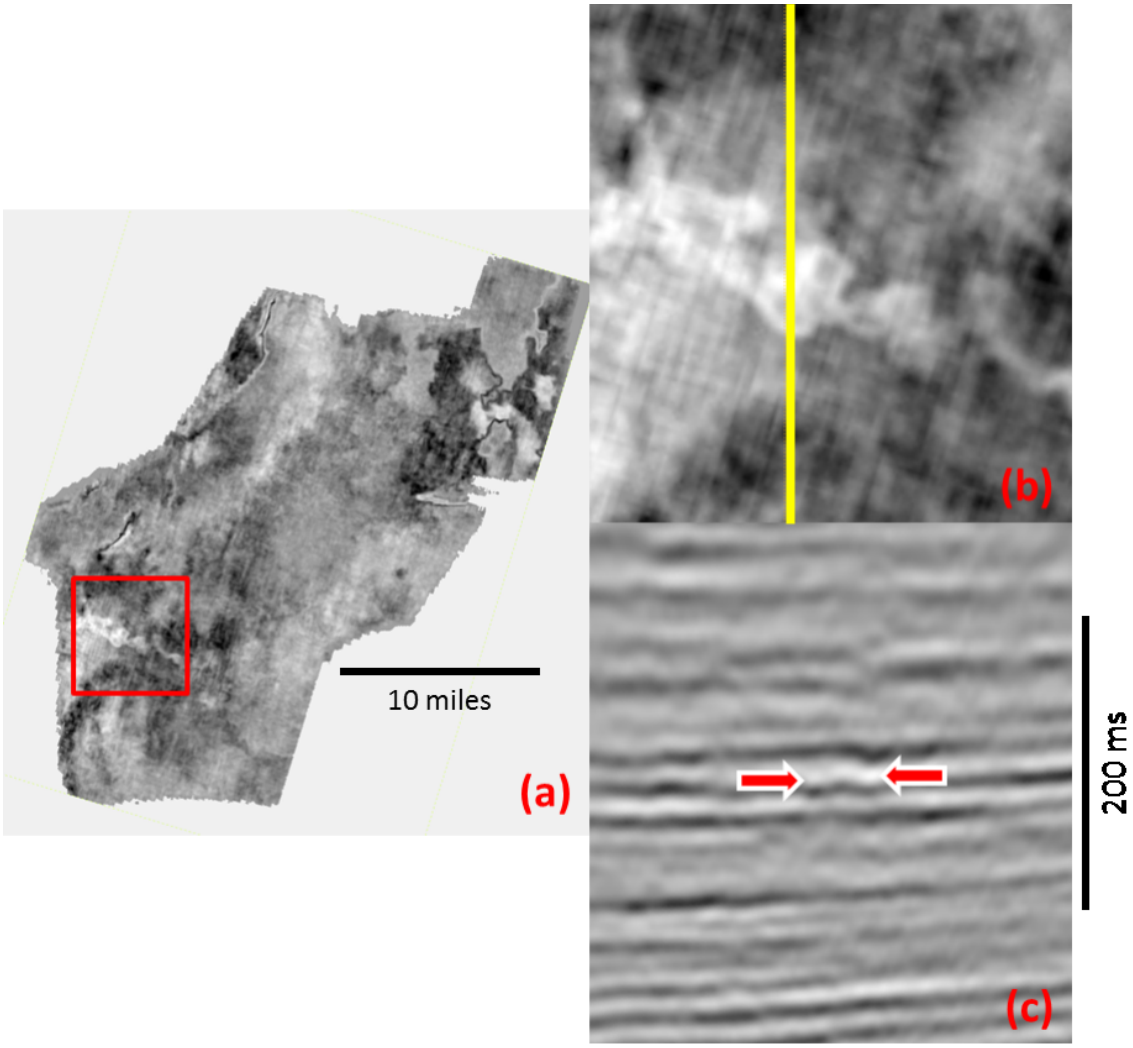


Figure 3.7: A representative view of a channel in the data set demonstrating the relatively poor data quality.

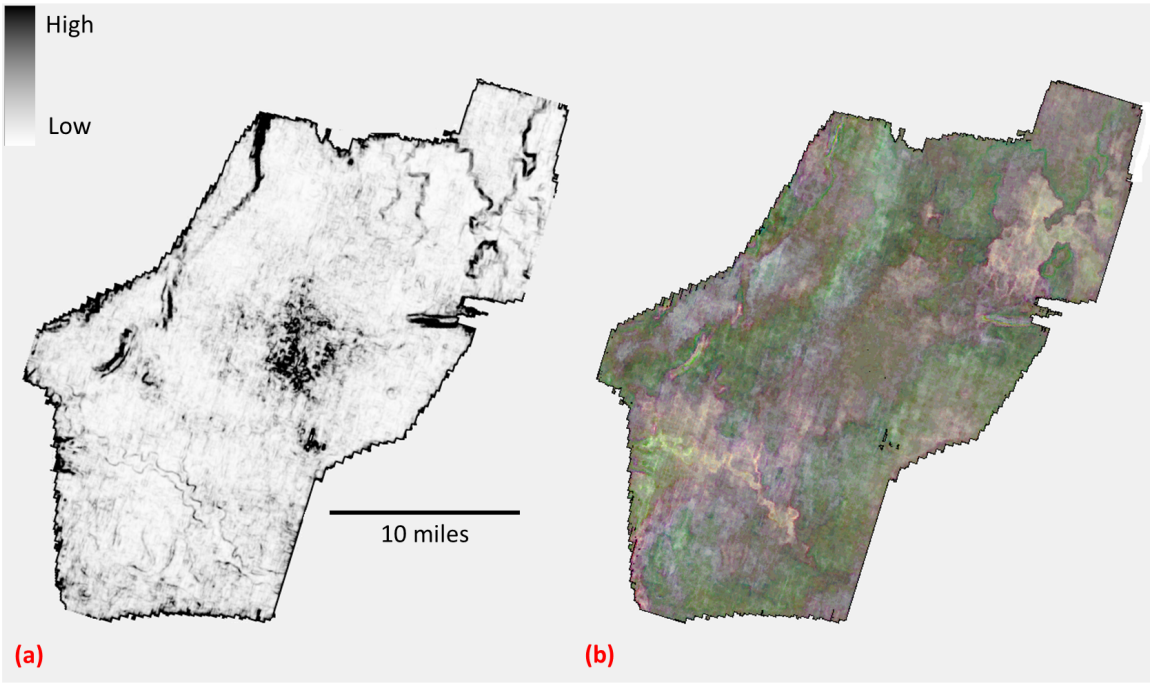


Figure 3.8: Two canonical attributes to establish a baseline of performance.(a) shows coherence while (b) shows the SRGB attributes (Laake and Wallet, 2013). Both images shows some evidence of channels though the systems are like clearly evident. Furthermore, coherence appears heavily corrupted by the presence of acquisition footprint.

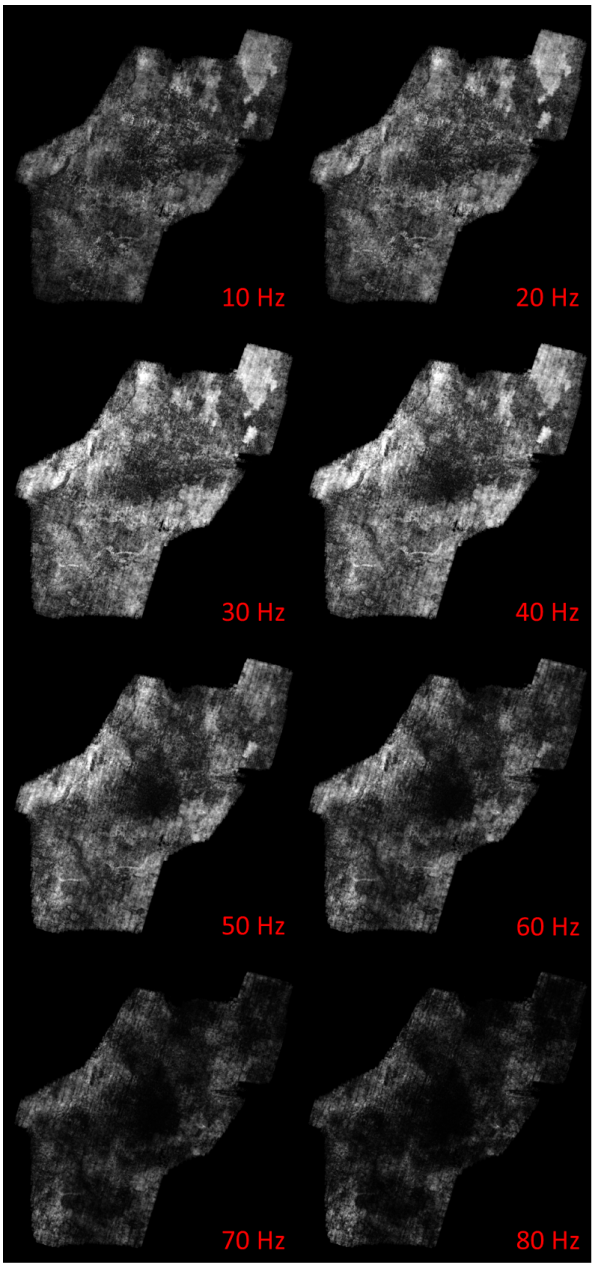


Figure 3.9: Horizon slices through eight spectral component volumes. Images indicate a large number of channels. Some of the information in the different images is likely redundant while other information may be complementary. Additionally, heavy aquisition footprint is quite evident throughout the images.

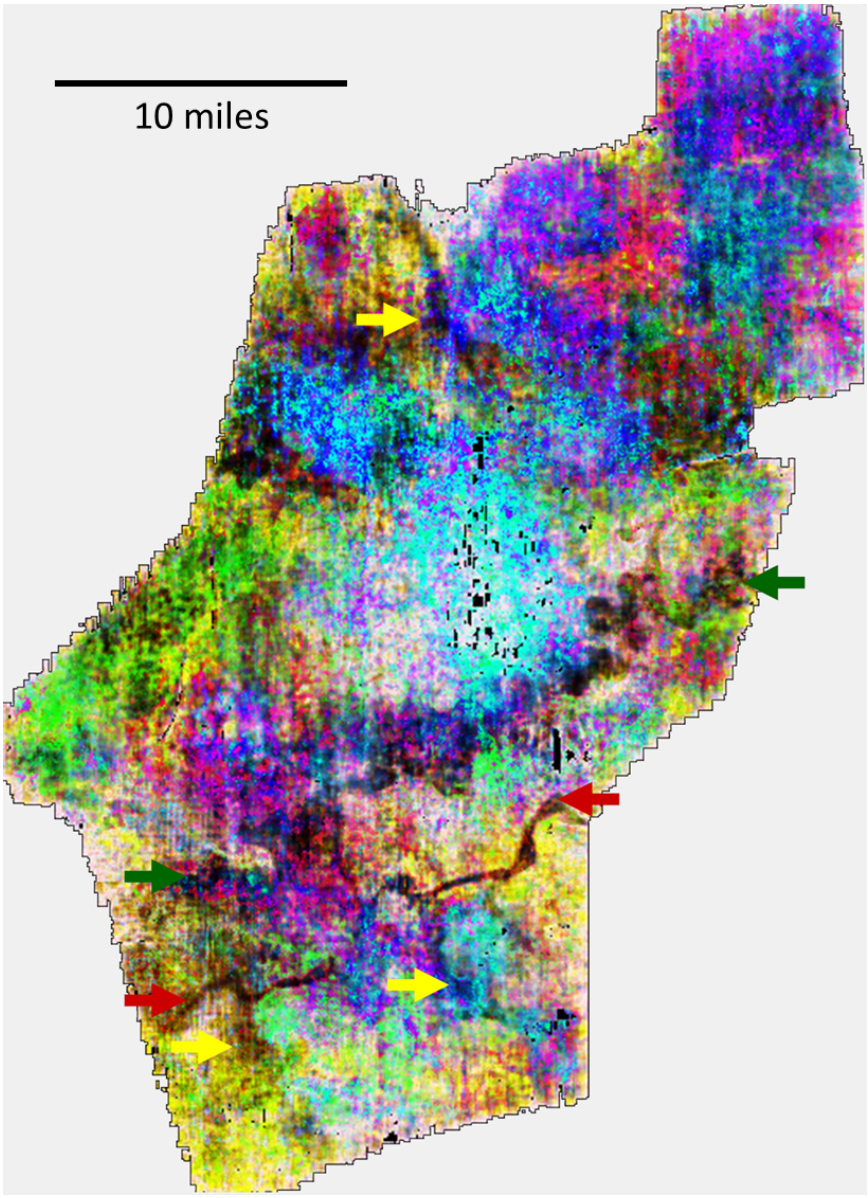


Figure 3.10: False color image composed of the first three principal components. Two large channels are indicated by the red and green arrows. Several smaller channels are indicated by the yellow arrows. Strong acquisition footprint is evident in the NS stripping across the image.

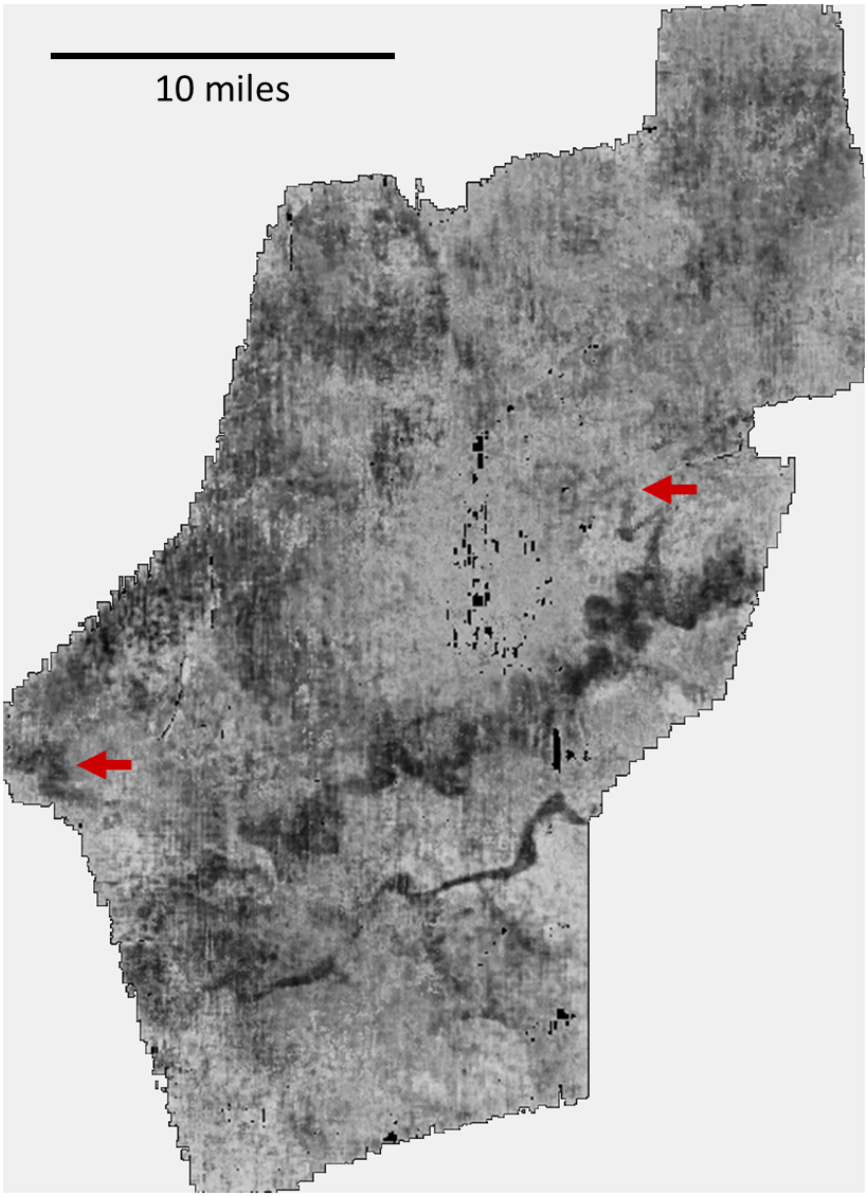


Figure 3.11: This grayscale image was discovered using the IGT. Note that all structure visible in the false color PCA image is visible in this single component image. The red arrows denote channels that are much more clearly imaged than previously.

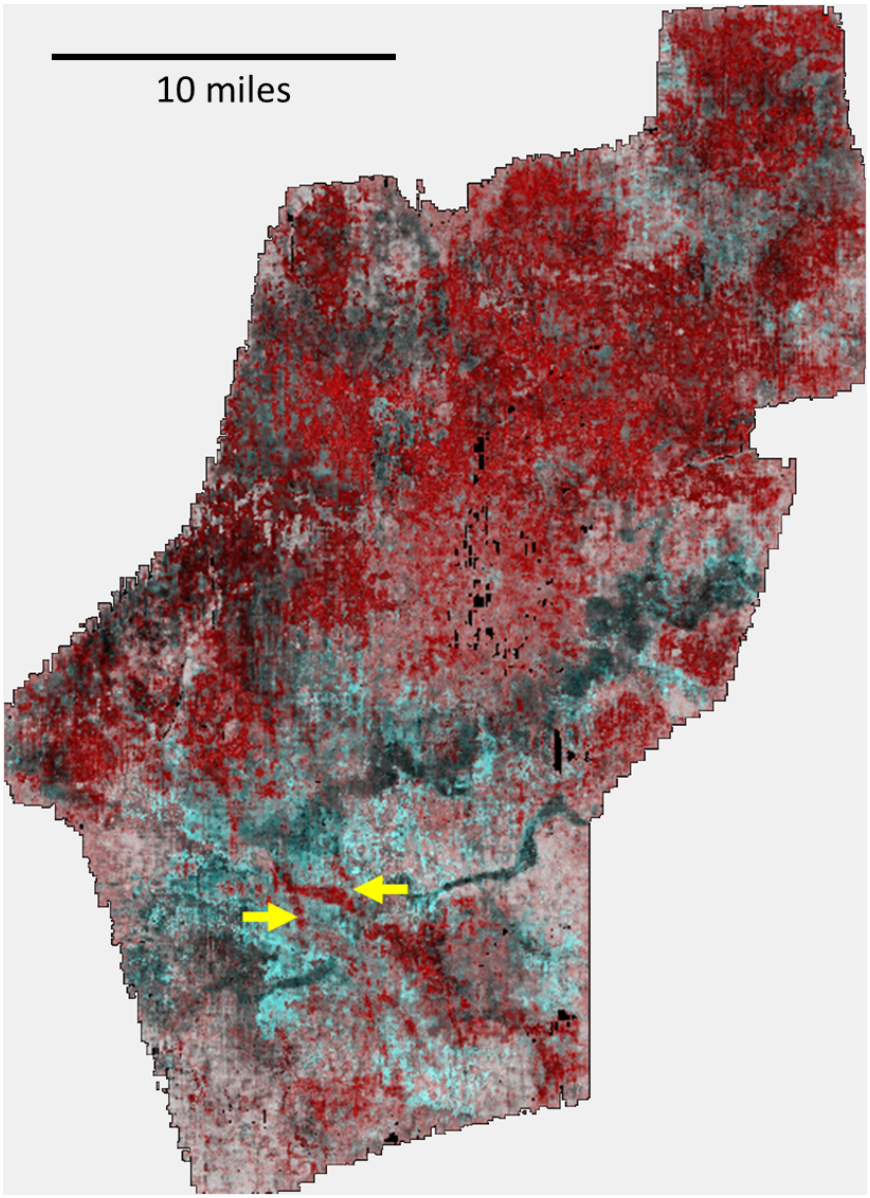


Figure 3.12: This image resulted from continuing to run the IGT with the red channel fixed on the previously discovered image. Distinct channel structure, denoted by the yellow arrows, was found overlaying the previously known major channels.

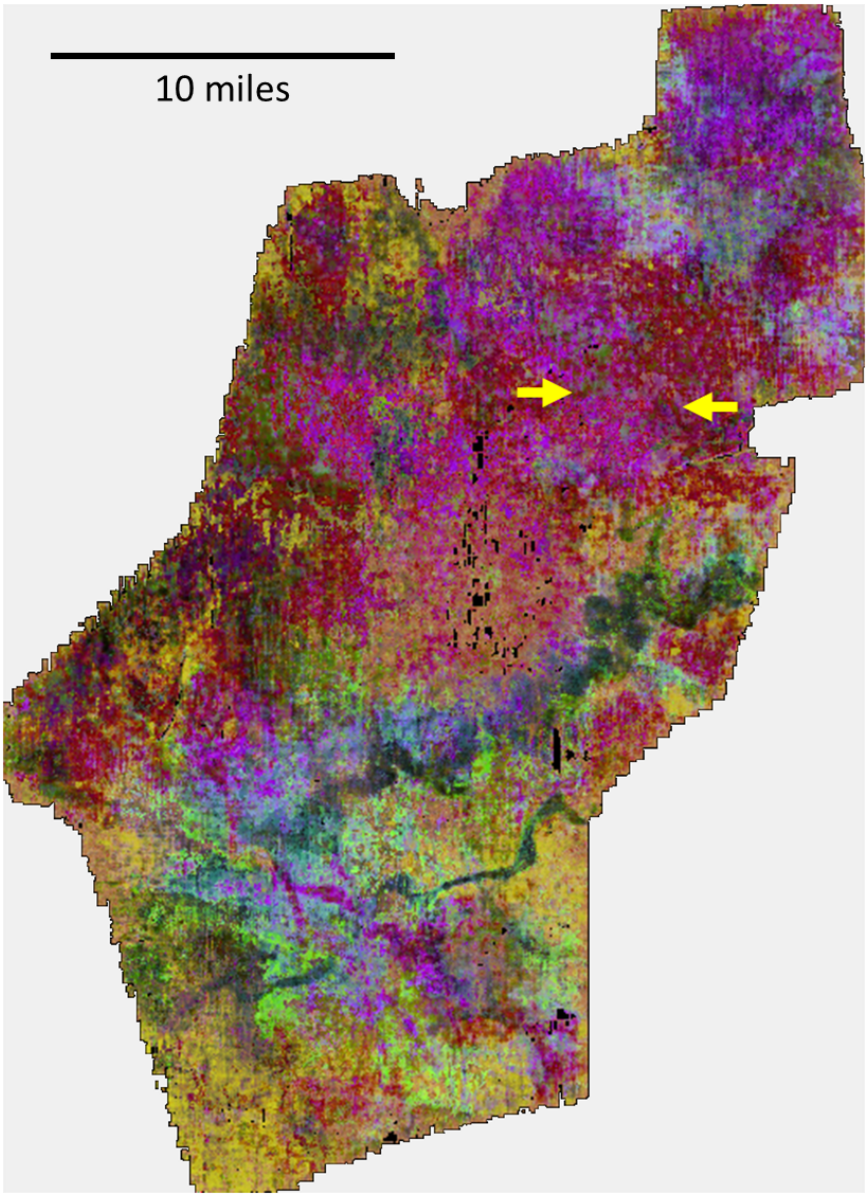


Figure 3.13: Continuing to run the IGT with the red and the green channels fixed uncovered other, more subtle structure. In this view, small channels denoted by the yellow arrows are clearly seen.

CHAPTER 4

Latent Space Modeling of Seismic Data: An Overview

This article was previously published in *The Leading Edge* (Wallet et al., 2009). It appears as published with minor formatting changes to accommodate the venue.

4.1 Introduction

Modeling of seismic data takes two forms, those based on physical or geological (phenomenological) models and those that are data driven (probabilistic) models. In the phenomenological approach, physical and geological models are tied to seismic data either through geological analogues or principles of structural deformation and sedimentary deposition. The results are then compared to the observed data, and the model is iterated as necessary to improve agreement. In contrast, probabilistic modeling looks at patterns in the data. The data could include raw seismic observations or seismic attributes. Probabilities can then be assigned to observations or potential observation; however many common techniques such as neural networks and clustering do not explicitly take this step.

While phenomenological modeling has the strength that it is tightly linked to geology, it is a hypothesis driven approach and lacks the flexibility of more exploratory, data driven methods. Furthermore, the probabilistic approach has attractive properties in that it can provide a strong quantitative assessment of reservoir uncertainty.

However, probabilistic modeling of seismic data can become mathematically infeasible due to its high dimensionality introducing high levels of statistical uncertainty.

(Wallet and Marfurt, 2008) observed that each seismic attribute can be represented as a dimension of a d-dimensional space in which the data reside where d is the number of attributes. A common method for dealing with high dimensional data is to reduce the dimension using a linear projection (Guo et al. (2006)). In modeling spectral decomposition of seismic data, the attribute space may be several hundred dimensional. In the concrete example presented later in this paper, we model 16 sample vertical windows of seismic traces. Each of these 60 ms waveforms, represented by a 16 dimensional vector, resides in a 16 dimensional attribute space. Throughout the rest of this paper, we will refer to waveforms, and these should be understood to be observations in attribute space.

The approach discussed in this paper is to model the data as a lower dimensional manifold representation of a latent space embedded in attribute space. A manifold can be thought of a space that can be approximately mapped into a Euclidean space. For instance, a one dimensional manifold can take the form of a line or a curve that can be straightened out to form a one dimensional Euclidean space. A latent space is a lower dimensional manifold embedded in attribute space that approximately contains the vast majority of the probability mass. If a latent space model is correct, virtually all observed waveforms in a seismic data set should fall close to the latent space. Figure 4.1 shows a pedagogical example of a one dimensional latent space in a two dimensional attribute space. In this case, the data should be mapped into the latent space by orthogonally projection with the manifold of the latent space corresponding with straightening the green line.

Figure 4.2 shows the motivation behind our effort. This figure shows two points in attribute space (waveforms) in the set of all possible waveforms. One of these

waveforms is an actual observation while the other is artificially created to be improbable. In this concrete example, it would be improbable since seismic data is band-limited, and the sudden discontinuity would appear outside of the seismic frequency band. Our approach seeks to model the regions of attribute space that are associated with plausible observations while not modeling regions associated with implausible observations. In keeping with our general philosophy of letting the data speak for themselves, the space of plausible observations, the latent space, is garnered from the data set being modeled. Hence, what is improbable is estimated based upon the data.

In summary, the goal of latent space modeling is to take our attribute data and map it into a lower dimensional space. Once the data are mapped in this way, they may be visualized as an image or used for further processing such as in pattern recognition or facies analysis. To keep things simple in this paper, we focus upon concrete methods for estimating or learning these latent spaces from a data set. In statistics and computer science, the process of gaining information from a data set is often referred to as learning, and we will choose to use this term to describe estimating the latent space from a data set. We will define these methods without giving details of their mathematics or implementation; then, we will discuss their relative merits and show some results of their application to seismic data.

We will discuss three methods of learning the latent space corresponding to the embedded manifold: self organizing maps (SOM), generative topographical maps (GTM), and diffusion maps. These methods differ in their assumptions, strengths and weaknesses. SOM learn the latent space by simultaneous clustering the data and ordering the clusters along the manifold. GTM learn the latent space by estimating a maximum likelihood solution of a constrained probability density function (PDF). Diffusion maps learn the latent space by learning the manifold defined by principal

inter-point connectivities.

4.2 Self Organizing Maps

Self organizing maps (SOM) (Kohonen (2001)) learn the latent space by a recursive clustering algorithm. An initial manifold is selected and uniformly populated with cluster centers. The observed waveforms are then recursively entered into the model in a random manner. Each observation is mapped to a neighborhood of closest clusters defined by point to cluster distances, and the clusters are subsequently updated, thereby pulling the latent space to better fit the data. It is superior to the commonly-used k-means algorithm as it assigns the ordered clusters which can be used with an ordered color map (Coléou et al. (2003)), and it is this ordering that justifies categorizing SOM as a method of latent space modeling.

While the clusters themselves are defined in the original n-dimensional space, they are mapped into a lower dimensional, typically one or two dimensional, latent space. Each waveform can be mapped into the latent space according to its nearest clusters. Since the representation is defined by this set of clusters, SOM is a form of vector quantization.

SOM has a number of strengths. It is easy to implement. Furthermore, it is relatively computationally inexpensive both in terms of memory and processing. It is also well understood, and it has been the subject of a considerable body of research and commercial software development. However, it does have a number of weaknesses. The most obvious of these is related to the initialization. The resultant model is dependent upon the initial conditions and the order in which the data are incorporated into the model. Furthermore, while SOM learns the latent space, there is no provision for learning the dimension of this space. Additionally, the theoretical basis for SOM

is weaker than for other methods. For instance, while multiple iterations through the data set can be performed, there is no proof of convergence. Finally, though different starting conditions will result in different models, there is not an obvious criterion for model comparison.

4.3 Generative Topological Maps

Generative Topological Maps (GTM) (Bishop et al. (1998)), as the name implies, learn the latent space by fitting a probability density function (PDF) to observed waveforms. Like SOM, GTM starts with an initial latent space, uniformly populated with clusters. However, the clusters in GTM are themselves parametrically defined as multivariate Gaussian distributions. In this way, the PDF is a Gaussian mixture model (Titterington et al. (1985)). The initial model is then updated using an expectation-maximization (EM) algorithm (McLachlan (2008)). The clusters are constrained to a uniformly spaced grid which is projected onto a changing nonlinear manifold with the EM algorithm adjusting the manifold position in data space. The EM algorithm is an iterative optimization algorithm that is guaranteed to converge to a possibly local maximum point in the likelihood surface. In other words, the latent space calculated in such a way as to maximize the likelihood of the data.

GTM was developed to address several weaknesses in SOM, and it thus has a number of notable strengths. Firstly, it is based upon Bayesian first principles, and it is proven to converge. Like with SOM, GTM can possibly converge to different solutions depending upon initialization. However, different GTM models may be assessed and compared based upon likelihood. Furthermore, since GTM is a generative model, it may be used to generate random observations that could be useful for geostatistical applications. Finally, since GTM is based upon mixture models, it should be possible

to formulate a Bayesian solution to the problem of latent space modeling.

GTM does have a number of weaknesses. Like SOM, the dimension of the latent space must be decided upon a priori. Furthermore, GTM is more computationally demanding than SOM in terms of memory and processing requirements. However, recursive forms of the EM algorithm have been formulated (Priebe (1994)), and such an approach could easily be derived for GTM which could reduce the memory demands of GTM.

4.4 Diffusion Maps

Diffusion maps, also known as "spectral clustering", learns the latent space of the data based upon principal inter-point distances between the observations. Possible distance measures include cross-correlation, L1 (Manhattan distance), and L2 (Euclidean distance). Diffusion maps work by calculating the full matrix of inter-point similarities of a data set. This similarity matrix is then normalized to sum to one along each row. In this manner, the matrix thus corresponds to the diffusion probability matrix for random jumps between points, hence the name of this method. Eigenanalysis is then performed to determine the principal axes of this similarity matrix. A detailed discussion of the mathematics of this method may be found in a number of other sources (Lafon (2004)).

When using diffusion maps, the dimensionality of the manifold can be decided using the eigenvalues of the distance matrix which is a major strength of diffusion maps relative to the other methods. The other major strength of this method is that it is closed form and completely deterministic while the other methods are iterative and subject to their initialization conditions. Unfortunately, diffusion maps have two major drawbacks. The first is that it is extremely computationally demanding both

in terms of processing and memory. The principal bottleneck in this regard is the need to perform an eigenvalue decomposition of an n by n matrix where n is the number of observed waveforms. For a typical dataset, memory requirements to store this matrix could easily reach the 100's of gigabytes with computational requirements running to several multiples of this. Large decimation of the dataset is thus often necessary. Unfortunately, this runs afoul of the second major drawback of this method. The mapped latent space is defined by the eigenvectors with each observed waveform used in the eigenvalue decomposition having a corresponding vector. Thus, observations that are not in the training data are not defined in the latent space model! Fortunately, a method for mapping arbitrary observations into this space has been developed though this can be complex to implement.

4.5 Application

We demonstrate the concept of latent space modeling by applying SOM and GTM to a seismic land survey acquired in the eastern part of the Anadarko Basin in central Oklahoma. We targeted our analysis upon the Middle Pennsylvanian age Red Fork Formation. The interpretation challenge is to map a series of incised valleys (Peyton et al., 1998).

To define our attribute space, we begin by interpreting a horizon on the Upper Red Fork Formation. An image of the seismic amplitudes corresponding to 28ms below this horizon can be found in Figure 4.3. An interpretation of this formation based upon seismic attribute analysis is shown in Figure 4.4. We then extracted 16 samples from each trace starting at 28ms below our interpreted horizon. These waveforms were then considered as a 16 dimensional attribute space. We then ran both SOM and GTM using implementations in Matlab upon this data set with the

goal of learning a two dimensional latent space, and we examined the results using a two dimensional color mapping.

Most commercial applications of SOM use a one dimensional latent space, with the waveforms plotted against a one dimensional "rainbow" color bar. Currently, there are no commercial implementations of GTM for seismic analysis. In our examples of both SOM and GTM, we use a two dimensional latent space, and map the waveforms against a two dimensional HSV color map.

Figure 4.5 and Figure 4.6 show resultant images for single runs of SOM and GTM respectively. These figures also show the interpretation contained in Figure 4.4 overlain upon the images derived using the latent space projections. Examining these images shows that the previously interpreted features are easily seen using both latent space methods. Within these features is visible additional richness that is likely to be useful in more complex analysis. In addition, both methods show what we interpret as a fan feature across the northern top of the primary channel.

4.6 Conclusions

Latent space modeling provides a useful tool for understanding and interpreting higher dimensional data derived from seismic amplitude and attribute data. We show the application of two latent space modeling techniques, self organizing maps (SOM) and generative topographical maps (GTM). The results show that these methods can characterize depositional features that are not easily seen using conventional seismic attributes. In addition to highlighting details within the incised valleys and overbank deposits, we are also able to visualize what appears to be a corresponding fan. Like almost all attributes, latent space modeling methods are sensitive to input seismic data quality, and thereby suffer from acquisition footprint. The rich nature of the

resulting projected data promises to be useful in well log constrained automated and semi-automated facies analysis.

While diffusion maps offer unique benefits, the method is current too computationally intensive to handle seismic data volumes. However, (Wallet and Perez, 2009) show that diffusion maps are very effective in clustering well logs to form bed set parameterization of parasequences. Currently, we are investigating using diffusion maps with a greatly decimated subset of the data as an initialization method for both SOM and GTM.

Acknowledgements

Thanks to Chesapeake Energy for use of their seismic data in research education. Additionally, we thank Kurt J. Marfurt for his advice and assistance in preparing this paper.

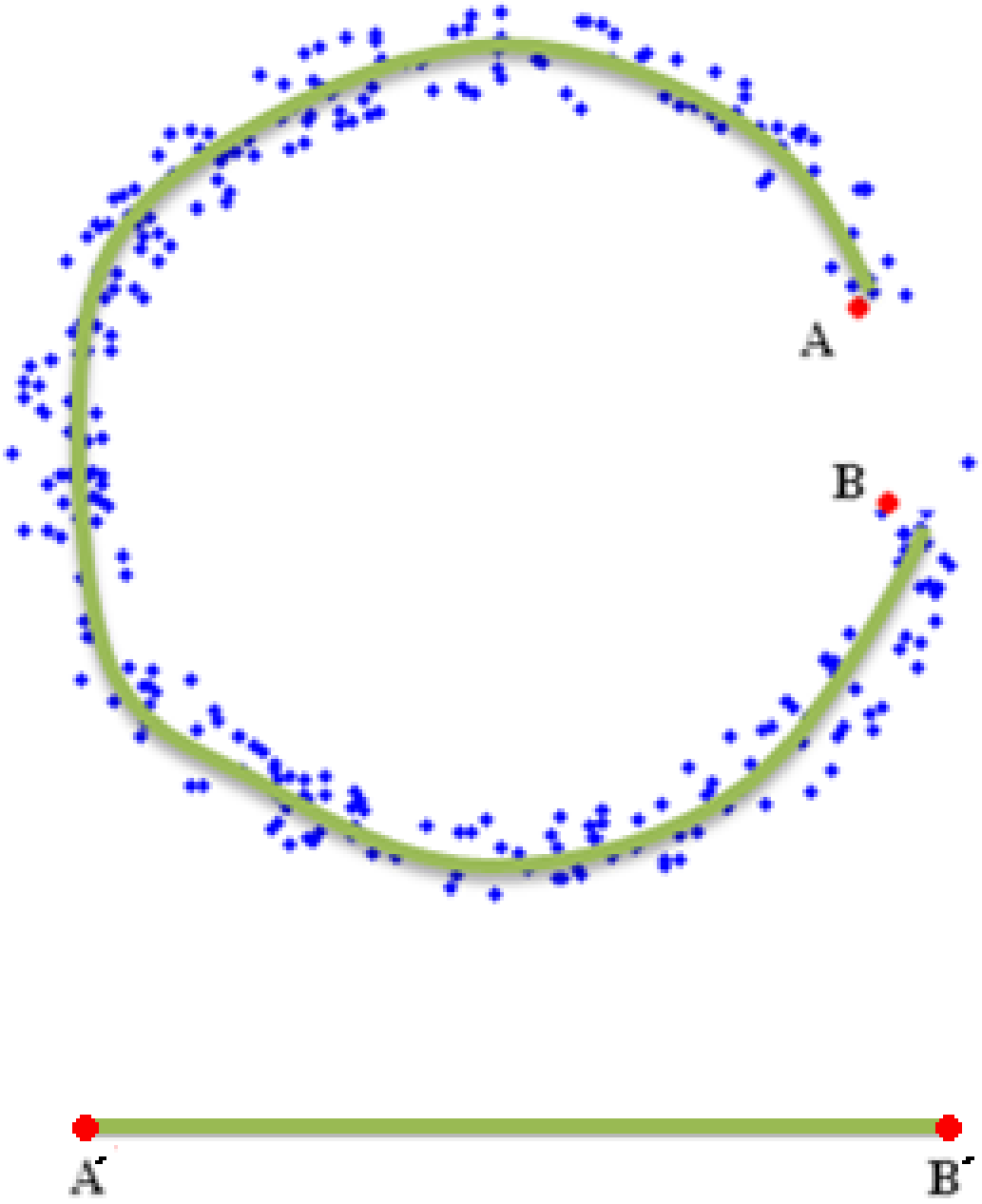


Figure 4.1: This figure shows a pedagogical example of a one dimensional latent space manifold embedded in two dimensions. Note that while points A and B are relatively close in Euclidean distance in the attribute space, they are extremely distant when mapped into the latent space as points A' and B'. The green curve represents a possible latent space that might explain this data set. A point distant from this green line would be of very low probability and would be considered implausible.

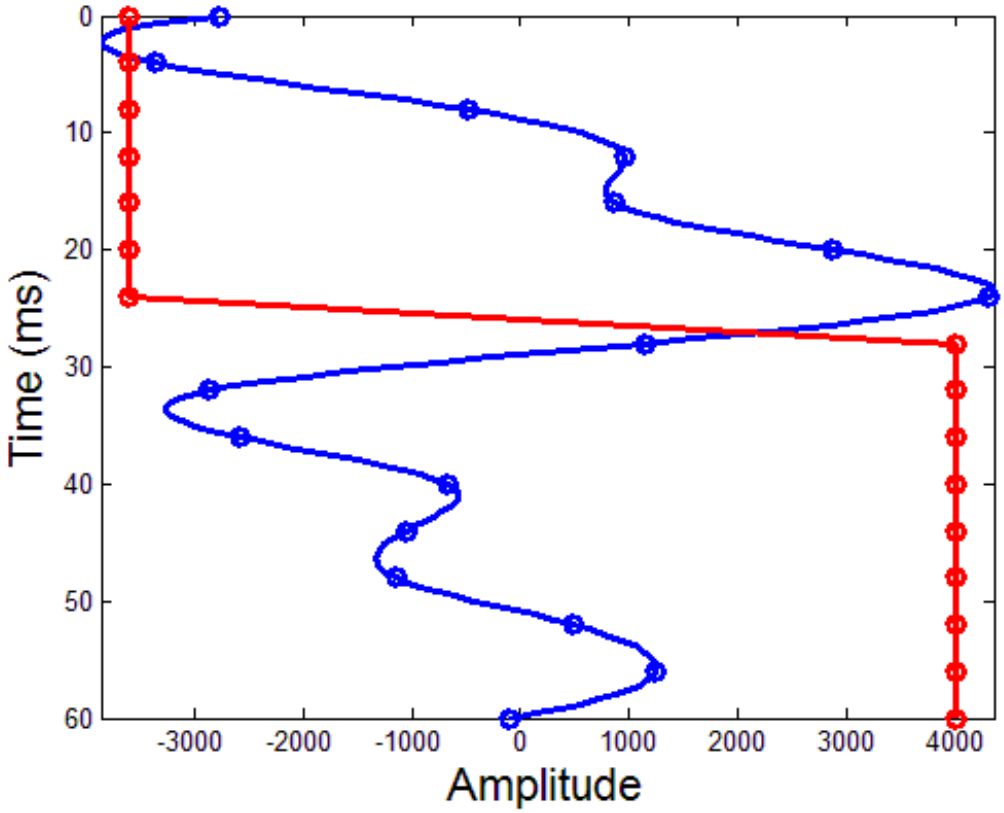


Figure 4.2: Seismic waveforms (or vectors) representing two points in the set of possible seismic waveforms of 16 samples in length. The blue segment is taken from the real data set and is entirely plausible while the red segment is artificially created and is highly improbable.

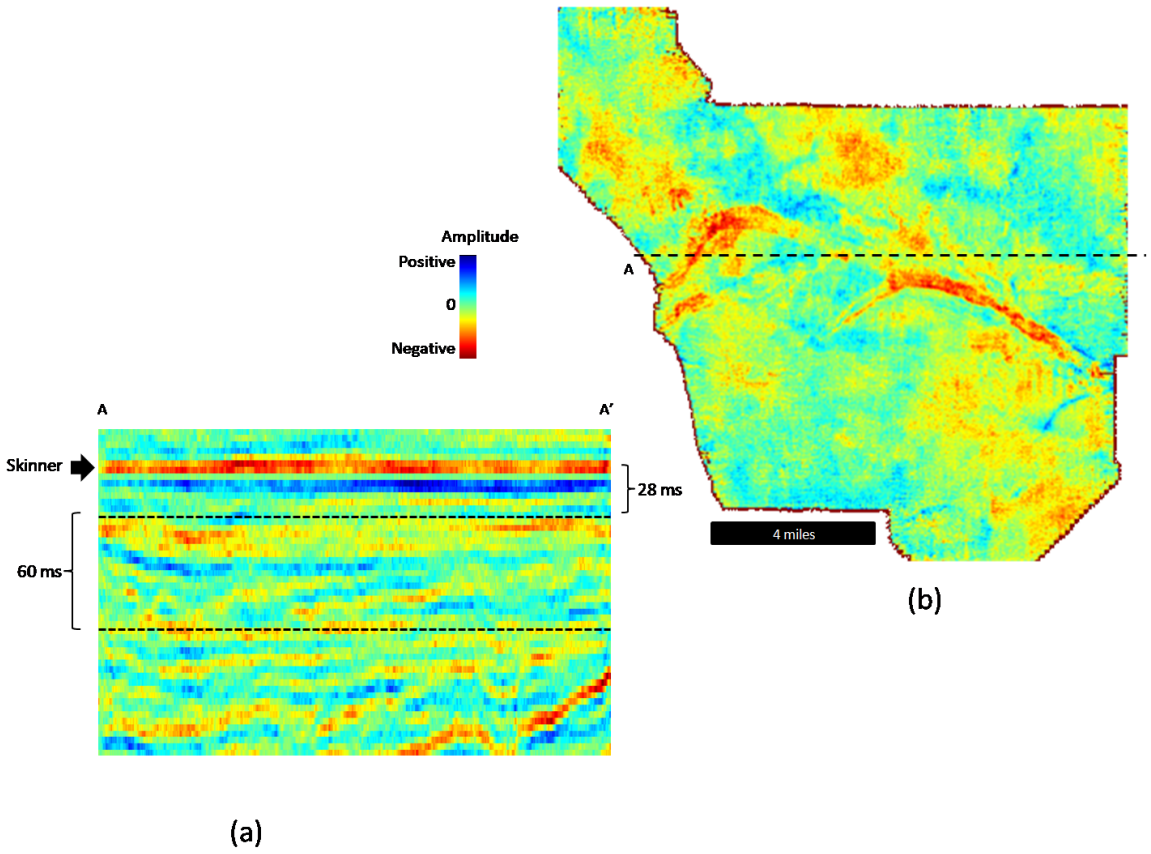


Figure 4.3: Seismic data that were modeled using SOM and GTM. (a) Vertical section through the seismic data flattened on the continuous Pink Lime horizon. The interval denoted by the yellow lines shows the extent of the waveforms we modeled. (b) Phantom horizon slice 60 ms below the Pink Lime. This represents the tops of the modeled waveforms.

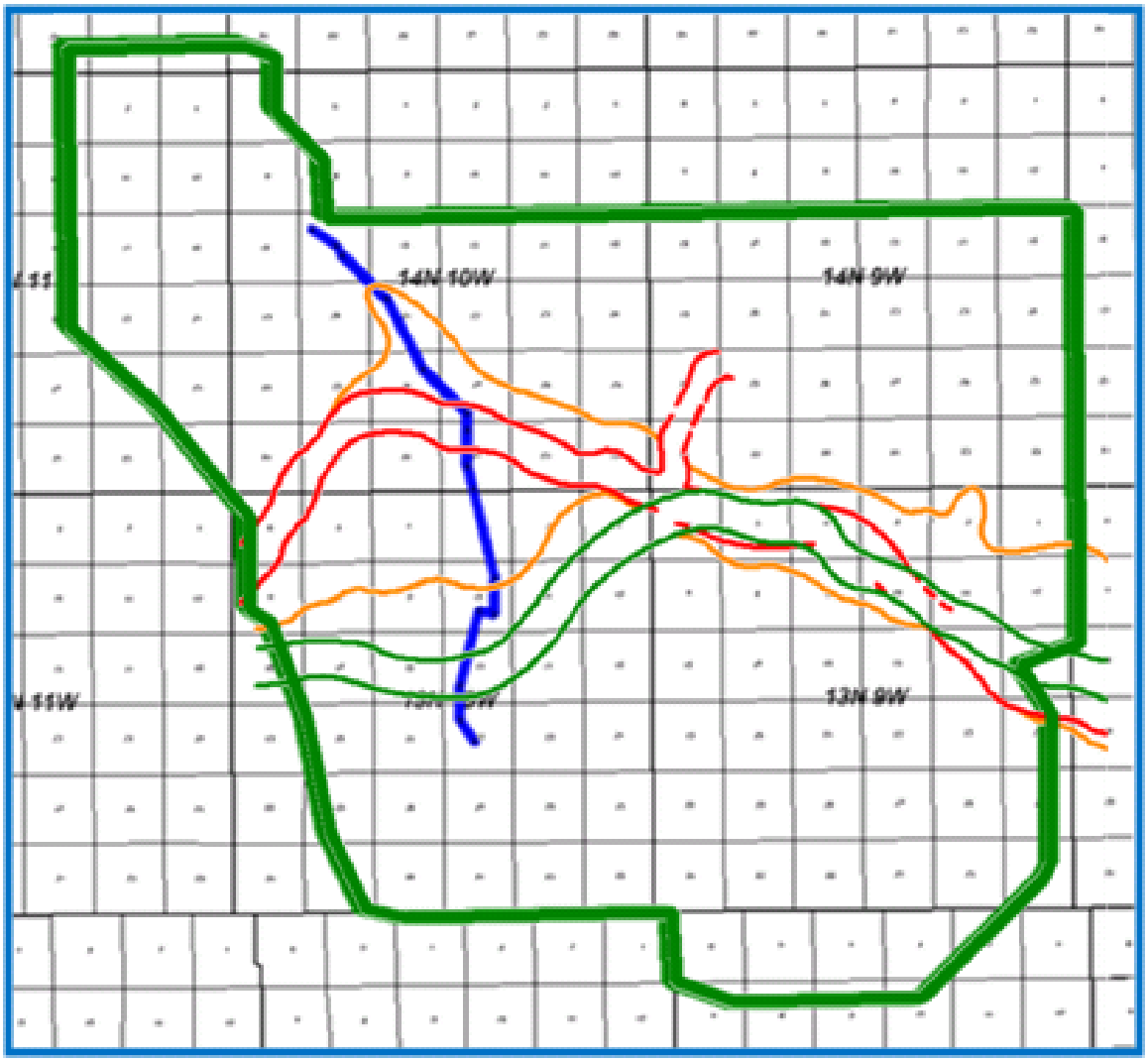


Figure 4.4: The survey area corresponding to the seismic data modeled in this paper contains a series of incised channels with varying characteristics. These channels have been previously mapped using a combination of well logs, seismic interpretation, and seismic attribute analysis. A detailed discussion of the various channels present in this system can be found in (Suarez et al., 2008).

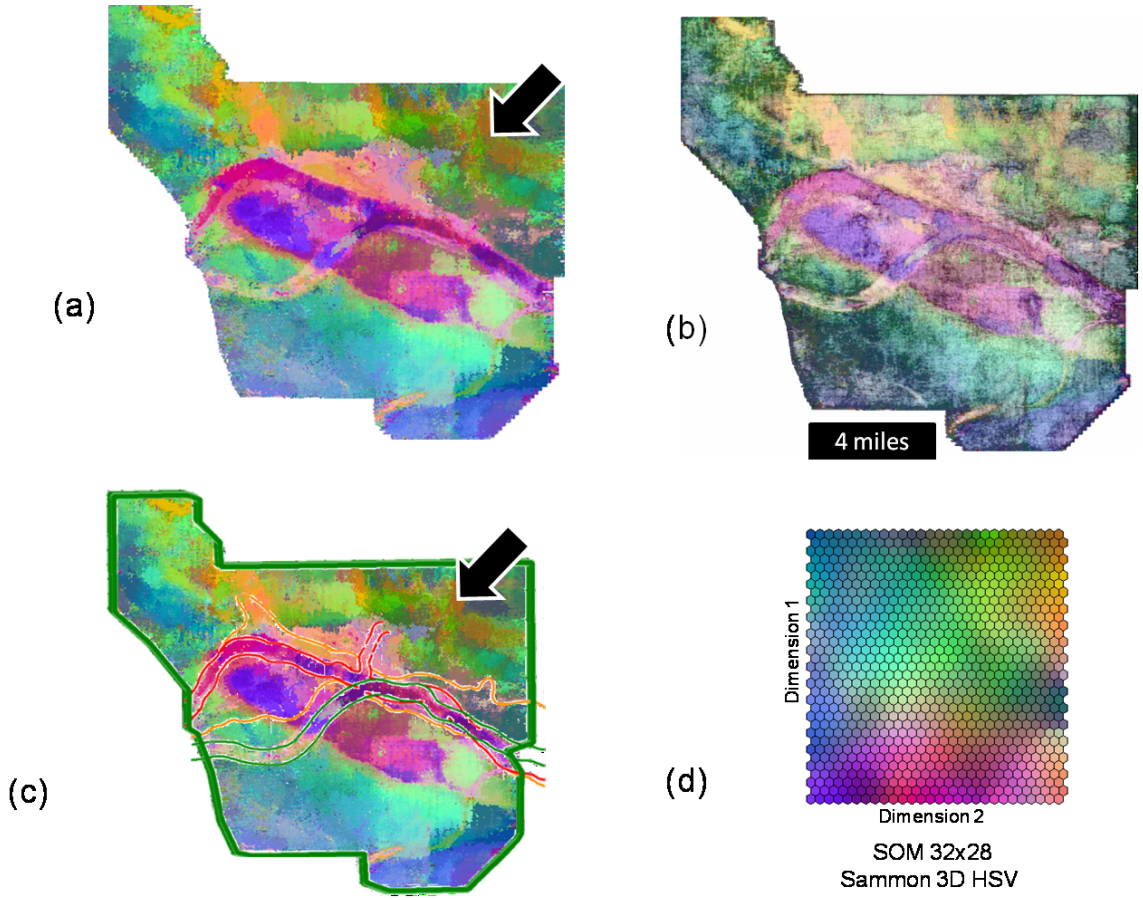


Figure 4.5: Images related to running SOM upon the data set. The new images agree with the previous interpretation while providing additional richness that promises to aid in future analysis. Additionally, the black arrows denote what we interpret to be a fan feature not previously seen. (a) The output a SOM with the latent space mapped vectors displayed as an image. (b) The SOM image blended with a coherency image. (c) The interpretation shown Figure 4.4 overlain on the SOM image. (d) The color map used in the display of the SOM image. Each hexagon represents a cluster with images (a) through (c) being colored with this color map.

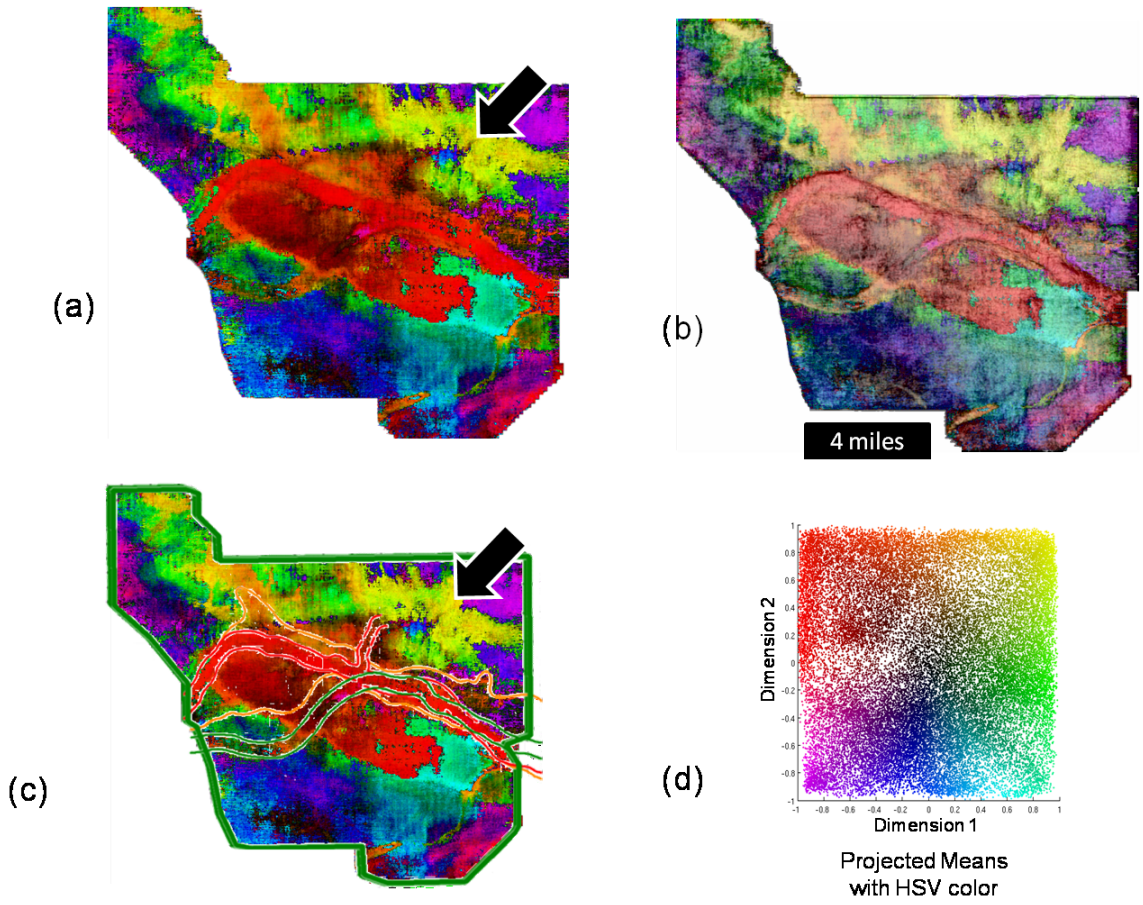


Figure 4.6: Images related to running GTM upon the data set. The new images agree with the previous interpretation while providing additional richness that promises to aid in future analysis. Additionally, the black arrows denote what we interpret to be a fan feature not previously seen. (a) The output a GTM with the latent space mapped vectors displayed as an image. (b) The GTM image blended with a coherency image. (c) The interpretation shown Figure 4.4 overlain on the GTM image. (d) The color map used in the display of the SOM image. Each dot represents a cluster with the latent space thus expressed in a discrete two dimensional space.

CHAPTER 5

Attribute expression of channel-forms in a hybrid carbonate turbidite formation

5.1 Introduction

Deepwater marine depositional systems are one of the most important reservoirs and have given rise to most of the recent conventional discoveries. Turbidite systems constitute an important class of hydrocarbon reservoirs in deepwater settings (Slatt, 2014), and considerable work has published on the characterization of deepwater turbidite reservoirs.

Because of their resemblance to common earth features such as rivers, canyons, and gullies and their strong laterally 2D (though often stacked) nature, deepwater turbidites have inspired significant study using seismic geomorphology. Posamentier (2006) completed a detailed analysis of a marine depositional system, looking at architectural elements at both shallow and exploration depths. In this work, he analyzed both vertical slices and time/horizon slices of amplitudes to illustrate channels and other elements. Additionally, he showed the value of using seismic attributes such as dip and curvature.

Braccini and Adeyemi (2011) focused upon the use of seismic attributes to map a deepwater turbidite in offshore Nigeria. In this work, they used spectral components, near and far offset limited stack amplitudes, and coherence to visualize both channels

and mass-transport complexes. They showed a number of vertical slices of the seismic data, demonstrating the 3D nature of these elements, but they only used the attributes in map views to visualize the lateral extent of these features.

While classical deepwater turbidites have been the subject of considerable study (Deptuck, 2003), significantly less work has been done in the area of hybrid carbonate turbidite reservoirs (Weimer and Slatt, 2006). Carbonates can make an excellent environment for the development of a turbidite system. This is due to their grain-rich facies that can be transported by turbidity flows (Harris and Wright, 1998). Producing reservoirs of this type include the Hasa field in Abu Dhabi, the Fateh field in Dubai, and the Poza Rica field in Mexico.

Another example of a hybrid carbonate turbidite is the Mandu Formation, off the northwest coast of Australia. Figure 5.1 shows a vertical slice through seismic data acquired in this region taken parallel to the paleo-shoreface. Evidence of channel-forms is clearly seen in this vertical slice, and even a novice interpreter could interpret many though not all of these forms. Figure 5.2 shows the same slice with a partial interpretation overlaid on the seismic.

Figure 5.3 shows a vertical slice running perpendicular to the paleo-shoreface. The most evident feature visible in this image is a series of clinoforms. An experienced interpreter can relate the internal structure of these to global eustatic changes in sea level (Figure 5.4). These clinoforms constitute the Mandu Formation, an Oligocene aged prograding carbonate shelf (Heath and Apthorpe, 1984). This image gives little information useful for mapping the architectural elements of the turbidite system.

In this chapter, I evaluate the attribute expression of a series of channel-forms in the prograding carbonate Mandu formation with the goal of visualizing the channel-form geometry in 3D as well as in conventional methods.

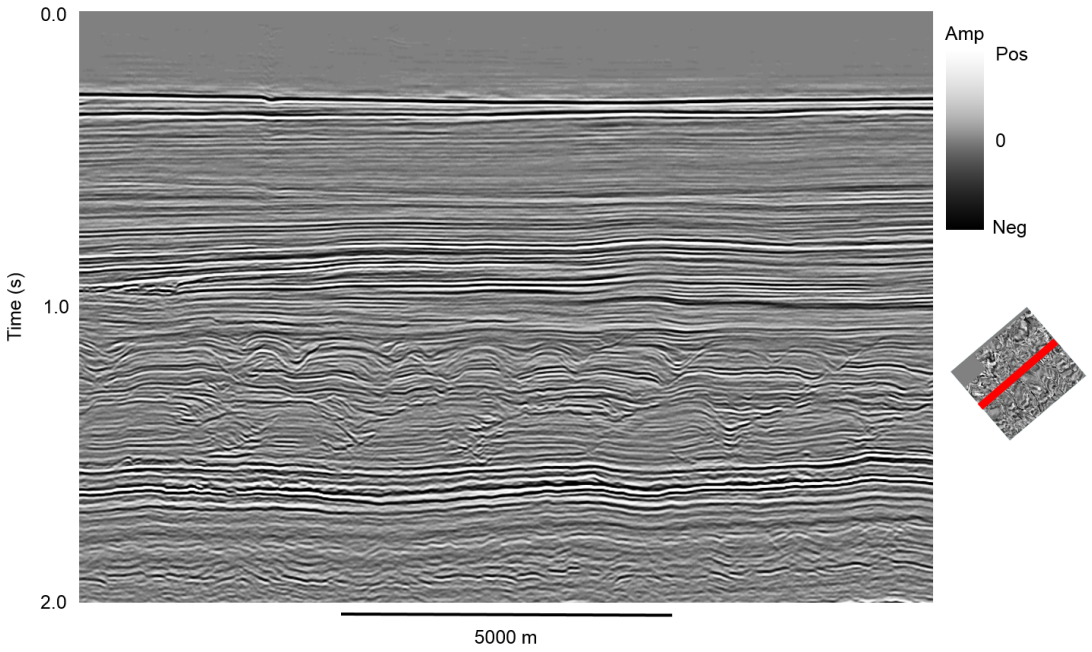


Figure 5.1: A vertical slice through the seismic data volume taken parallel to the paleo-shoreface. Evidence of channel-forms is clearly seen in this image.

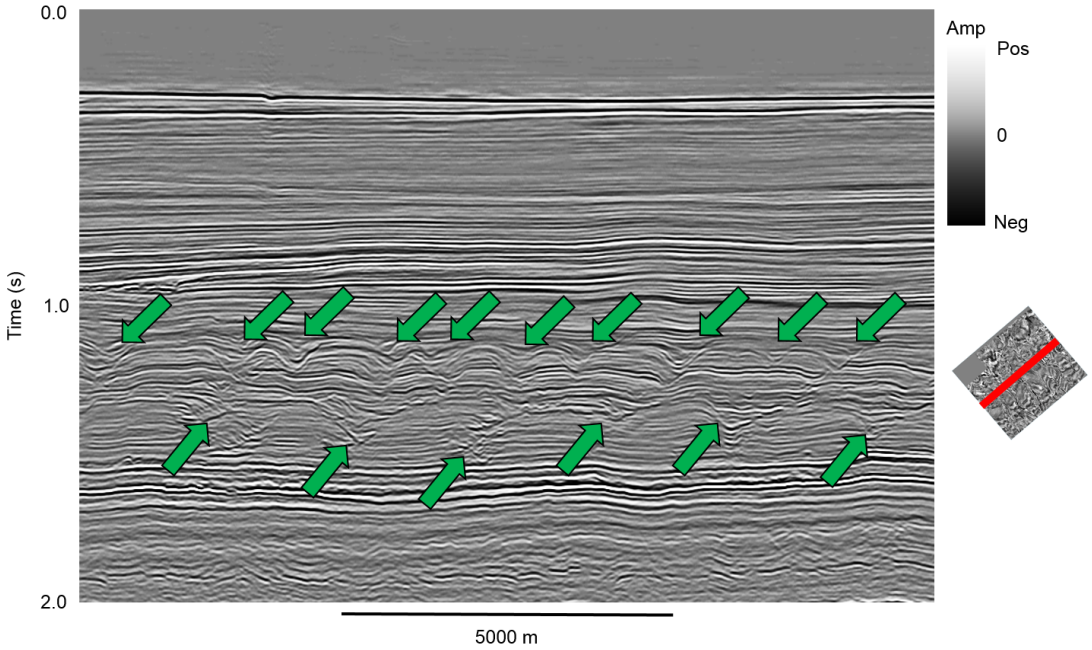


Figure 5.2: A partial interpretation overlayed on the vertical slice. The green arrows denote the channel-forms in the prograding carbonates.

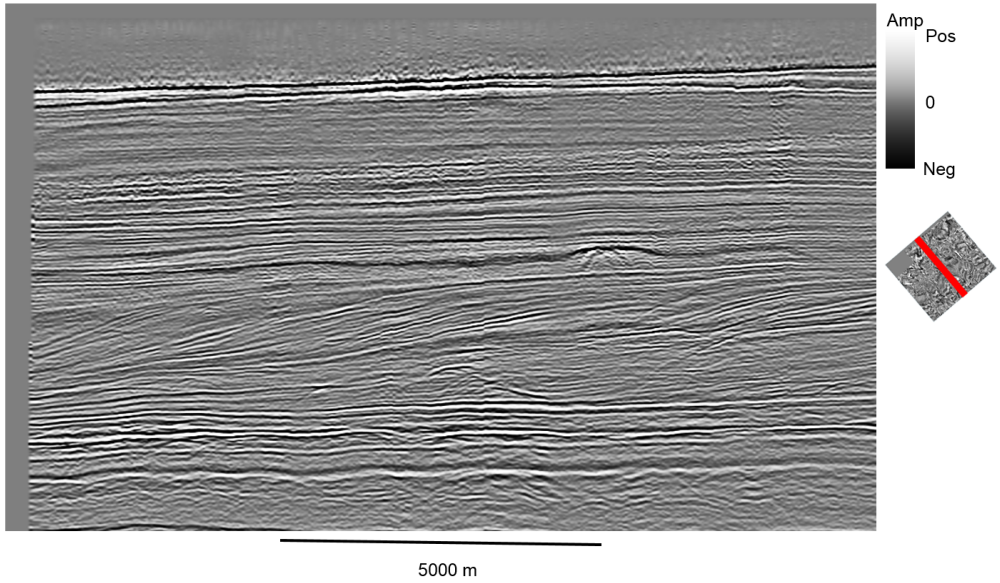


Figure 5.3: A vertical slice through the seismic data volume taken perpendicular to the paleo-shoreface. An experienced interpreter can glean considerable information regarding global eustatic sea levels from this view, but it does not clearly map the channel forms and other architectural elements of the turbidite system.

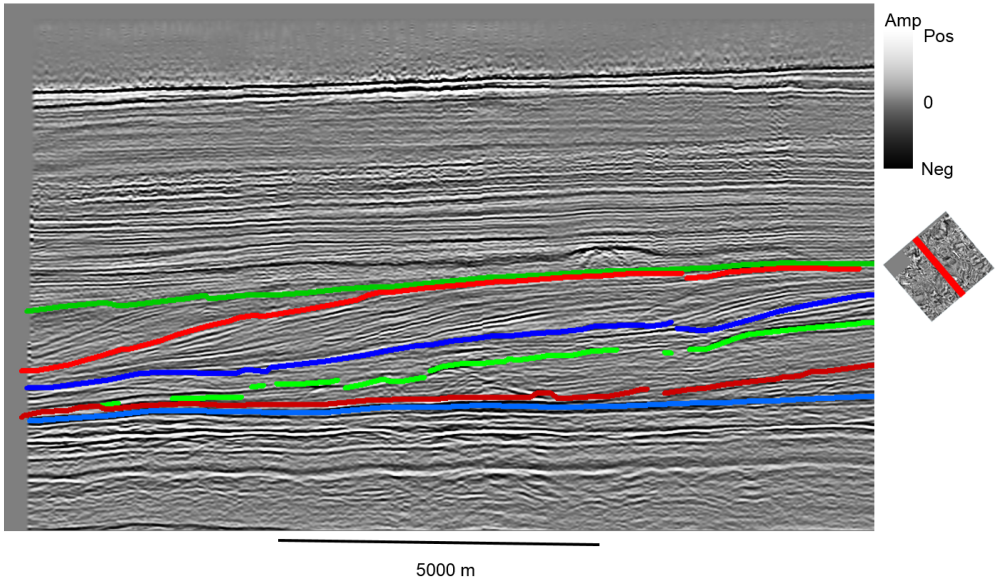


Figure 5.4: A vertical slice through the seismic data volume taken perpendicular to the paleo-shoreface with an interpretation overlain. Blues indicate the tops of high-stand events. Greens indication the tops of transgressive events. Reds indicate the tops of low-stand events.

5.2 Geological and geophysical background

5.2.1 Regional geology

The study area is located on the Rankin Platform of the Carnarvon Basin off the coast of Western Australia (Figure 5.5). A major lowstand event occurred during Early Oligocene time. This resulted in a progradational wedge of carbonate slope that resulted in the Mandu Formation. This progradation continued until it was terminated by an eustatic sea level rise approximately 15 MYA.

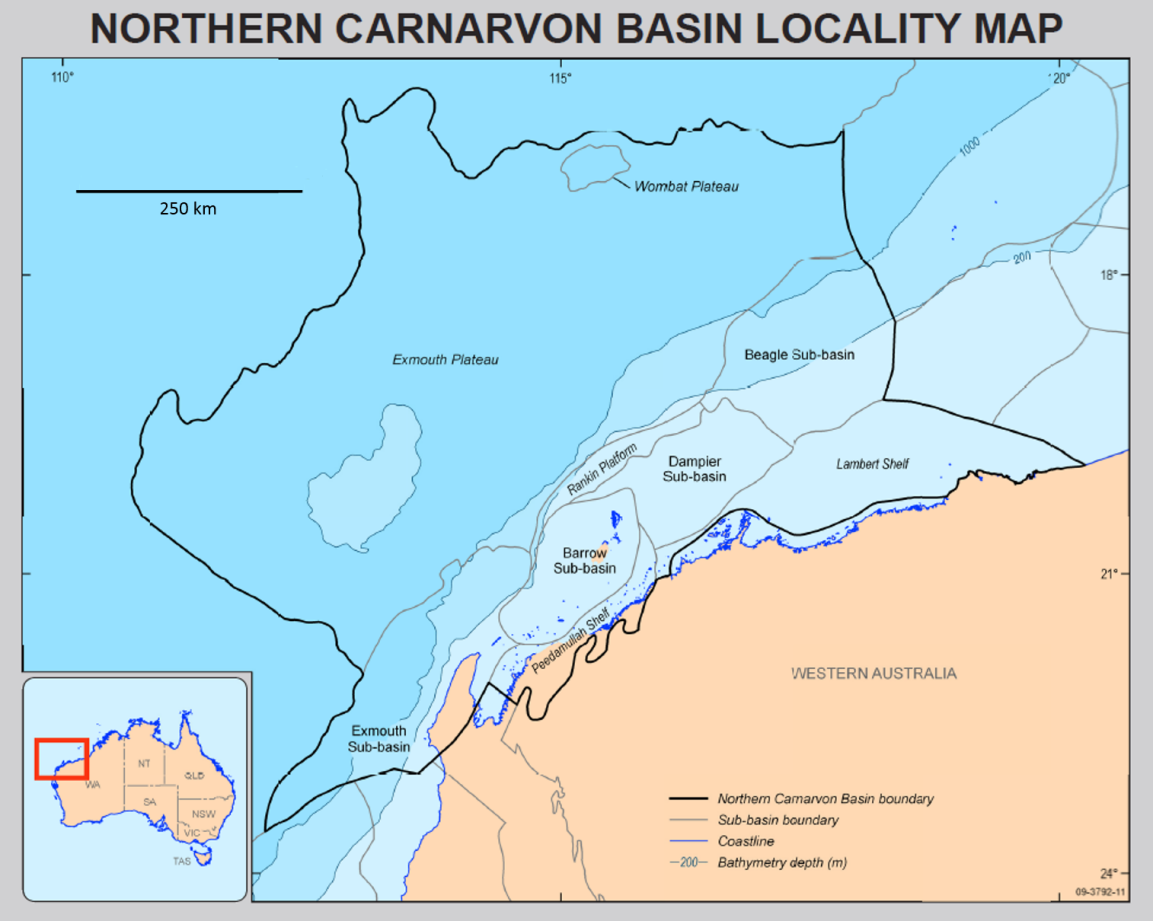


Figure 5.5: Location of the Carnarvon Basin along the coast and offshore of Western Australia. ©Commonwealth of Australia (Geoscience Australia). Used with permission.

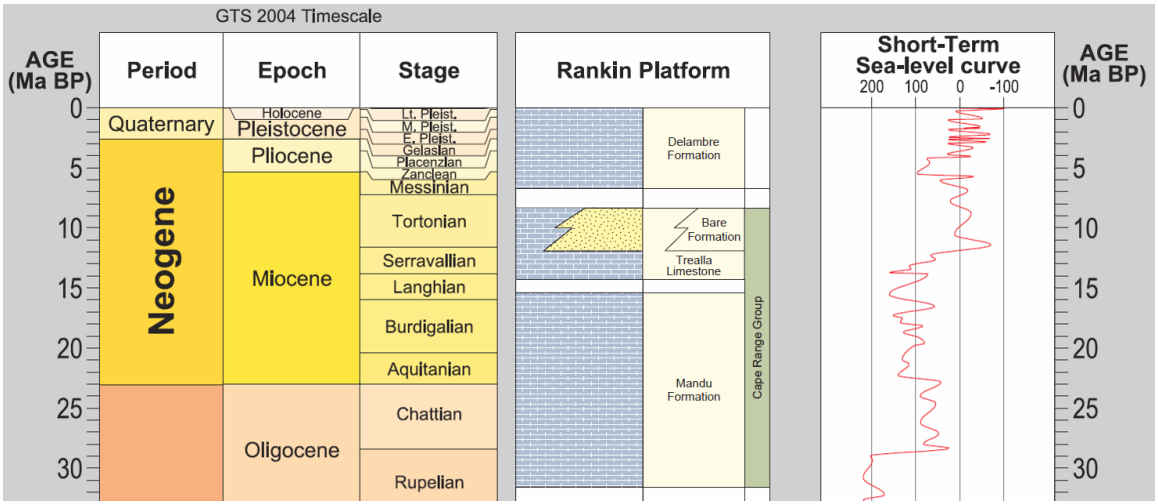


Figure 5.6: Relative sea level curve for the Rankin Platform from the Oligocene to the present. (Richardson, 2000)

During the period of deposition from the Oligocene to the middle Miocene, there were a number of high-stand, low-stand, and transgressive intervals though the overall pattern was a lower frequency sea level rise (Figure 5.6). During the Oligocene to the middle Miocene, there developed a series of channel-forms or canyons. There is some uncertainty as to the mechanism by which these form. It is believed that during low-stand events, clastic systems tend to shed the majority of their material into the basin (Vail et al., 1977) (Figure 5.7). However, it is unknown if this is the case in carbonate environments, and this topic has been the subject of considerable controversy (Bernet et al., 2000). Therefore, improved mapping of these canyons might add to the understanding of the nature of carbonates in general.

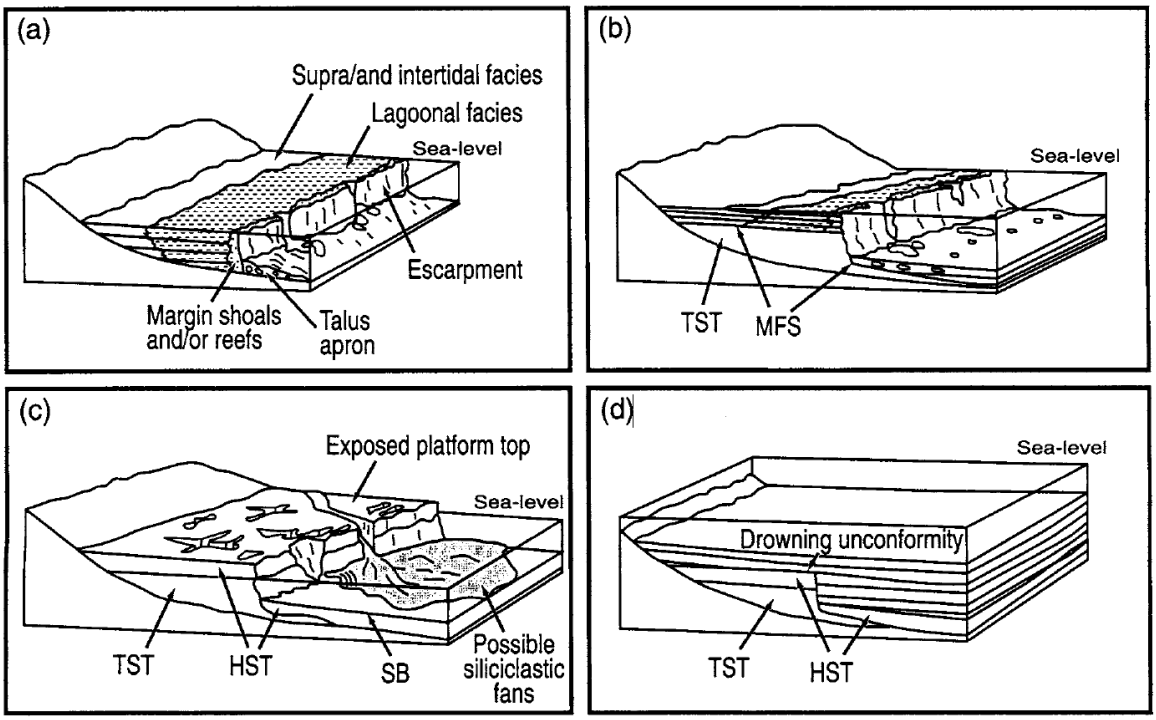


Figure 5.7: Bypass margins are believed to form turbidity flows during low-stand events. a) Transgressive-stand event. b) High-stand event. c) Low-stand event. d) Drowning unconformity. From Moore (2001).

There exist a number of modern analogs for the Mandu Formation. One such analog is the Little Bahama Bank (Mullins et al., 1984). In this case, foreslope reefs in this zone exhibit a channel-form architecture that is present in my study area

(Figure 5.8).

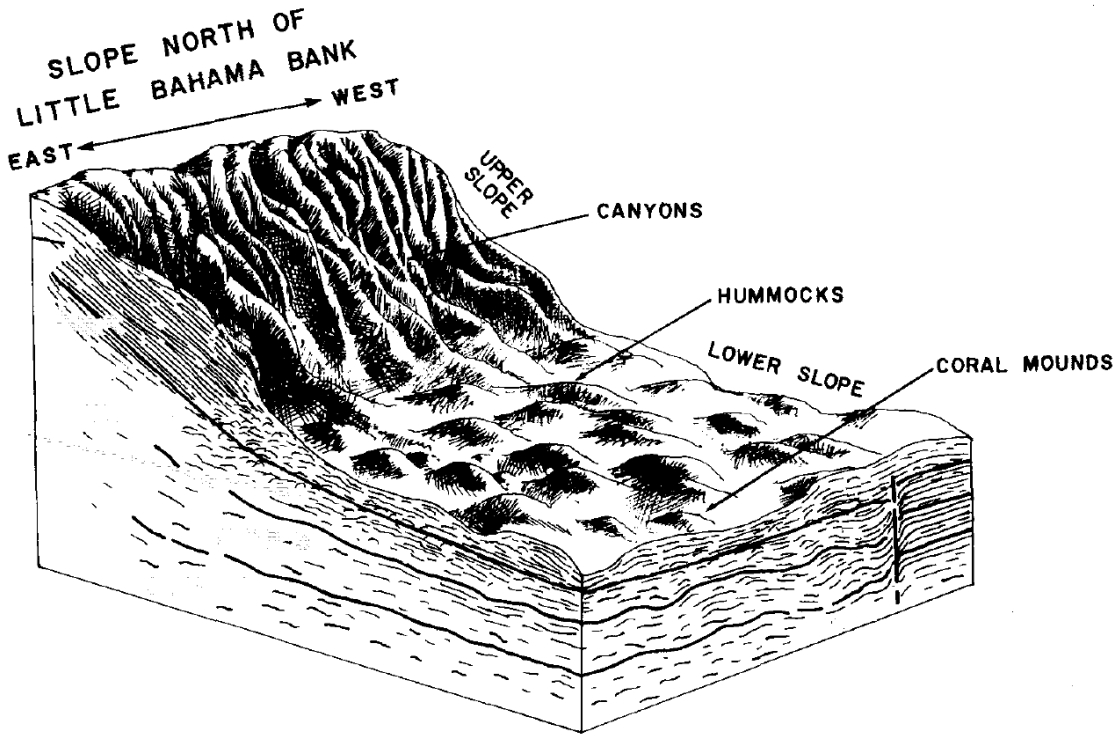


Figure 5.8: One modern analog for the Mandu Formation can be found on the Little Bahama Bank. Foreslope reefs in this zone exhibit a similar channel-form architecture. No scale is implied in this image. Modified from Mullins et al. (1984).

Another modern analog can be found in the Florida Keys, Florida USA. This system is a carbonate structure that is currently experiencing sub-aerial exposure. Viewing this structure in aerial imagery (Figure 5.9) demonstrates channel-forms that are very similar in their size and geometry to those presented in my data set.

5.2.2 Data description

The Rosie 3D survey used in this study was provided by Geoscience Australia. It was acquired between November 1996 and February 1997 by Geco-Prakla, with a line orientation of NE-SW (49.5 deg) with a dual source / 4 streamer configuration. The cable separation was 150 meters and the source separation was 75 m, resulting in

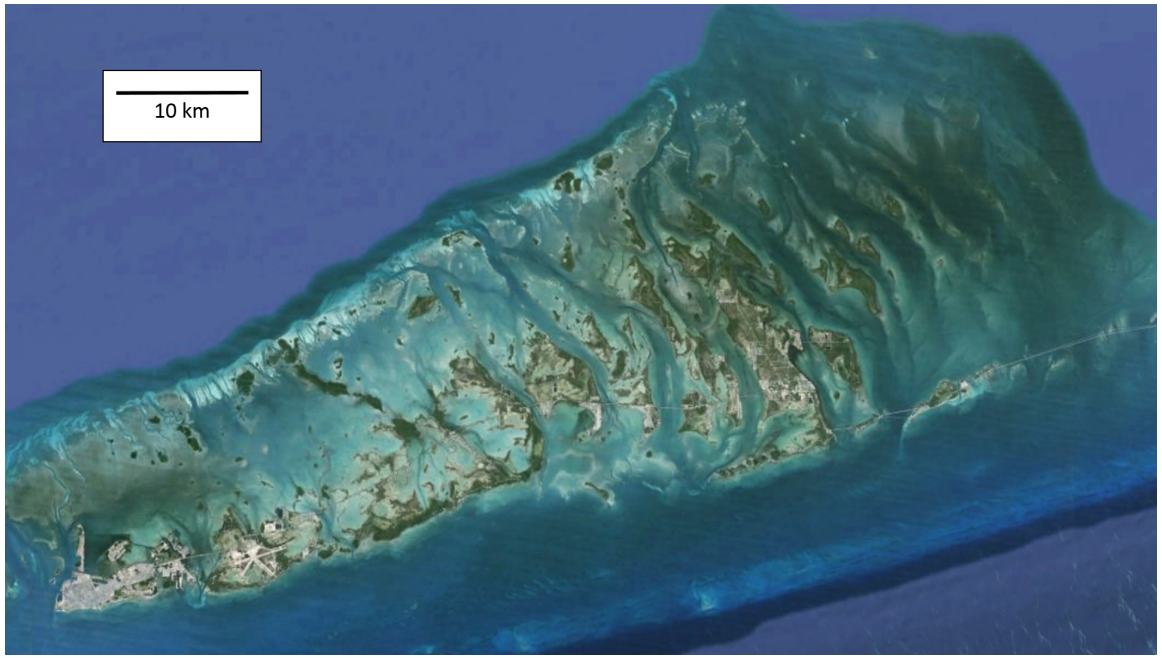


Figure 5.9: A modern analog for the Mandu Formation that is currently experiencing sub-aerial exposure is the Florida Keys, Florida USA. Similar channel-form architecture is readily visible in aerial images. (Courtesy of Google Earth ™.)

an initial subsurface CDP line spacing of 18.75 m. Each streamer had 304 channels resulting in a nominal fold of 50.

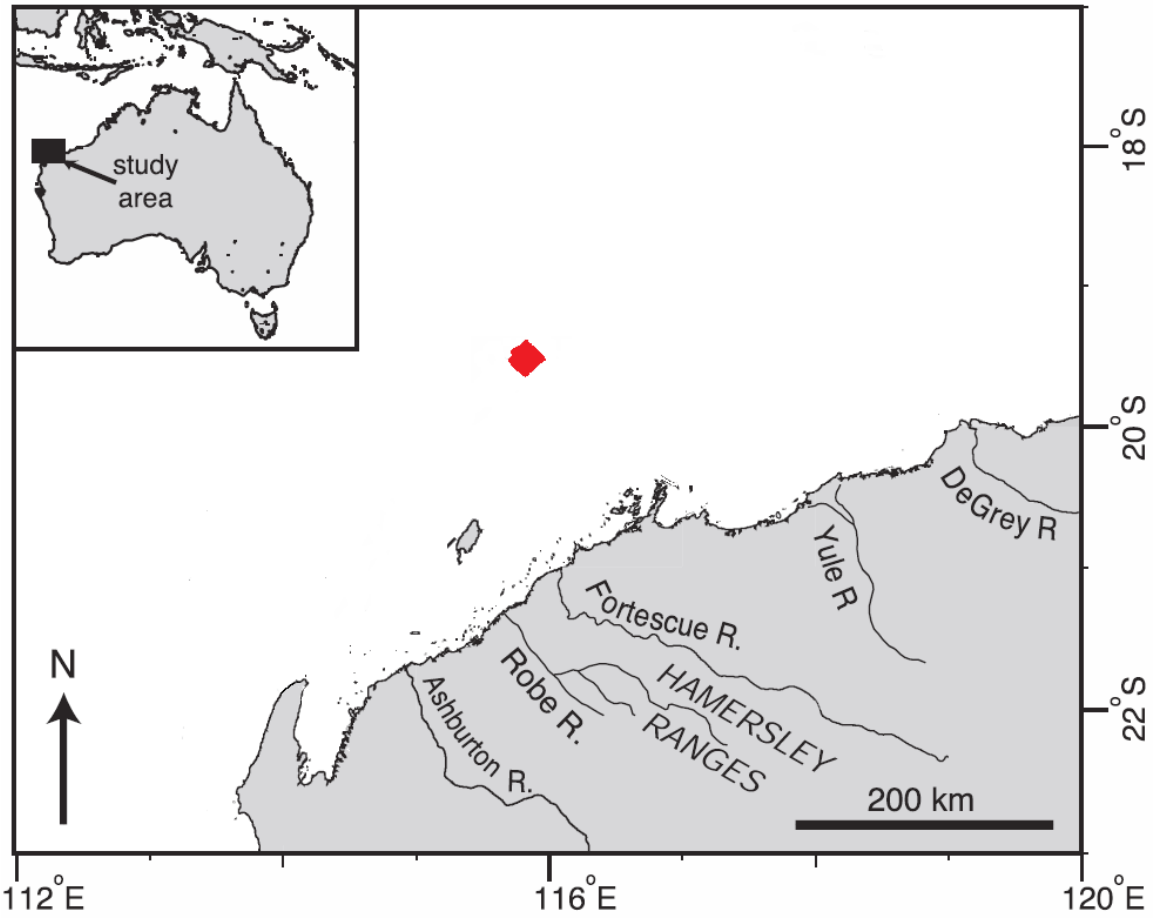


Figure 5.10: The location of the Rosie 3D survey that is used in this study. Modified from Cathro et al. (2003).

Processing was completed by Western Geophysical from December 1996 through July 1997 with a resulting sample increment of 4 ms. The data are of good quality and broad bandwidth for the time of acquisition and processing. Dominant frequency between two and three seconds is 35 Hz. More details about the acquisition and processing of this data set can be found in Richardson (2000).

5.3 Seismic interpretation and 3D geomodeling

Historically, interpretation has reflects the 2D origins of seismic analysis with interpreters using vertical slices through seismic data to interpret geological features such as faults and horizons. By interpreting these features on successive slices, an interpreter is thus able to construct 3D interpretations using an adapted 2D approach.

Geological modeling or geomodeling is the science of using geological and geophysical data to construct computerized models of the subsurface. Typically, this is thought of as being done in 3D. While successive 2D interpretations can construct 3D models of some geological features, it is more efficient to use a direct 3D approach.

5.4 Seismic expression of channel-forms

In order to establish a background for 3D geomodeling of the channel-forms, I examined the expression of channel-forms in my available data set using a number of seismic attributes. The focus was upon visualizing these channel-forms using seismic geomorphological methods combined with seismic attributes. Recently, there has been a trend in published work to focus upon the attribute expression of specific geological features. These works examine a suite of attributes, and show examples of how these features are illuminated with various attributes. The goal of this work is to illustrate how specific attributes are tied geologically and geophysically to the feature of interest.

This approach is in contrast to an all too common approach to seismic attributes of calculating a large number of attributes with little regard for their underlying geological or geophysical tie to the interpretation task at hand. Commercial packages

typically have 50+ attributes, many of which are poorly understood by interpreters. The problem is compounded when the interpreter then relies upon partially understood data analysis techniques such as such as neural networks or latent space modeling (Wallet et al., 2009) to automatically process these attributes without careful examination.

In contrast, interpreters who are experienced in the use of seismic attributes typically use a very small number of attributes they understand well, and that they have found useful in the past. However, the ability to do this properly involves understanding and experience as to what attributes work within a given geologic and data quality setting. Furthermore, we are happiest when we can link the response of a chosen attribute to some geological and/or geophysical feature of our data and thus explain our results in a meaningful manner. With this in mind, I will test a number of attributes, focusing upon their expression of channel-forms in the hybrid carbonate turbidite system.

5.4.1 Single attribute analysis

I begin my analysis by examining individual attributes to better understand the seismic attribute expression of the channel-forms. Close examination of Figure 5.1 suggests three distinct sets of channel forms. Approximate locations of these sets of channel forms are designated in Figure 5.11.

Since seismic geomorphology involves using visualization techniques to illuminate features at a given geologic time, a common work-flow is to pick horizon slices and flatten the data rather than work with time slices. However, as seen in Figure 5.2, more than half the lateral extent of the Mandu Formation is channel-forms. In this environment, picking a consistent surface for flattening proved impossible. Best prac-

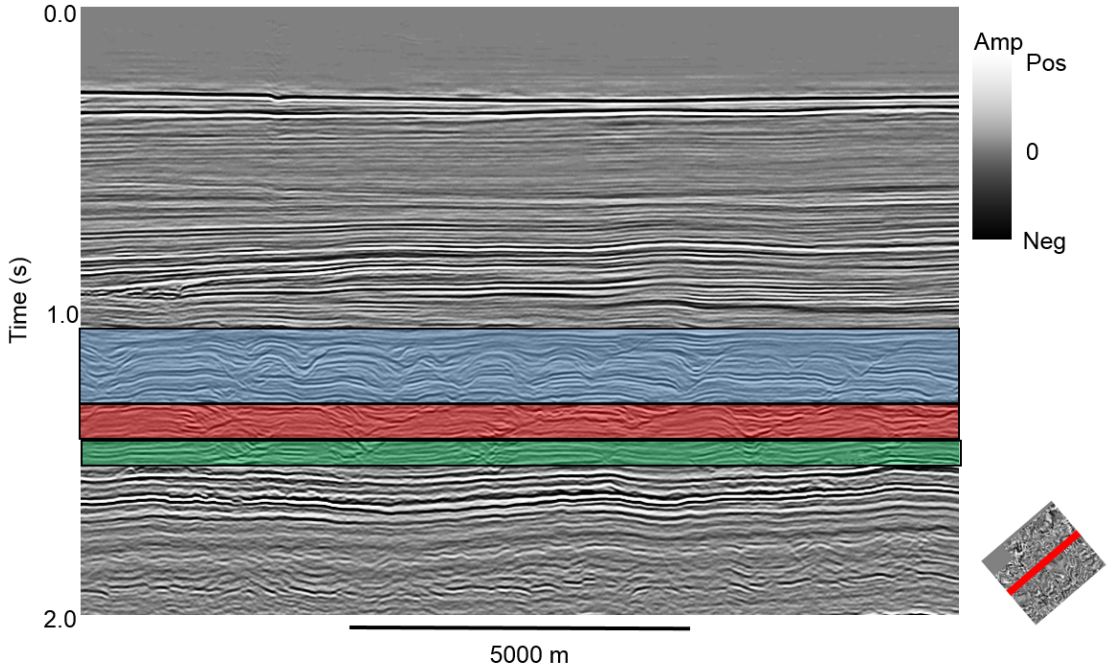


Figure 5.11: Three distinct sets of channel forms are apparent in the data set. Approximate locations of these sets are designated by the blue lines.

tice in this case typically involves picking a strong continuous reflector above or below the channelized region and generating phantom horizon slices (Brown, 2011). Figure 5.12 shows a horizon I interpreted for this purpose.

Figure 5.13 shows the results of flattening using the horizon shown in Figure 5.12. The appears to have flattened the data well in the lowest portion of the Mandu Formation. However, given the strong progradational nature of the formation the flattening horizon has little bearing upon the internal geometry of the Mandu Formation. Hence, further up in the system, the flattening has little result, and horizon slices will tend to cut across geological ages which should be recognized as a limitation of this flattening work-flow.

Figure 5.14 shows a zoomed view of the vertical slice of amplitude data centered about a representative channel-form. A number of details concerning the channel-form suggest attributes that may be useful. Specifically, the shown channel-form is associated with discontinuities, converging reflectors, and an overall concave shape.

Figure 5.15 shows a horizon slice taken 52 ms above the flattening surface. A number of meandering channel-forms are visible in this horizon that appear to have been deposited upon a relatively flat topography. My interpretation is that these systems formed in a depositional environment before the carbonate reef prograded into the region of this data set.

Figures 5.16 and 5.17 show horizon slices taken 152 and 352 ms above the flattening horizon respectively. The channel-forms in these horizons cut sharply through the carbonate, and they appear to result from erosion rather than deposition.

The variance attribute detects boundaries and edges by calculating the second central moment (statistical variance) for a windowed region in a seismic data set (Marfurt et al., 1998). In the presence of a boundary, the window contains obser-

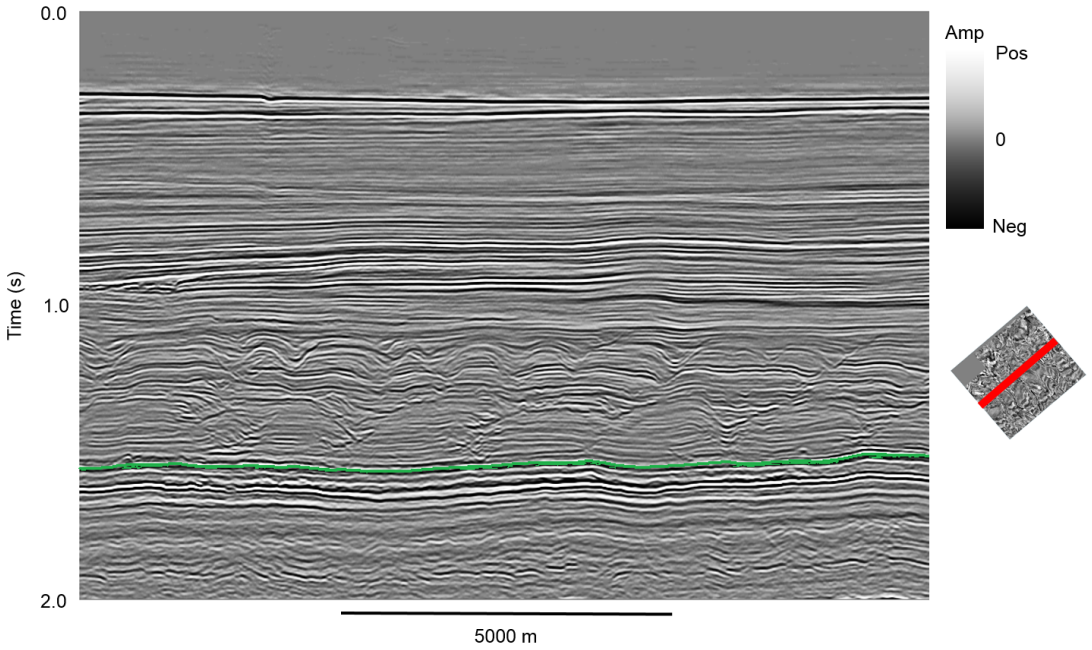


Figure 5.12: The green line shows the horizon I interpreted to flatten the data volume for this study.

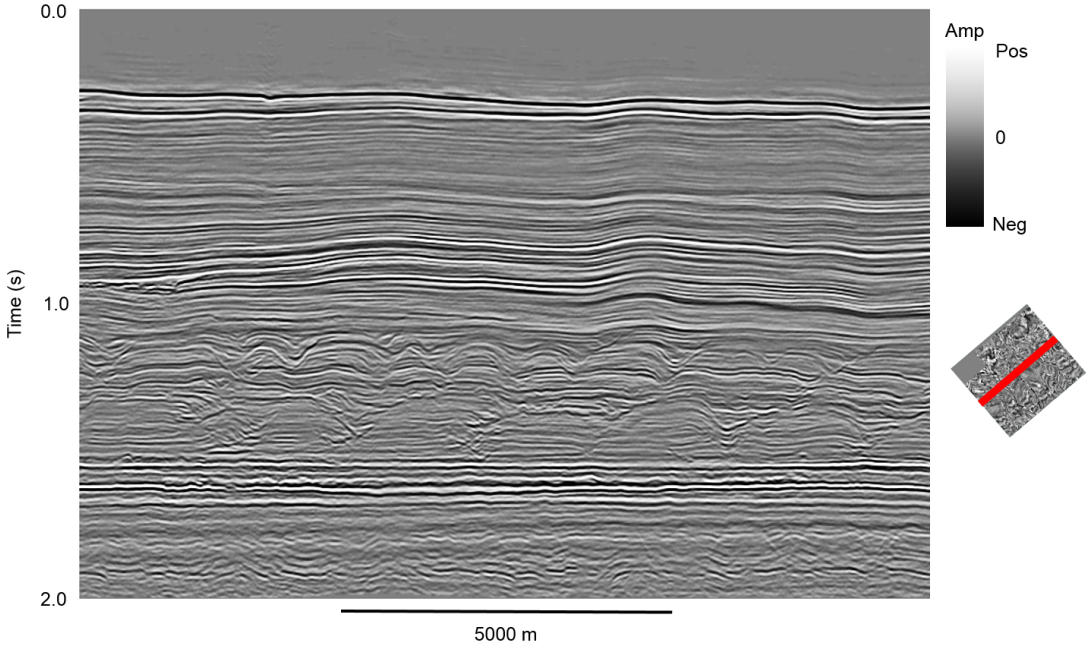


Figure 5.13: This is the flattened version of the data that was used in this study.

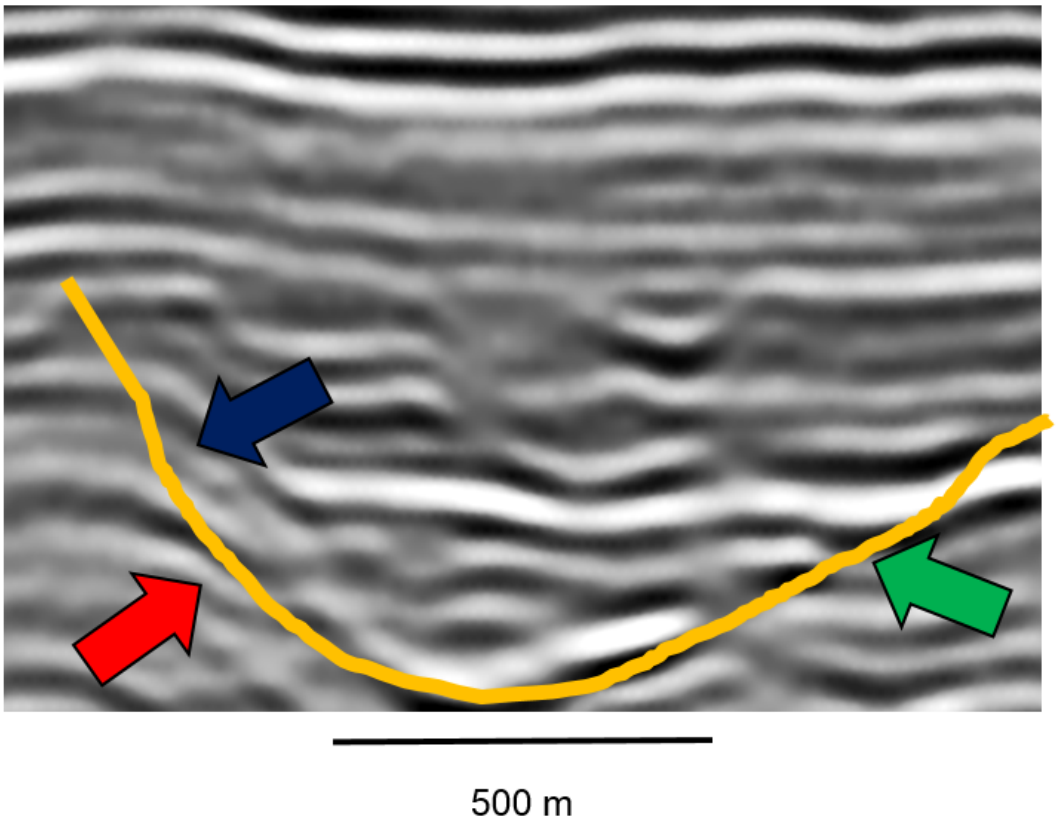


Figure 5.14: Zooming in on a channel-form yields considerable information about the morphology of the features. Reflectors associated with the channel-forms tend to converge out toward the edges inside the channel-form (blue arrow) and in toward the edges outside the channel-form (red arrow). Also, there are considerable numbers of discontinuities associated with the channel-forms (green arrow). The overall shape of the channel-forms is concave as shown by the yellow line.

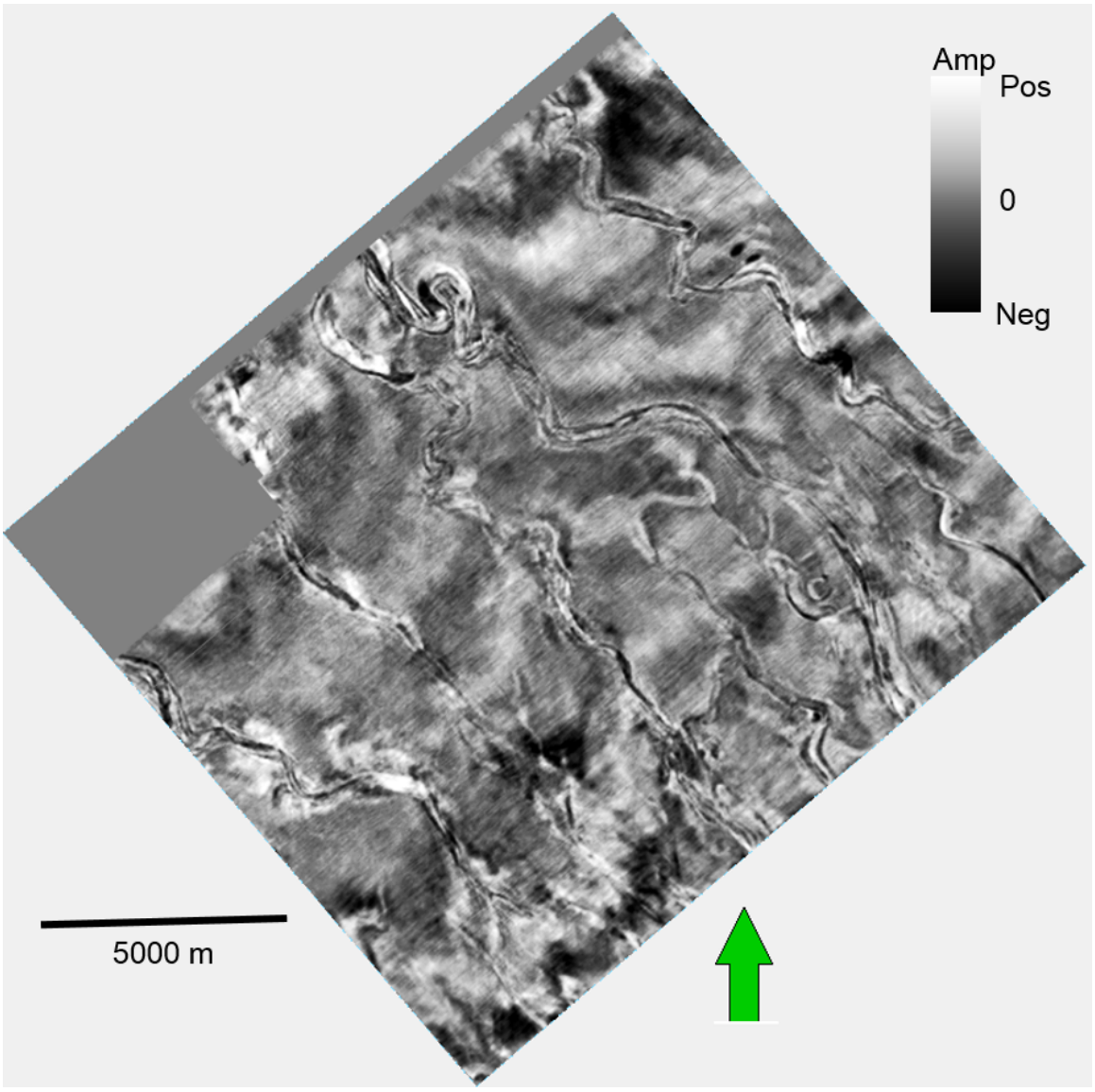


Figure 5.15: Phantom horizon slice through the seismic amplitude volume 52 ms above the flattening (green) horizon. The channel-forms are meandering in this horizon. I interpret this as being before the carbonate reef prograded into the region.

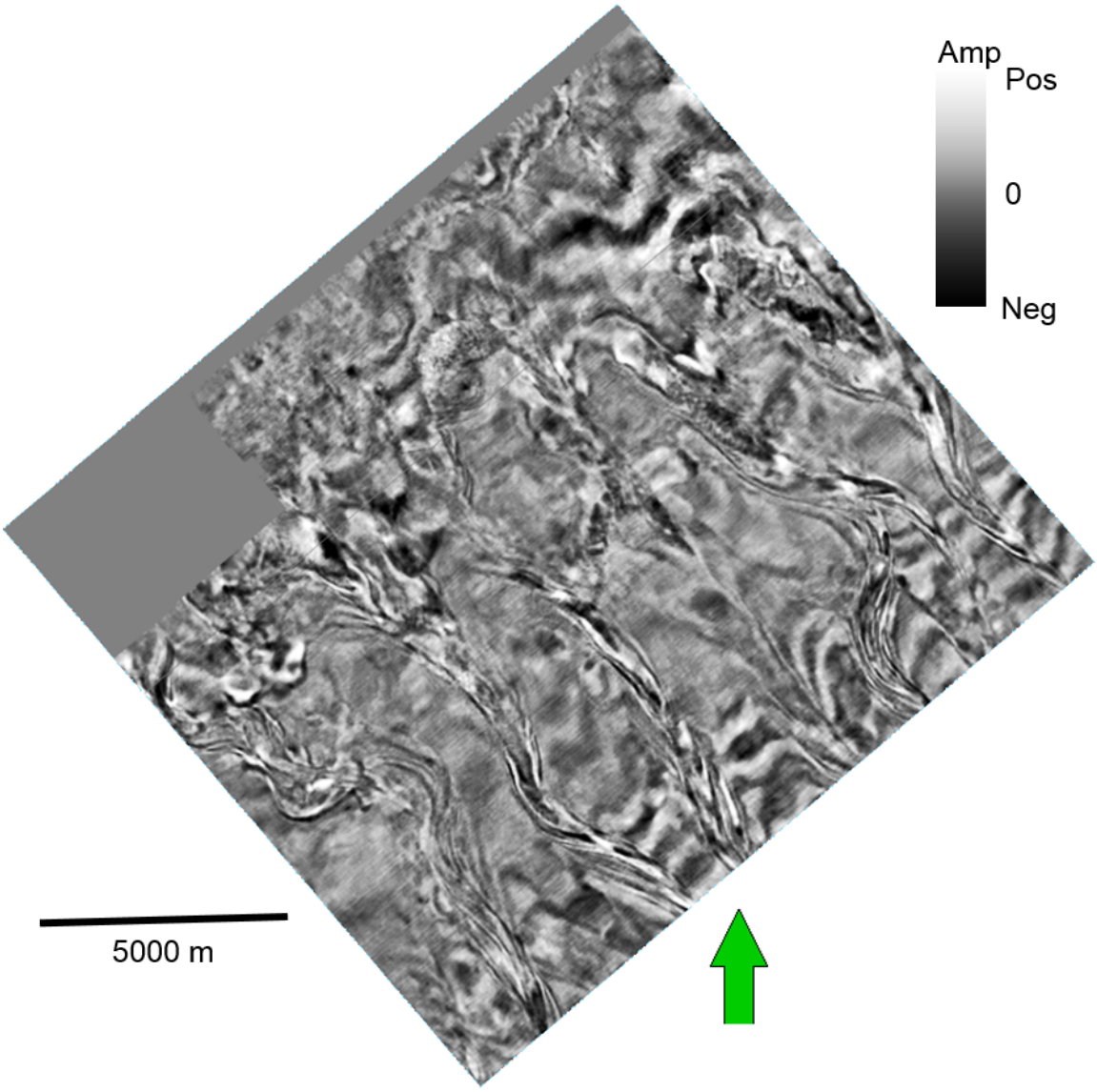


Figure 5.16: Phantom horizon slice through the seismic amplitude volume 152 ms above the flattening (green) horizon. The channel-forms are straighter and wider than they were at the shallower horizon corresponding to their deeper incisement.

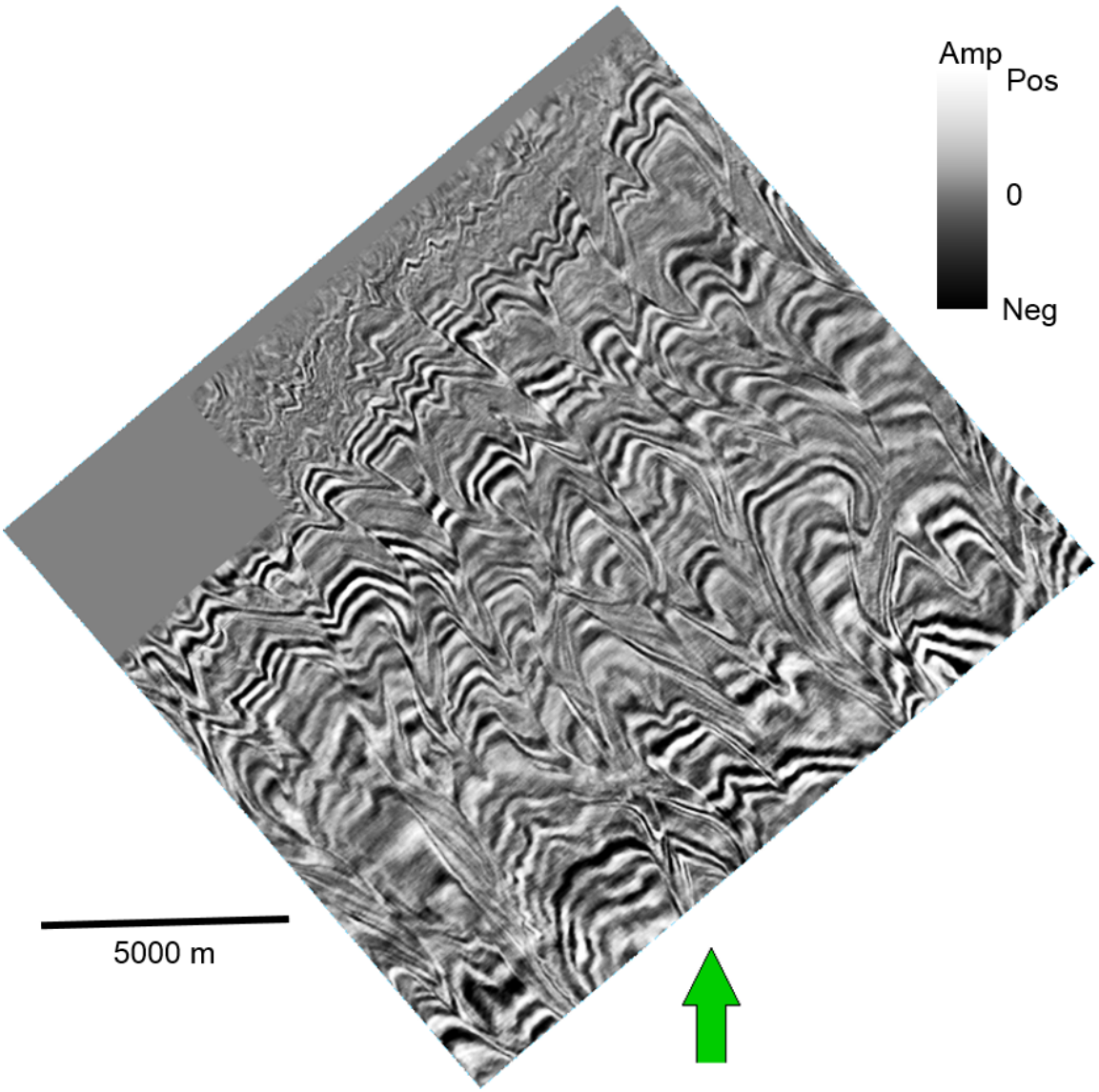


Figure 5.17: Phantom horizon slice through the seismic amplitude volume 352 ms above the flattening (green) horizon. The extent and edges channel-forms are more difficult to interpret in this horizon as they are cutting through the internal geometry of the carbonates at a much higher angle.

vations from either side of the boundary, thus resulting in a higher variance value. Variance would thus help in interpreting channel-forms by highlighting their edges. Figure 5.18 shows the variance attribute for a vertical line. In this image, the channel-forms are visible. However, the edges and form of the channel-forms is not clear, and the overall impression is "blurry".

Figure 5.19 shows a zoomed view of the variance attribute co-rendered with the seismic amplitude over a channel-form. While variance detected some of the boundaries, it missed others, and it did not provide for a closed boundary.

Figures 5.20-5.22 show the variance attribute for 52, 152, and 352 ms above the flattening (green) horizon shown in Figure 5.12. Unlike in the vertical slice (Figure 5.18, the edges are clear and crisp. This contrast suggests that while variance may be useful in understanding and interpreting channel-forms, it is not suitable for 3D geomodeling of them as it does not achieve closure (fully defining the boundaries in 3D).

The next attributes I will consider is the principal curvature attribute, most negative principal (k2) curvature (Mai et al., 2008). Since channels are frequently described as "lens shaped" or valley cross-sectional structures in seismic data, it seems reasonable that channel-forms would have a curvature response, and hence principal curvature should be useful in their interpretation.

Highly negative values of k2 would tend to be associated with structural valleys. Generally, this is the expected shape of seismically thick channel-forms. Figure 5.23 shows the k2 curvature co-rendered with seismic amplitude for the vertical slice. In this figure, the highly negative values of k2 (dark blue) are clearly associated with the channel-forms. However, these regions do not appear to span the full width of the channels but rather accentuate the channel-form axes.

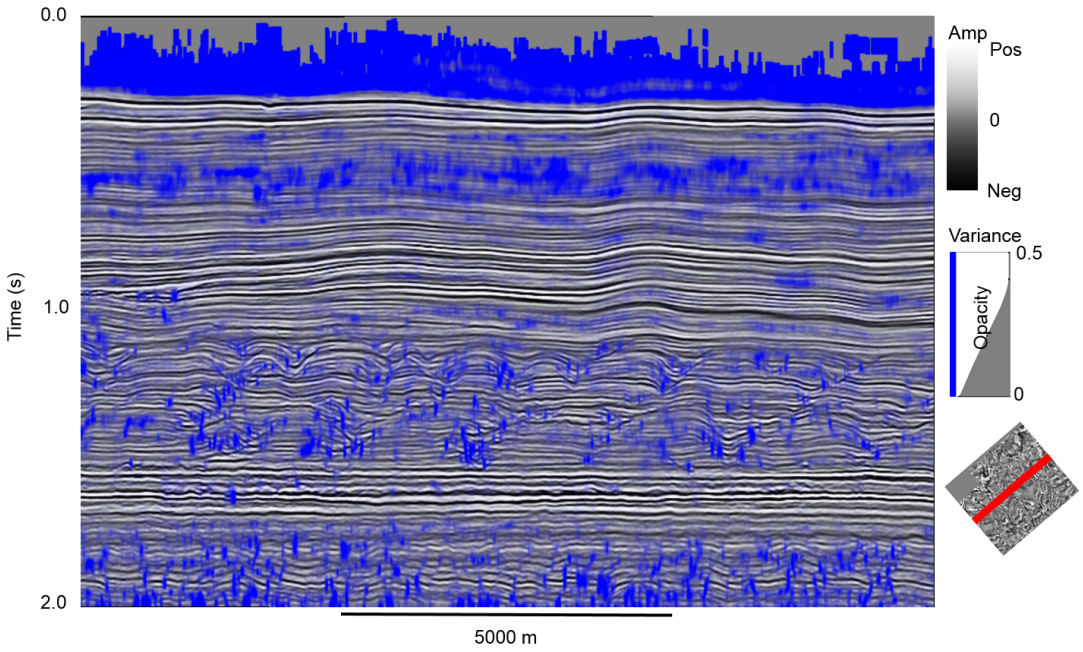


Figure 5.18: The variance attribute for a vertical line. The expression of the channels is readily apparent, but edges are not clear. The image has a generally "blurry" appearance.

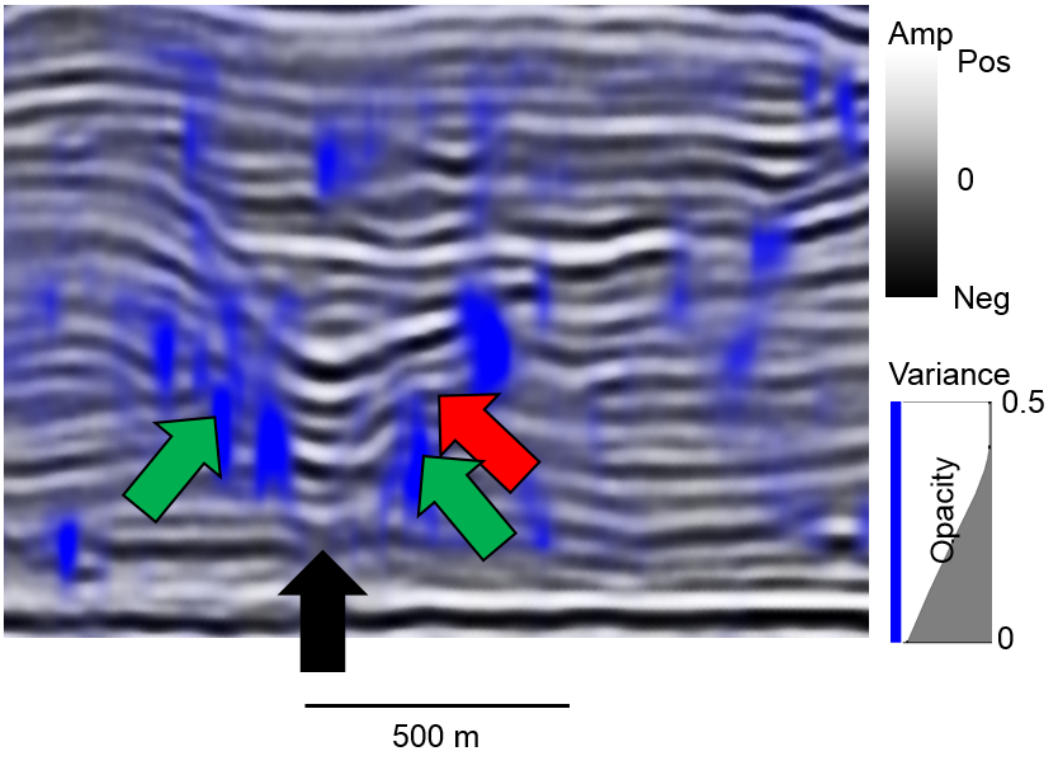


Figure 5.19: The variance attribute zoomed in upon a channel-form. Some boundaries are highlighted (green arrows) while others are not (red arrow). The bottom of the channel-form, however, is not highlighted (black arrow).

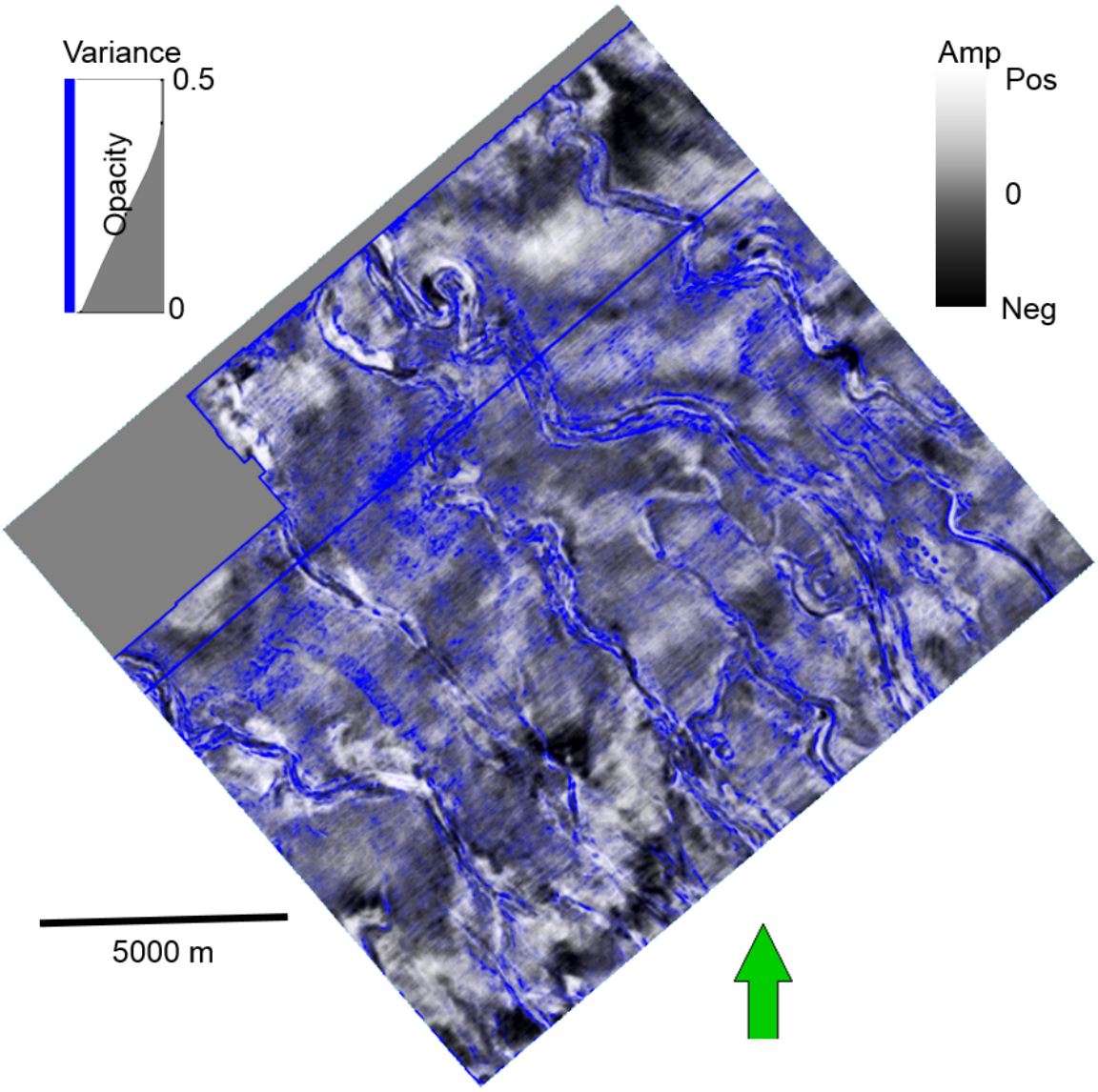


Figure 5.20: Variance attribute for 52 ms above the flattening horizon.

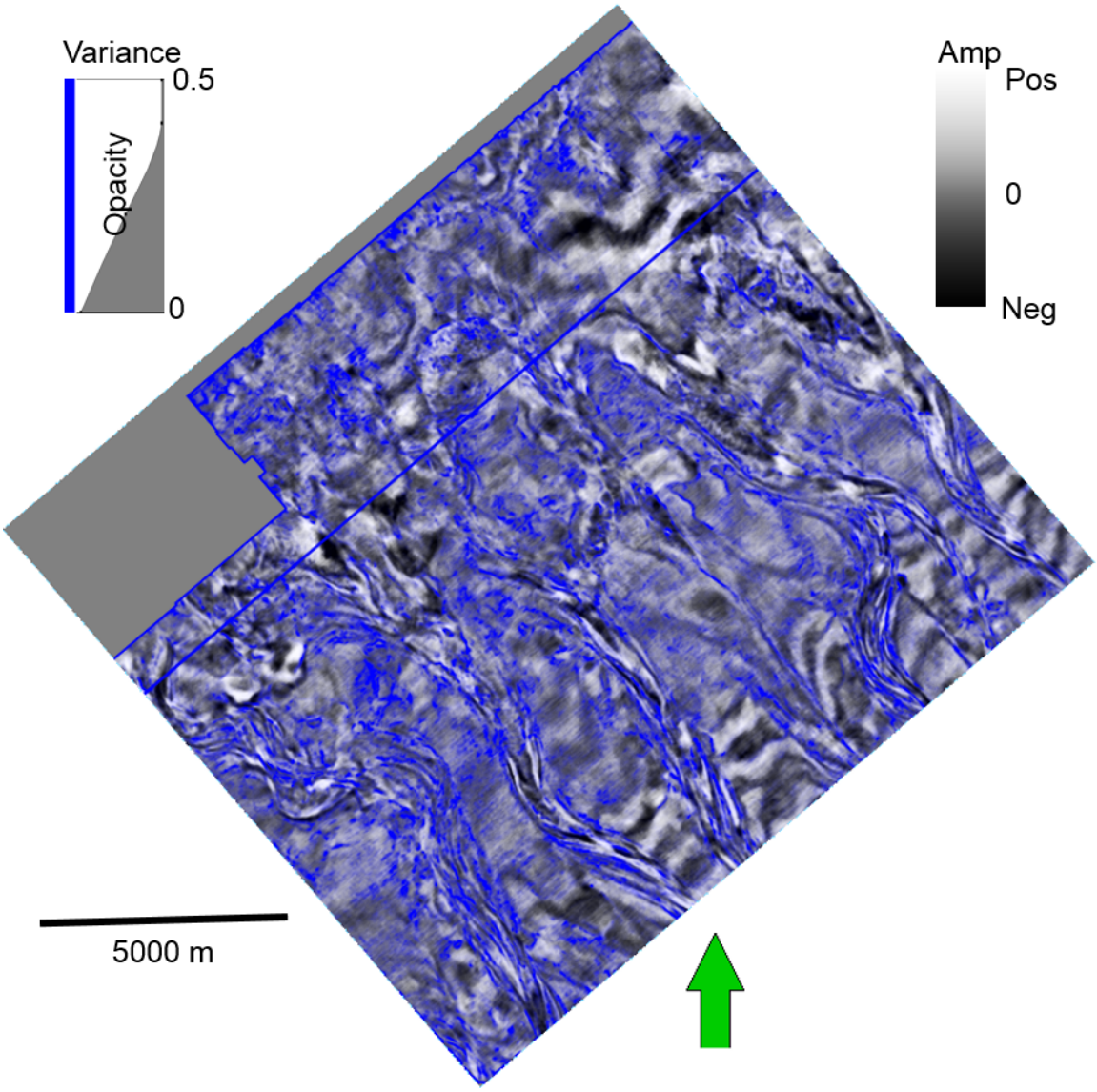


Figure 5.21: Variance for 152 ms above the flattening horizon.

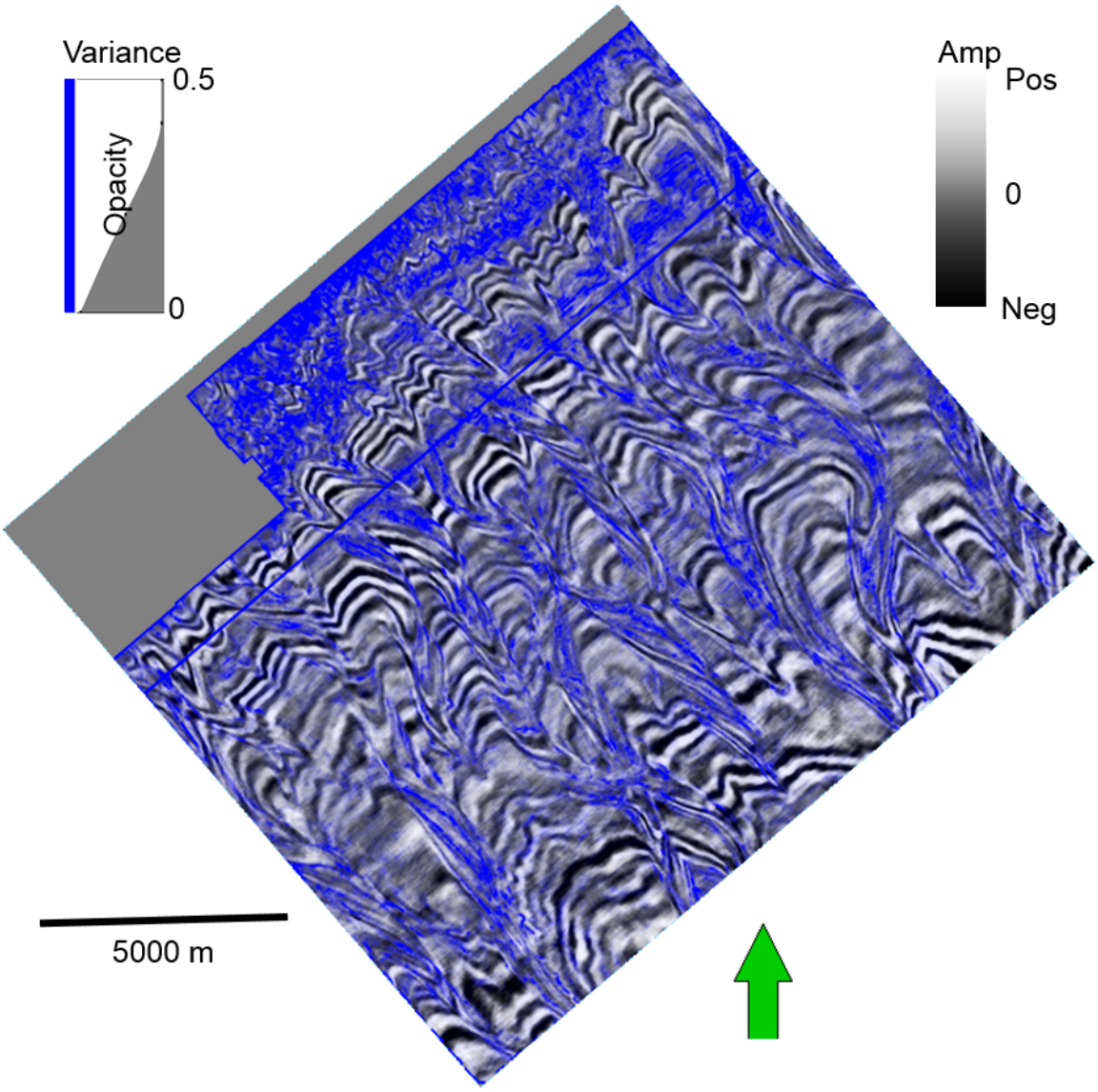


Figure 5.22: Variance attribute for 352 ms above the flattening horizon.

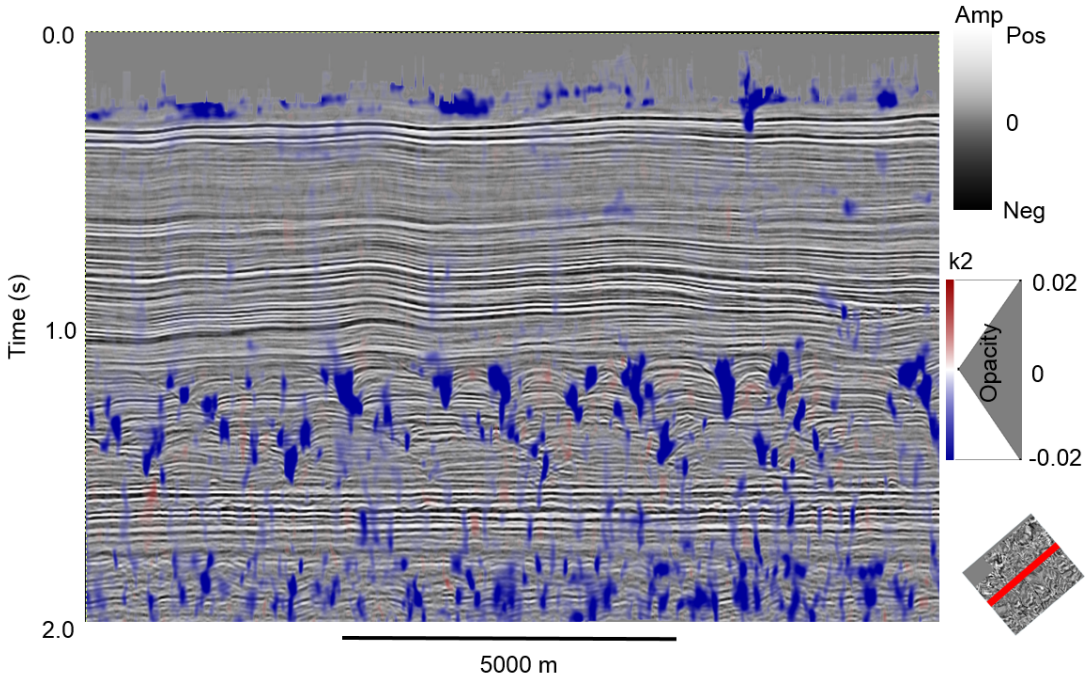


Figure 5.23: K2 principal curvature for a vertical. Highly negative values appear to follow the centers of the channel-forms, but they do not appear to fully cover the lateral crosswise extent.

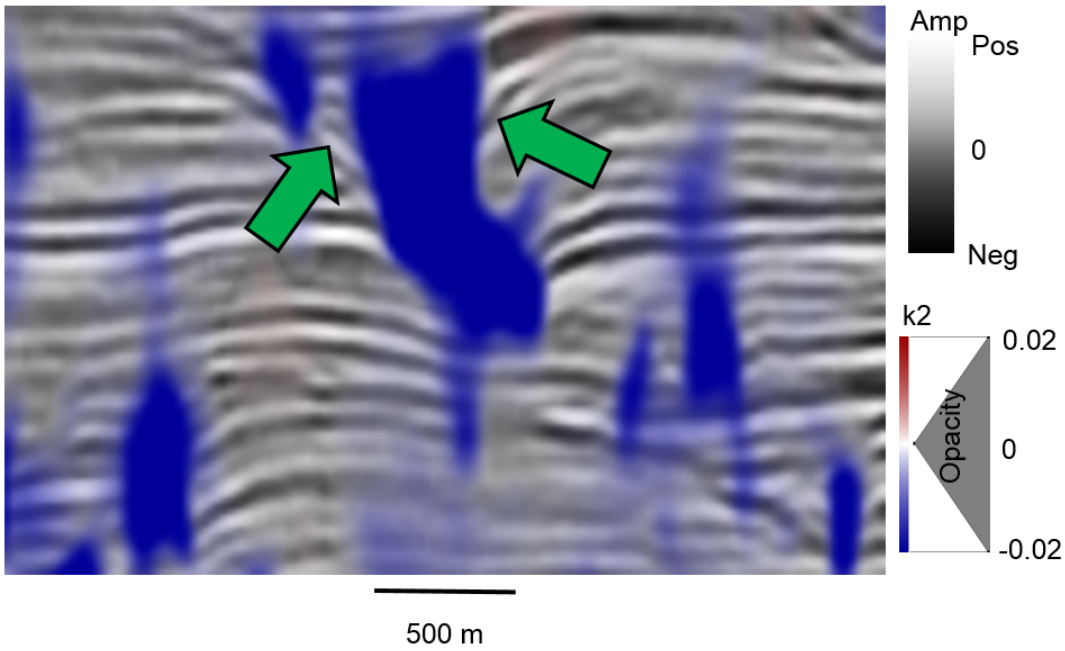


Figure 5.24: Most negative curvature zoomed in upon a channel-form. Highly negative values of k2 characterize the vertical extend of the channel-form, they do not reach the full lateral extent as shown by the green arrows.

Figures 5.25-5.27 show the k2 curvature attribute for 52, 152, and 352 ms above the flattening (green) horizon shown in Figure 5.12. In these figures, the highly negative regions appear to completely map the channels. Furthermore, unlike variance, they appear to correspond to the channel-forms axes rather than the channel-form boundaries. This makes them suitable for geobody extraction methods based upon value thresholding. However, I note that Figure 5.23 suggested that such an approach might not lead to the modeling of the full crosswise extent of the channel-forms.

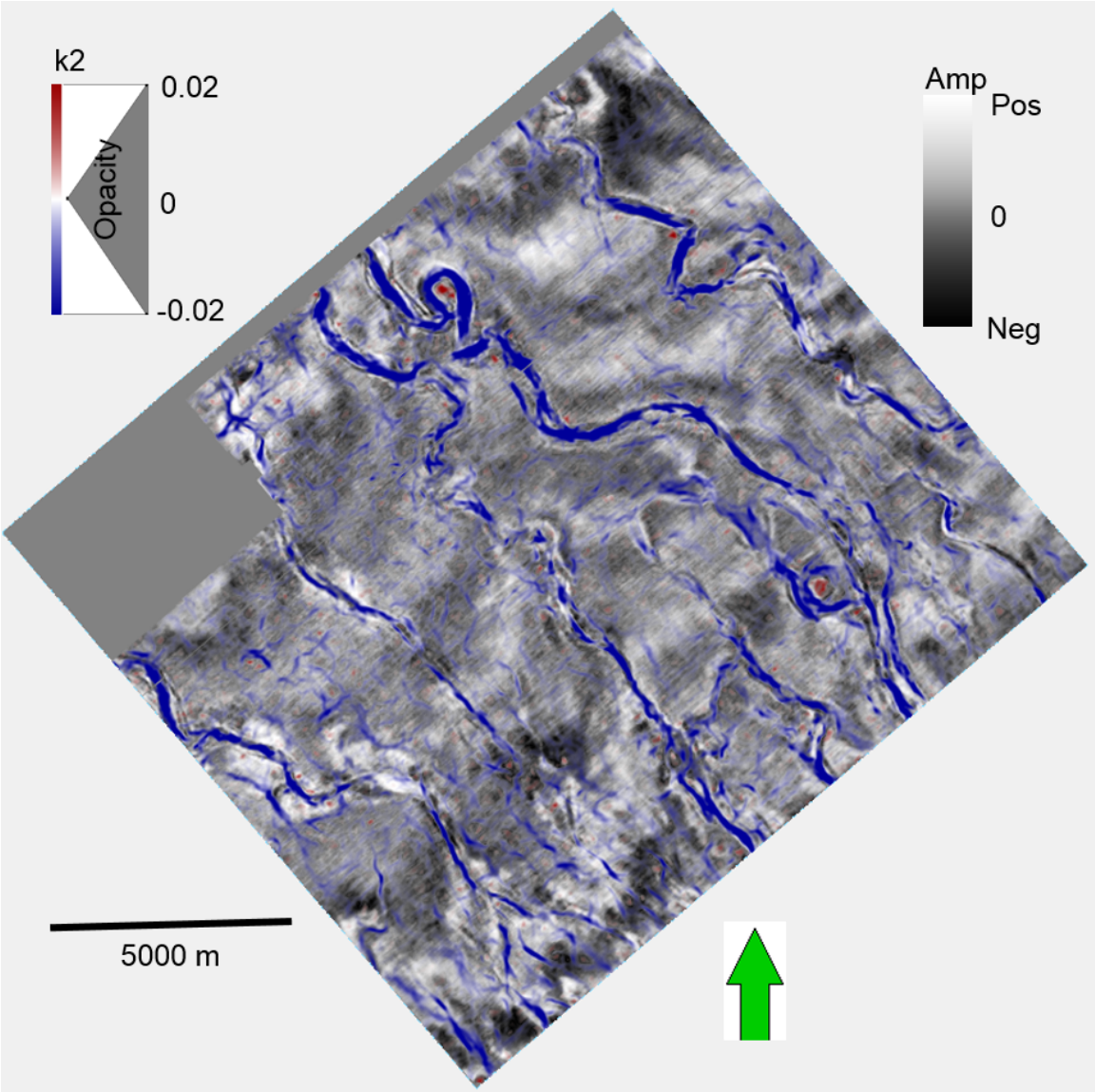


Figure 5.25: K2 principal curvature for 52 ms above the flattening horizon. Highly negative values appear to map out the channel-forms.

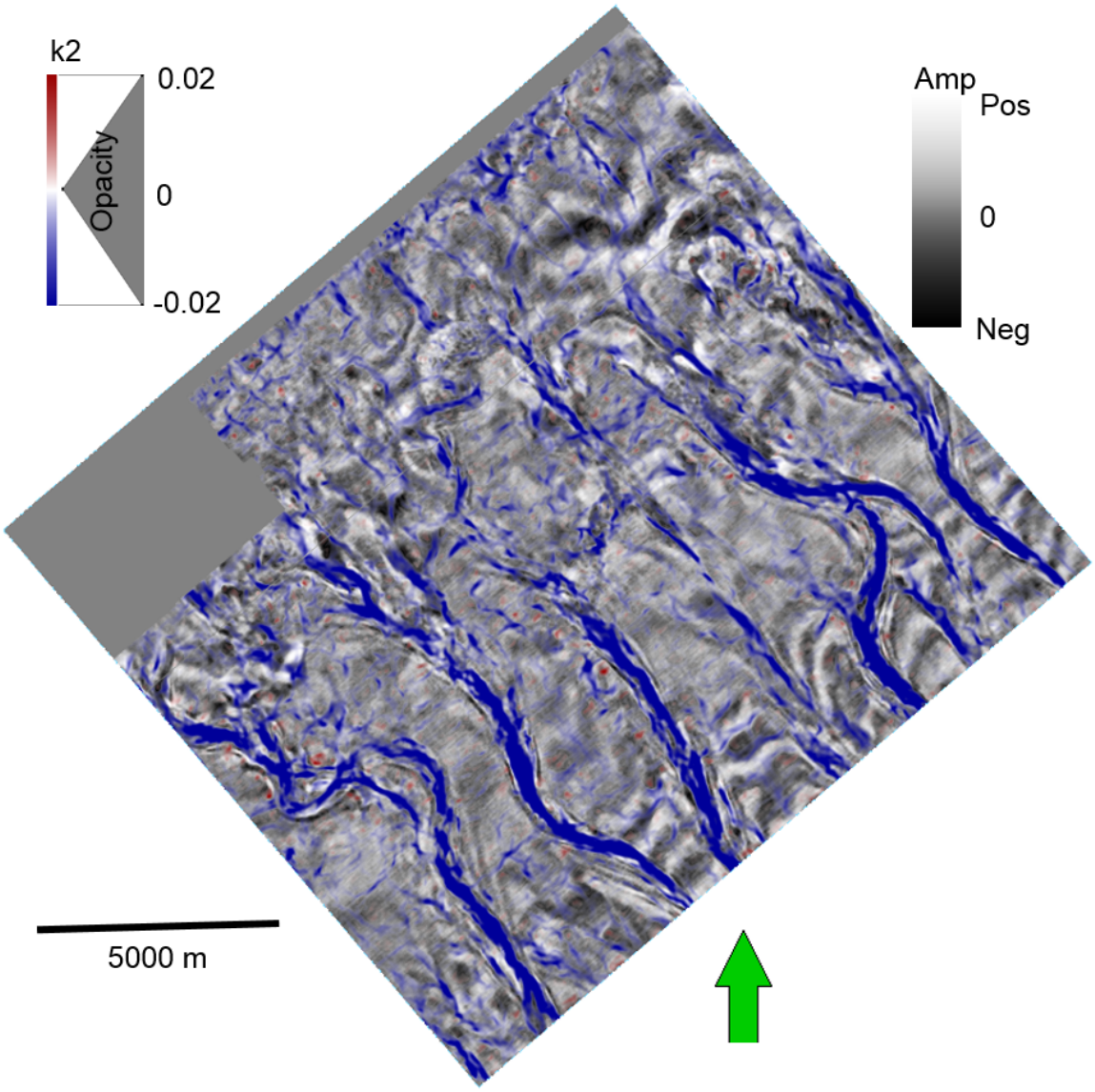


Figure 5.26: K2 principal curvature for 152 ms above the flattening horizon. Highly negative values appear to map out the channel-forms.

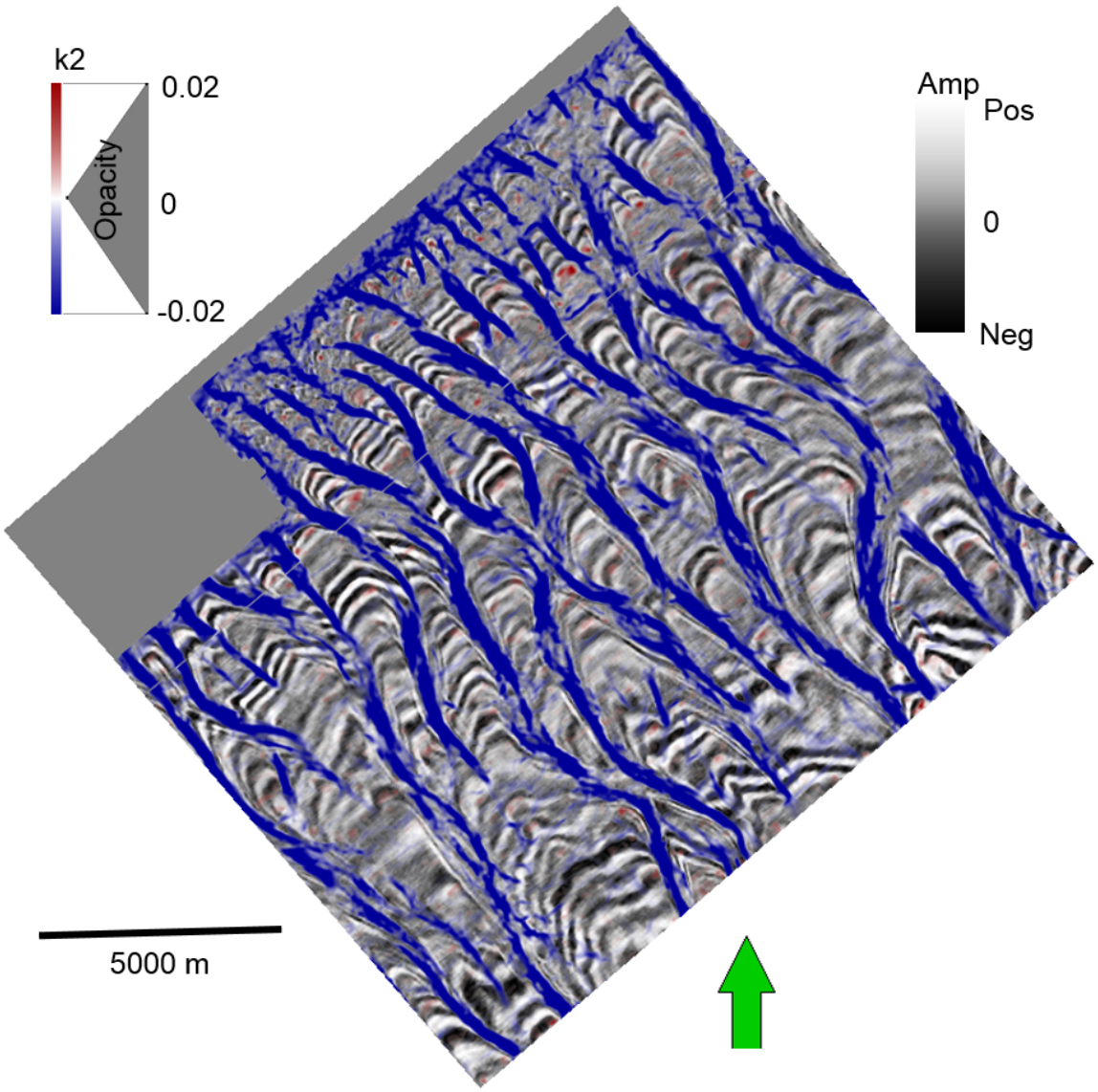


Figure 5.27: K2 principal curvature for 352 ms above the flattening horizon. Highly negative values appear to map out the channel-forms.

Since k2 curvature appeared to map the center of the channel-forms, I turn my attention to what might be used to "fill-in the gaps". Examination of Figure 5.14 leads to the observation that while the middle of the channel-forms have a trough-like appearance, the edges "roll-off" into angular unconformities. Reflector convergence (Marfurt and Rich, 2010) is an attribute sensitive to such unconformities. It works by calculating the magnitude to which reflectors converge together as well as the direction of any such convergence.

Figure 5.28 shows the reflector convergence azimuth and magnitude for the vertical line. The sides of the channel-forms appear visible as adjoining regions of values separated by 180 degrees. In general, the values of these regions are mostly in east/west sets perpendicular to the channel-form axes. Contrasting values appear on the flanks of the channel-forms. These values on the flanks are caused by the erosional nature of the channel-forms cross cutting layers.

Figure 5.29 shows a zoomed portion of the vertical line. Contrasting azimuths are seen on the edges of the channel-forms as well as the flanks. Figure 5.30 shows how such a configuration will tend to occur in an incised channel-form architecture.

5.5 Geobody extraction

Given these observations on the response of the k2 curvature attribute to the channel-forms, I can now use a thresholding approach to modeling and extracting the channel-forms in 3D (Myer et al., 2001). Geobody extraction is a process by which attribute values in one or more 3D volumes are used to create objects in 3D. These objects could correspond to salt diapers, channels, or other geologically meaningful features. Figure 5.31 summarizes typical work-flow used for geobody extraction.

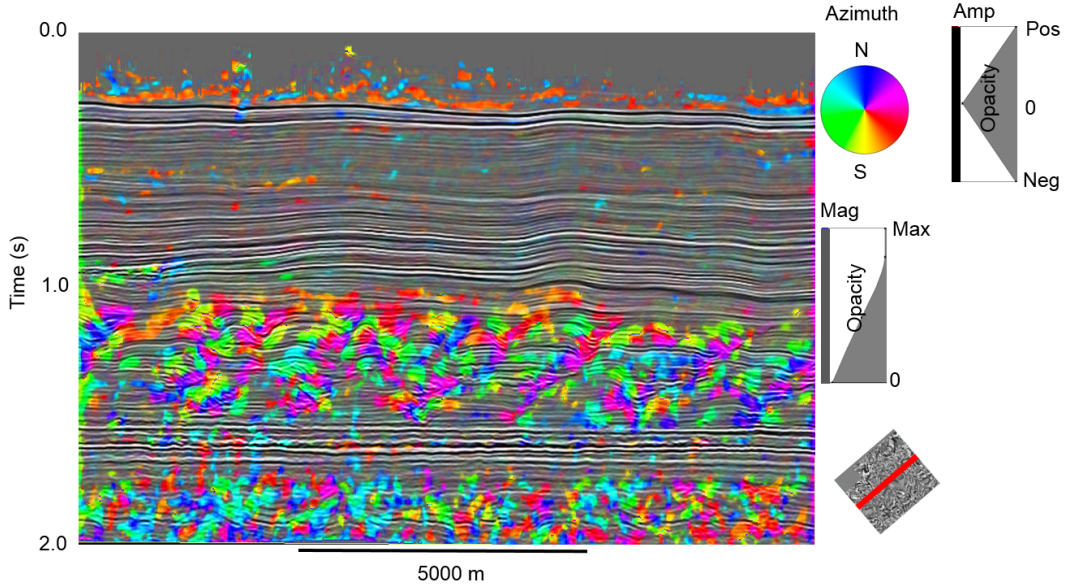


Figure 5.28: Reflector convergence azimuth and magnitude for a vertical line. The reflectors converge on the edges of the channel-forms as well as the flanks.

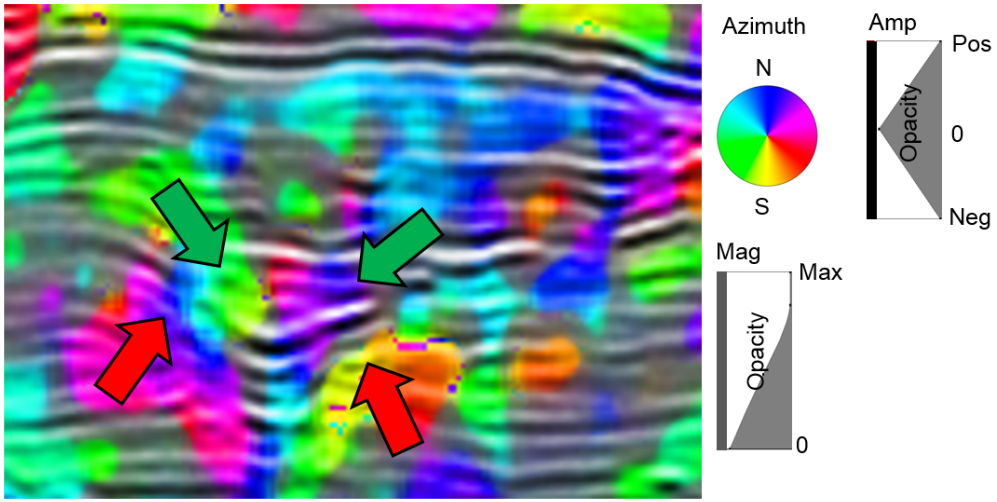


Figure 5.29: Reflector convergence azimuth and magnitude for a zoomed portion of a vertical line. Green arrows denote the convergence associated with the edges of the channel-forms. Red arrows show the convergence associated with the flanks.

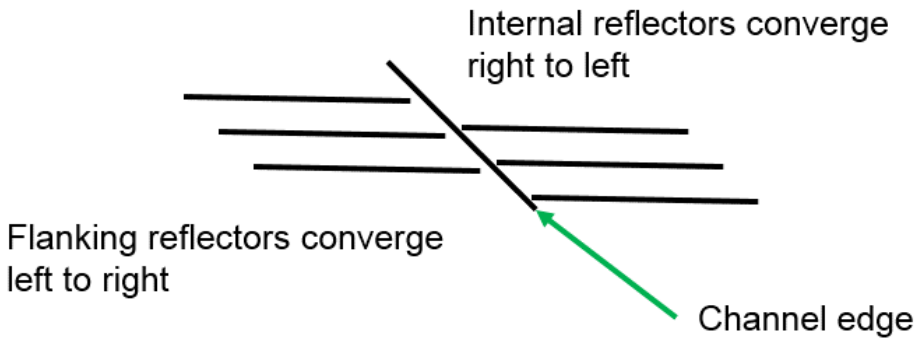


Figure 5.30: Reflectors on the flanks of an incised channel-form will tend to converge toward the edges.

The first step in the geobody extraction work-flow is the selection of attribute(s). In the previous section, I looked at a number of attributes, and I concluded that k2 curvature was the best candidate.

The next step in the geobody extraction work-flow is to select attribute parameters. While k2 curvature was a good candidate for geobody extraction, highly negative values did not extend fully across the lateral extent of the channel-forms. I took measurements of a number of channel-forms, and determined that 600 m was a typical lateral width for the channel-forms. I then constructed a spatial operator with a half wavelength of 600 m to use in the curvature calculation process. This operator is shown in Figure 5.32.

Using the spatial operator shown in Figure 5.33, I calculated k2 curvature for the extent of the Mandu formation (Figure 5.33). In this case, the highly negative values did a much better job extending across the full lateral extent of the channel-forms.

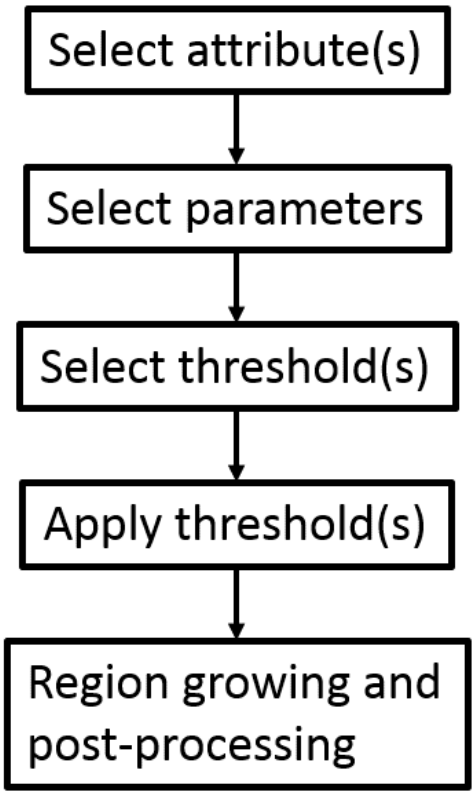


Figure 5.31: A typical geobody extraction work-flow.

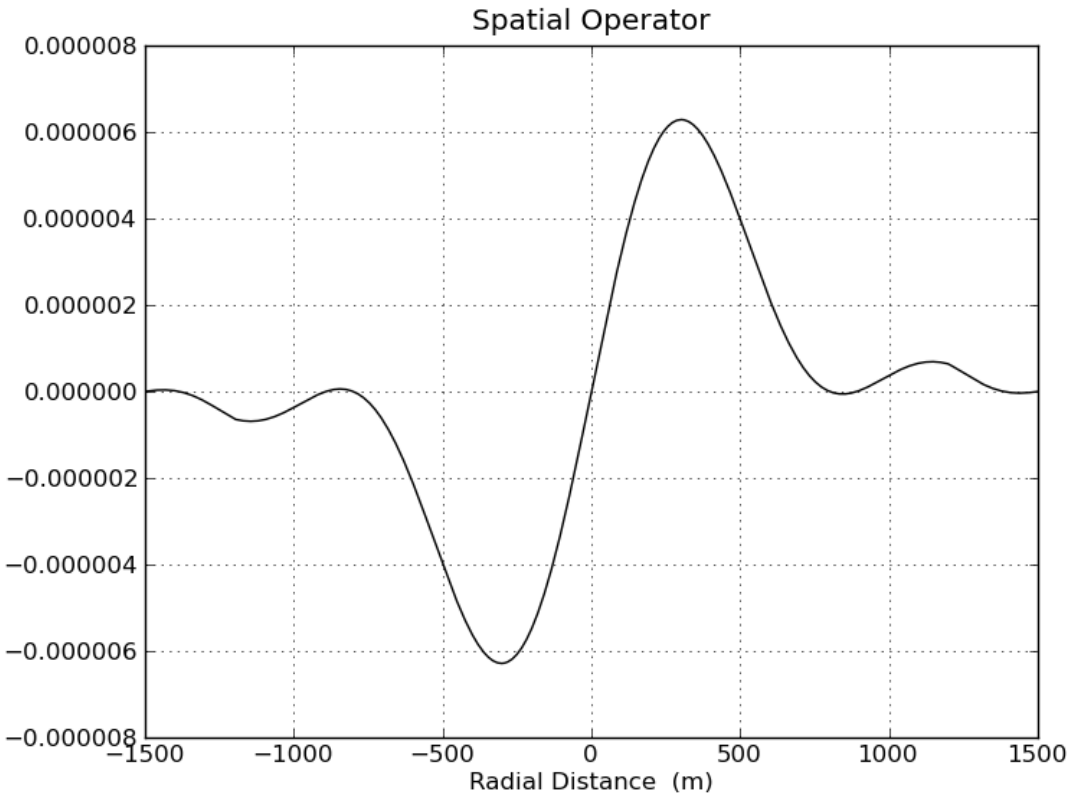


Figure 5.32: A spatial operator with a half wavelength of 600 m.

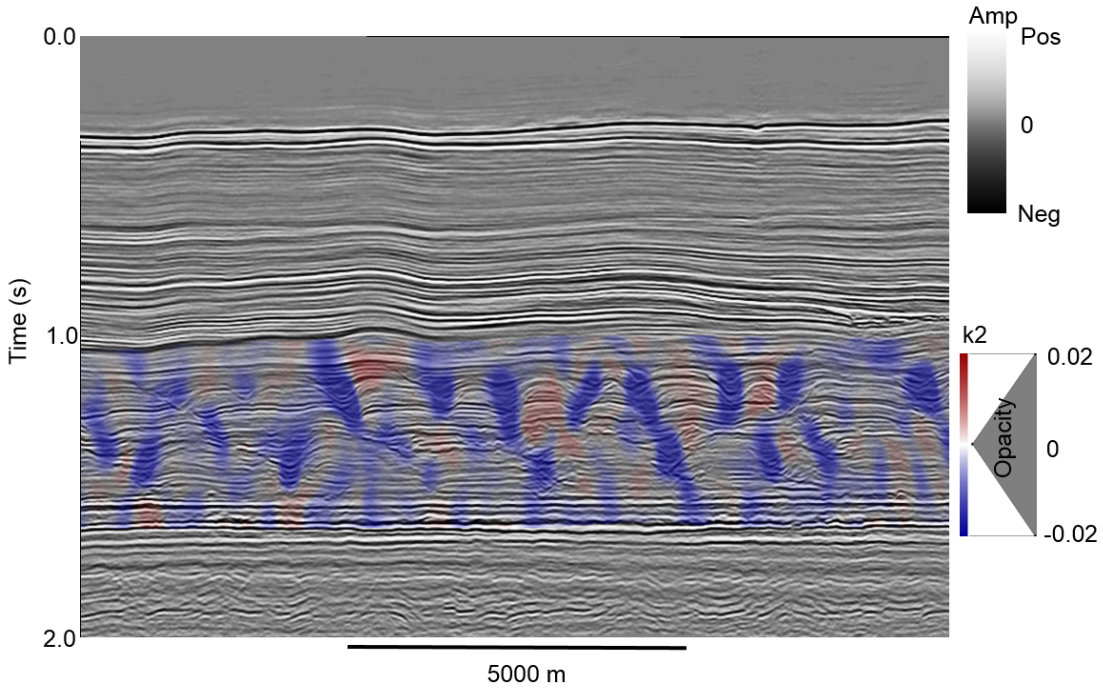


Figure 5.33: k2 curvature calculated using a spatial operator designed for 600 m wide features calculated for the extent of the Mandu formation. Highly negative values of k2 do a much better job of extending across the full lateral extent of the channel-forms. Note that several of the "interfluvials" or regions between the channel-forms have a dome shape which gives rise to a positive value (red) for k2.

Using the calculated k2 curvature shown in Figure 5.33, I then established a threshold to be used in the geobody extraction process (Figure 5.34).

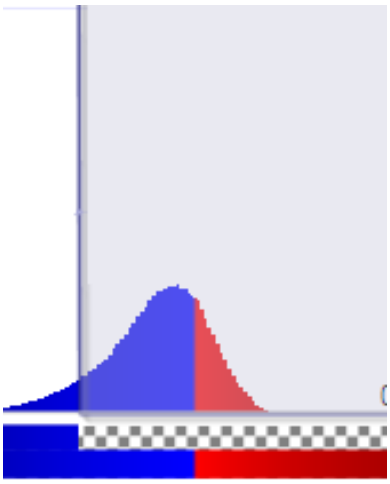


Figure 5.34: In the thresholding process, highly negative values of k2 curvature are assumed to correspond with the channel-forms.

Figure 5.35 shows the values that fell below the selected threshold. These results appear to well define the channel-forms and were thus used to continue the geobody extraction work-flow.

The final step of the geobody work-flow involves post-processing of the thresholded values. This step includes region growing to define objects and a post-processing step to reject objects that are too small in size. The results of this extraction process are shown in Figure 5.36. The extracted channel-forms appear to be geologically feasible, and correlate closely to the channel-forms seen by animating through a suite of EW vertical slices through the seismic amplitude data. This seems to confirm the viability of the use of k2 curvature for 3D geomodeling.

Figure 5.37 shows a representative intersection of the extracted geobodies with the seismic amplitude for the vertical line (Figure 5.13) used in the validation process. The geobodies in this slice have modeled every channel-form that is present in the

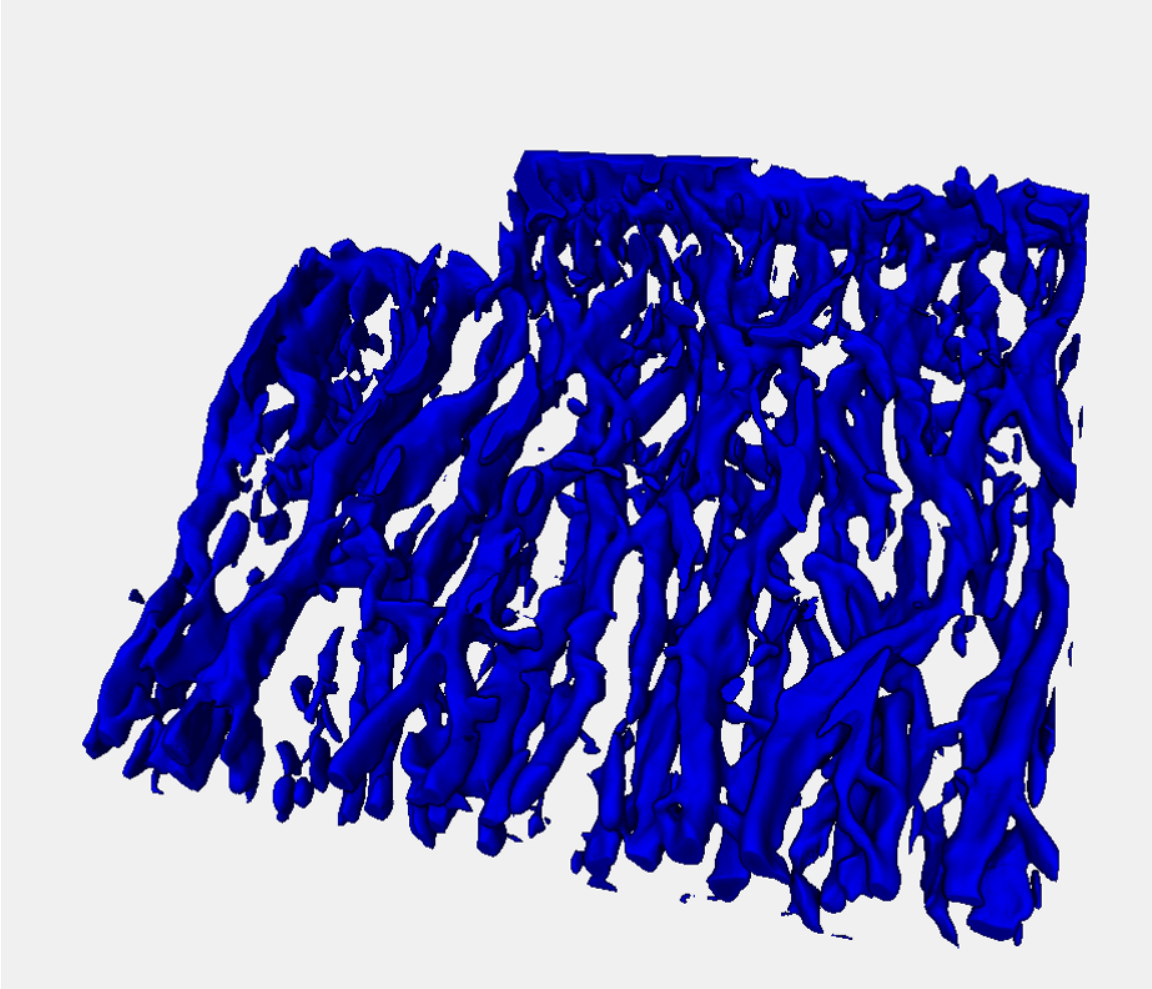


Figure 5.35: Values of k2 curvature below the selected threshold are candidates for inclusion in the geobody being extracted.

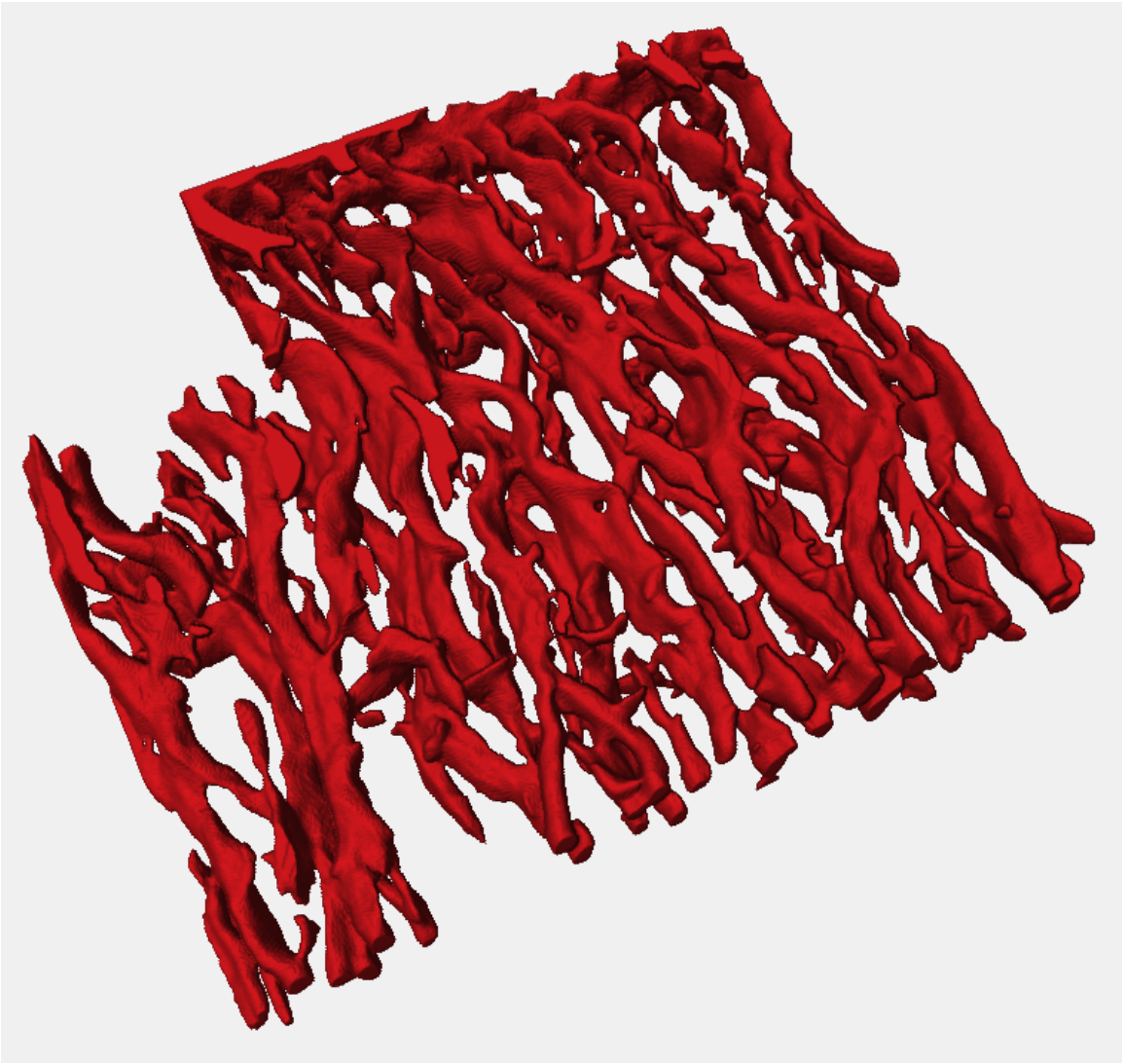


Figure 5.36: Extracted geobodies for the channel-forms modeled using k2 curvature. The results appear to be geologically feasible.

data. However, there were some additional small valley features that were extracted below the larger channel-forms that should not have been. Furthermore, as expected, the modeled geobodies to not cover the full crosswise extent of the channel-forms. The overall results are quite promising although further parameter tuning is necessary.

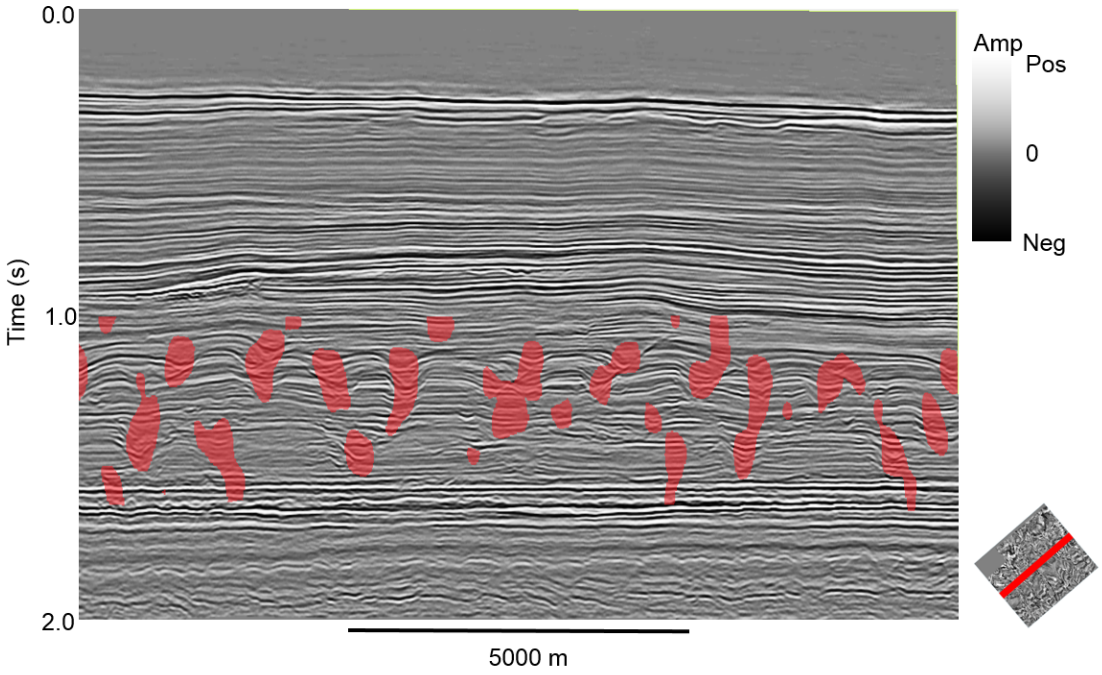


Figure 5.37: Extracted geobodies overlain on the seismic amplitude data.

5.6 Conclusions

In this chapter, I have examined the seismic attribute expression of channel-forms in a hybrid carbonate turbidite formation using a data set from the Carnarvon Basin, Australia. This formation is highly channelized, and mapping these channels through traditional seismic geomorphological methods is complicated by the difficulty in picking appropriate flattening horizons. Therefore, I have designed and implemented a more modern work-flow based on seismic attributes.

I have shown how these channel-forms are expressed by a number of seismic attributes including variance, principal curvature, and reflector convergence. These were picked due to articulable characteristics of the morphology of channels and channel like structures. I also used multi-attribute visualization to demonstrate the interaction and synergy of multiple attributes.

In my analysis, I found that k2 curvature was very effective in mapping the trough-like nature of the channel-forms. I then used this relationship to build 3D models of the channel-forms. I showed that this approach provided promising results in that it appeared to map all of the channel-forms. However, it did have a weakness in that it captured a small number of unwanted features. Furthermore, while it mapped the channel-forms, it did not provide complete coverage of their crosswise extent.

I have laid the groundwork for future work. Specifically, further tests could be employed to reject falsely mapped regions. Additionally, I would suggest using the extracted channel-form models as a starting point for heuristic analysis that would expand the models until the full extent was captured.

Carbonate turbidite systems are not as widely understood as the more traditional clastic turbidites, and there exist questions concerning how they are formed. Specifically, it is unknown during what timing of the system evolution they are formed. Accurate and complete modeling of these channel-forms should help to further study their nature, contributing to our understanding of carbonate turbidite systems.

CHAPTER 6

Conclusions

In this dissertation, I have examined a number of approaches to visualize fluvial-deltaic and turbidite systems using seismic attribute analysis. My main focus has been to develop methods to integrate a plethora of attributes. While I have used both objective and subjective approaches, my unifying goal has been to present the right image to the interpreter and to put my faith in his ability to make the right decision.

In chapter 2, I presented an innovative use of an alternate color mapping to simultaneously present both spectral phase and magnitude information. Traditional interpretation tends to focus upon spectral magnitude information because of a) the well understood nature of magnitude and b) the challenges presented by the circular nature of phase. I demonstrated that phase adds a richness of detail to the images allowing for interpretation of a complex range of architectural elements.

I also demonstrated the use of PCA with spectral phase and magnitude. Traditionally, this approach has only been applied to magnitude information. I showed how it was able to reduce the dimensionality of the problem. This was especially important since incorporating phase information precluded the simultaneous visualization of multiple spectral magnitude components. At the same time, I quantitatively demonstrated limitations of the PCA approach that are not well understood by the interpretation community.

In chapter 3, I presented an interactive method, IGT, for combining multiple spectral magnitude components. The goal of this work was to find an alternative to PCA that did not have the same weaknesses. This approached used the skill and expertise of the interpreter to decide how to best combine the spectral magnitude components to achieve the interpretation task at hand. I demonstrated that within the limitations of the approach that I could construct images with considerable interpretational value.

In chapter 4, I applied a statistical-based method to the problem of combining multiple attributes. The intent of this method was to provide an objective alternative to PCA. This approach avoided the linearity assumptions of both PCA and IGT. Unlike IGT, this technique was not interactive, making it not subject to the skill of the interpreter while also loosing the advantages associated with this difference.

In chapter 5, I analyzed the seismic attribute expression of a hybrid carbonate turbidite system. The goal of this work was to inform the interpreter of the strengths and weaknesses of a number of useful attributes to allow her to make the choice for herself. Unlike the previous sections of this dissertation, the work in this chapter was not limited to 2D interpretation of horizon slices. I looked at both single attributes individually as well as performing multi-attribute analysis.

My analysis concluded that the k2 curvature attribute provided considerable power in mapping the presented channel-forms. I then used this finding to use commercially available software to construct a 3D model of the channel-forms. I demonstrated that these models were very useful but also had limitations.

Having completed this work, I would like to make a number of recommendations for the future based upon my findings. These recommendations are as follows:

1. Interpreters should consider spectral phase when they interpret spectral decomposition attributes. The benefits of including this information outweighs the cost. As a community, we should develop tools for using HSV color maps to visualize seismic attributes.

2. PCA has strengths and weaknesses, but it is generally a very useful tool. Other tools should continue to be developed and considered, and all of these methods should be in the interpreters "toolbox".

3. IGT should be developed commercially and integrated into existing interpretations packages. It has capabilities not present in any other approach, and these should be captured.

4. Latent space modeling is a powerful tool that goes beyond PCA. While SOM is available in a number of commercial software products, GTM is not. GTM should also be included in these packages.

5. Additional work should be done upon the use of k2 curvature to model channels and channel-like features in 3-D.

6. Once a more robust approach to channel-form extraction is developed, the carbonate turbidite data set I used should be revisited. Modeling these channel-forms completely and accurately should contribute significantly to the understanding on how carbonate turbidite systems develop.

Finally, in addition to these specific conclusions and recommendations, my experiences in writing this dissertation have led me to a number of more general conclusions that I would like to share. These are as follows:

1. There is no single right attribute, approach, or view of the data. As an interpreter, you must have a rich "toolbox", and you must be prepared to use what

it takes to complete your task.

2. Images almost always look better on a computer display than they do on a printed page or a projected screen. Hence, in examining this dissertation, I encourage you to rely upon an electronic copy whenever possible.

3. As a community, we have accomplished a lot in seismic attribute analysis. However, there is much more work to be done.

Thank you for reading this dissertation to its completion. I hope you have enjoyed reading it as much as I've enjoyed writing it.

Bibliography

Andrews, D., 1972, Plots of high-dimensional data: Biometrics, **28**, 125–136.

Asimov, D., 1985, The grand tour: A tool for viewing multidimensional data: SIAM Journal on Scientific and Statistical Computing, **6**, 128–143.

Bahorich, M., A. Motsch, K. Laughlin, and G. Partyka, 2002, Amplitude responses image reservoir: Harts E&P, 59–61.

Bellman, R. E., 1957, Dynamic programming: Princeton University Press.

Bernet, K. H., G. P. Eberli, and A. Gilli, 2000, Turbidite frequency and composition in the distal part of the Bahamas transect: Proceedings of the Ocean Drilling Program, Scientific Results, 45–60.

Bishop, C. M., M. Svensén, and C. K. I. Williams, 1998, GTM: The Generative Topographic Mapping: Neural Computing, **10**, 215–234.

Braccini, E., and A. Adeyemi, 2011, Integrating seismic attributes for geo-modeling purposes: Nigeria deepwater turbidite environment case study: Presented at the Proceedings of the Gulf Coast Section of the Society for Sedimentary Geology.

Brown, A. R., 2011, Interpretation of three-dimensional seismic data: AAPG.

Buja, A., and D. Asimov, 1986, Grand tour methods: An outline: Presented at the Computer Science and Statistics: Proceedings of the Seventeenth Symposium on the Interface.

Castagna, J., and S. Sun, 2006, Comparison of spectral decomposition methonds: First Break, **24**, 75–79.

Castagna, J. P., S. Sun, and R. W. Siegfried, 2003, Instantaneous spectral analysis: Detection of low-frequency shadows associated with hydrocarbons: The Leading Edge, **32**, 120–127.

Cathro, D. L., J. A. Austin, and G. D. Moss, 2003, Progradation along a deeply submered Oligocen-Miocene heterozoan carbonate shelf: How sensitive are clinoforms to sea level variations?: AAPG Bulletin, **87**, 1547–1574.

Chaveste, A., 2003, Risk reduction in estimation of petrochemical properties from seismic data through well-log monitoring, seismic modeling, and rock properties estimation: The Leading Edge, **22**, 406–418.

Chernoff, H., 1973, Using faces to represent points in k-dimensional space graphically: Journal of the American Statistical Association, **68**, 361368.

Chopra, S., and K. J. Marfurt, 2006, Seismic attributes - A promising aid for geologic prediction: CSEG Recorder, 110–121.

Coléou, T., M. Poupon, and K. Azbel, 2003, Interpreter's Corner-Unsupervised seismic facies classification: A review and comparison of techniques and implementation: The Leading Edge, **22**, 942.

Davogustto, O., M. C. de Matos, C. Cabarcas, T. Dao, and K. J. Marfurt, 2013, Resolving subtle stratigraphic features using reservoir ridges and phase residues:

Interpretation, **1**, SA93–SA108.
Davogustto, O., B. Dowdell, S. Guo, J. T. Kwiatkowski, K. J. Marfurt, A. Roy, S. Verma, and B. Zhang, 2011, Running AASPI software with GUIs: Technical report, University of Oklahoma.
Del Moro, Y., A. Fernandez Abad, and K. J. Marfurt, 2013, Why should we pay for a merged survey that contains the data we already have? An Oklahoma Red Fork example: The Shale Shaker, **63**, 336–357.
Deptuck, M. E., 2003, Post-rift geology of the Jeanne DArc basin, with a focus on the architecture and evolution of early Paleogene submarine fans, and insights from modern deep-water systems: PhD thesis, Dalhousie University.
El-Mowafy, H., and K. J. Marfurt, 2008, Structural interpretion of the Middle Frio Formation using 3D seismic and well logs: An example from the Texas Gulf Coast of the United States: The Leading Edge, **27**, 840–854.
Elis, Y. O., 2011, Effect of prestack processing flows on acquisition footprint as seen on geometric attributes: The Red Fork Formation case study: Master's thesis, The University of Oklahoma.
Guo, H., K. J. Marfurt, J. Liu, and Q. Duo, 2006, Principal component analysis of spectral components: 76th Annual International Meeting of the SEG, **25**, 988–992.
Harris, P. M., and R. P. Wright, 1998, Reservoir protential of the carbonate forereef-slope setting: Presented at the AAPG international conference and exhibition.
Heath, R. S., and M. C. Apthorpe, 1984, New formation names for the late cretaceous and tertiary sequence of the southern north west shelf: Technical Report Record 1984/7, Geological Survey of Western Australia.
Jackson, J. E., 2003, A user's guide to principal components: Wiley.
Kirkland, F., and W. W. Newcomb, 1967, The rock art of Texas Indians: The University of Texas Press.
Kohonen, T., 2001, Self-organizing maps: Springer.
Laake, A., and B. C. Wallet, 2013, Improved salt body delineation using a new structure extraction workflow: Presented at the 75th EAGE Conference & Exhibition.
Lafon, S. S., 2004, Diffusion maps and geometric harmonics: PhD thesis, Yale University.
Leppard, C., A. Eckersley, and S. Purves, 2010, Quantifying the temporal and spatial extent of depositional and structural elements in 3D seismic data using spectral decomposition and multi attribute RGB blending: Presented at the Gulf Coast Section of the SEPM.
Liu, J., and K. J. Marfurt, 2005, Matching-pursuit decomposition using morlet wavelets: SEG Technical Program Expanded Abstracts, **24**, 786–789.
———, 2007a, Instantaneous spectral attributes to detect channels: Geophysics, **72**, P23–P31.
———, 2007b, Multicolor display of spectral attributes: The Leading Edge, **26**, 268–271.
Mai, H. T., K. J. Marfurt, and S. Chávez-Pérez, 2008, Coherence and volumetric curvatures and their spatial relationship to faults and folds, an example from Chicontepec Basin, Mexico: SEG.
Manolakis, D., C. Siracusa, and G. Shaw, 2001, Hyperspectral subpixel target detec-

tion using the linear mixing model: IEEE Transactions on Geoscience and Remote Sensing, **39**, 1392–1409.

Marfurt, K. J., and R. L. Kirlin, 2001, Narrow-band spectral and thin-bed tuning: Geophysics, **66**, 1274–1283.

Marfurt, K. J., R. L. Kirlin, S. Farmer, and M. S. Bahorich, 1998, 3-d seismic attributes using a semblance-based coherency algorithm: Geophysics, **63**, 1150–1165.

Marfurt, K. J., and J. Rich, 2010, Beyond curvature - volumetric estimates of reflector rotation and convergence: SEG Technical Program Expanded Abstracts.

McLachlan, G. J., 2008, The EM algorithm and extensions: Wiley-Interscience.

Moore, C. H., 2001, Carbonate reservoirs porosity evolution and diagenesis in a sequence stratigraphic framework: Elsevier.

Mullins, H. T., K. C. Heath, H. M. V. Buren, and C. R. Newton, 1984, Anatomy of a modern open-ocean carbonate slope: Northern Little Bahama Bank: Sedimentology, **31**, 141–168.

Myer, D. E., E. L. Harvey, T. E. Bulloch, J. C. Voncannon, and T. M. Sheffield, 2001, Use of seismic attributes in 3-d geovolume interpretation: SEG Technical Program Expanded Abstracts.

Partyka, G., J. Gridley, and J. Lopez, 1999, Interpretational applications of spectral decomposition in reservoir characterization: The Leading Edge, **18**, 353–360.

Peyton, L., R. Bottjer, and G. Partyka, 1998, Interpretation of incised valleys using new 3-d seismic techniques: A case history using spectral decomposition and coherency: The Leading Edge, **17**, 1294–1298.

Posamentier, H. W., 2006, Seismic geomorphology: imaging elements of depositional systems from shelf to deep basin using 3D seismic data: implications for exploration and development: Presented at the 3D Seismic Technology: Application to the Exploration of Sedimentary Basins.

Priebe, C. E., 1994, Adaptive mixtures: Journal of the American Statistical Association, **89**, 796–806.

Richardson, M. J., 2000, Rosie 2D & 3D seismic interpretation report: Technical report, Woodside Energy Limited.

Slatt, R. M., 2014, Stratigraphic reservoir characterization for petroleum geologists, geophysicists, and engineers: Elsevier.

Stockwell, R. G., R. P. Lowe, and L. Mansinha, 1997, Instantaneous wave-vector analysis: Presented at the Wavelets IV.

Suarez, Y., K. J. Marfurt, and Mark, 2008, Seismic attribute-assisted interpretation of channel geometries and infill lithology: A case study of Anadarko Basin Red Fork channels: SEG Technical Program Expanded Abstracts, **27**, 963–967.

Symanzik, J., B. C. Wallet, and W. Shannon, 2007, The image grand tour for exploring medical images: Presented at the 2007 Proceedings of the American Statistical Association, Statistical Graphics Section [CD-ROM].

Symanzik, J., E. J. Wegman, A. J. Braverman, and Q. Luo, 2002, New applications of the image grand tour: Presented at the Computer Science and Statistics: Proceedings of the 34th Symposium on the Interface.

Titterington, D. M., A. F. M. Smith, and U. E. Makov, 1985, Statistical analysis of finite mixture models: Wiley.

Vail, P. R., R. M. Mitchem, and S. Thompson, 1977, Seismic stratigraphy and global changes of sea level, part 2. The depositional sequence as a basic unit for stratigraphic analysis., *in* Seismic Stratigraphy: Applications to hydrocarbon exploration: AAPG Memoirs, 53–62.

Wallet, B. C., 2008, Visualizing spectral decomposition using the view locked color image grand tour: SEG Technical Program Expanded Abstracts, **27**, 894–898.

———, 2013, Using the image grand tour to visualize fluvial deltaic architectural elements in south Texas, USA: Interpretation, **1**, SA117SA129.

Wallet, B. C., V. Aarre, A. Davids, T. Dao, and K. J. Marfurt, 2011, Using a hue-saturation color map to visualize dewatering faults in the overburden of the Hod Field, North Sea: SEG Technical Program Expanded Abstracts, **30**.

Wallet, B. C., O. Davogustto, R. Daber, and K. J. Marfurt, 2012, Using an HSV color map to visualize spectral phase and magnitute information for an incised valey system in the Anadarko Basin, Oklahoma, USA: SEG.

Wallet, B. C., M. C. de Matos, J. T. Kwiatkowski, and Y. Suarez, 2009, Latent space modeling of seismic data: An overview: The Leading Edge, **28**, 1454–1459.

Wallet, B. C., D. J. Marchette, and J. L. Solka, 1997, Using genetic algorithms to search for optimal projections: Presented at the Automatic Target Recognition VII.

Wallet, B. C., and K. J. Marfurt, 2008, A grand tour of multispectral components: A tutorial: The Leading Edge, **27**, 334–341.

Wallet, B. C., and R. Perez, 2009, Clustering bed sets from the Barnett Shale using diffusdif map attributes: SEG Technical Program Expanded Abstracts.

Wegman, E. J., 1992, The grand tour in k-dimensions: Presented at the Computer Science and Statistics: Proceedings of the 24th Symposium on the Interface.

Wegman, E. J., W. L. Poston, and J. L. Solka, 1998, Image grand tour: Automatic Target Recognition VIII - Proceedings of SPIE, 286–294.

Wegman, E. J., and J. Shen, 1993, Three-dimensional Andrews plots and the grand tour: Presented at the Computer Science and Statistics: Proceedings of the 25nd Symposium on the Interface.

Weimer, P., and R. M. Slatt, 2006, Introduction to the petroleum geology of deepwater settings: AAPG studies in geology: AAPG.

Zhang, K., K. J. Marfurt, R. M. Slatt, and Y. Guo, 2009, Spectral decomposition illumination of reservoir facies: Presented at the 78th Annual International Meeting of the SEG.

APPENDIX A

The Curse of Dimensionality

The curse of dimensionality refers to the intractable nature of data modeling and probability density estimation in high dimensional space. This was first observed by Bellman (1957), and it is based upon the fact that fact that as the dimension of an attribute space grows, observations rapidly become sparse in terms of their generating probability mass, i.e. observations become infinitely far apart.

A.1 Geometric Analogy

One way of considering what occurs in high dimensional space is to consider a shape contained within another shape in a multi-dimensional space as the dimensions goes to infinity. As I will show, increasingly the volume of the larger shape goes to the far margins.

The implication of this is that given observations drawn from a distribution with one observation x selected at random, the difference between the distance from x to the closest observation, $\delta_{\min}$, and the distance from x to the furthest observation, $\delta_{\max}$, relative to $\delta_{\min}$ goes to 0 as the dimension grows. This can be expressed as

$$\lim_{d \to \infty} \frac{\delta_{\max} - \delta_{\min}}{\delta_{\min}} \longrightarrow 0. \tag{A.1.1}$$

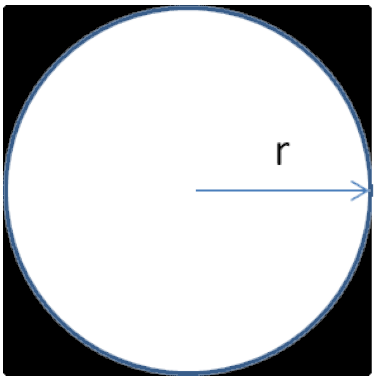


Figure A.1: A two-dimensional example of a hypersphere circumscribed within a hypercube. Any space within the hypercube that is not also within the hypersphere is contained within the corner regions.

where d is the dimension. The implication of this is that distance measures lose their meaning in high dimensional spaces.

Hypercube

There are two standard calculations that are frequently used to understand why this occurs. The first of these involves considering a d-dimensional hypersphere circumscribed within a d-dimensional hypercube (Figure A.1). The volume of a d-dimensional hypercube with sides of length $2r$ is $(2r)^d$, and the volume of a d-dimensional hypersphere with radius r is

$$\frac{2r^d\pi^{\frac{d}{2}}}{d\Gamma(\frac{d}{2})} \tag{A.1.2}$$

where Γ is the Gamma function defined by

$$\Gamma(z) = \int_0^\infty t^{(z-1)}e^{-t}\,dt. \tag{A.1.3}$$

Given this, the volume of the hypersphere relative to the hypercube is

$$\frac{\frac{2r^d\pi^{\frac{d}{2}}}{d\Gamma(\frac{d}{2})}}{(2r)^d} \tag{A.1.4}$$

which leads to

$$\lim_{d\to\infty} \frac{\pi^{\frac{d}{2}}}{d2^{d-1}\Gamma(\frac{d}{2})} \longrightarrow 0. \tag{A.1.5}$$

Therefore, in this model, as the dimensionality grows to infinity, all of the space within the hypercube occurs in the distant margins defined by the corners.

Hypersphere

The second way to poise the curse of dimensionality geometrically is to consider a hypersphere of radius r containing a hypersphere of radius $r - \epsilon$ (Figure A.2). In this manner, the difference in the radii of the two hyperspheres can be taken to be arbitrarily small. Using Equation A.1.2, the relative volume of the smaller hypersphere to the larger is

$$\lim_{d\to\infty} (\frac{r-\epsilon}{r}) \longrightarrow 0. \tag{A.1.6}$$

Therefore, in this model, as the dimensionality grows to infinity, all of the space within a hypersphere occurs in an arbitrarily thin shell.

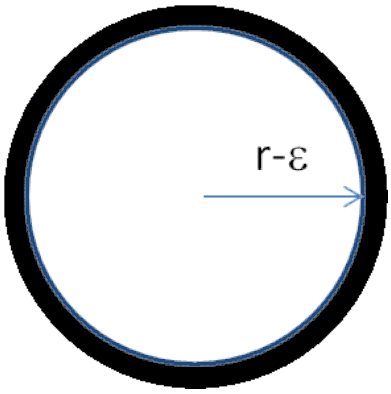


Figure A.2: A two-dimensional example of a hypersphere contained within a hypersphere of ϵ larger radius. Any space within the larger hypersphere that is not also within the smaller hypersphere is contained within within a thin shell.

A.2 Practical Implications

The sparseness of high dimensional space has profound implications upon the analysis of multiattribute data when modeling and clustering. To understand the implications for modeling, consider a multivariate Gaussian distribution in a high dimensional space. In this case, the curse of dimensionality means that all probability mass is thus at the "edges", aware from the center or mean of the distribution. In practical terms, this means that all observations are outliers and thus unreflective of the underlying process being modeled. The implications of this is that attempting to construct a classifier with a large number of attributes is statistically impossible.

One should also consider the implications upon clustering in high dimensions. In this case, the probability mass near any observation is effectively zero, and we could thus expect to find no other observations "near" any others. Therefore, when attempting to construct a classifier or cluster with many attributes, it is necessary to somehow reduce the dimensionality.

APPENDIX B

Visualization of High Dimensional Data

B.1 Cross plots

Scatter plots, frequently know in the geophysics community as cross plots, are a workhorse in multi-attribute analysis. They have successfully been used in analysizing many types of geophysical data including seismic attribute Chopra and Marfurt (2006) and well log analysis Chaveste (2003). Scatter plots are the canonical method for visualizing data when the only topological consideration is the structure of the attribute space, and they are supported by virtually all data visualization and analysis packages. Scatter plots can be further expanded using color or plotting character; such methods are often used to incorporate such information as data class. Traditionally, scatter plots can only be used visualize data in two or possibly three dimensions. In pairs plots (Figure B.1), all possible pair-wise combinations of the attributes are plotted allowing for d-dimensional visualization; however such data are still only visualized in two attribute combinations.

B.2 Parallel coordinates

To effectively visualize more than three dimensions, we can use non-Euclidean geometries. Parallel coordinates plots Wegman (1992) display data using a projective

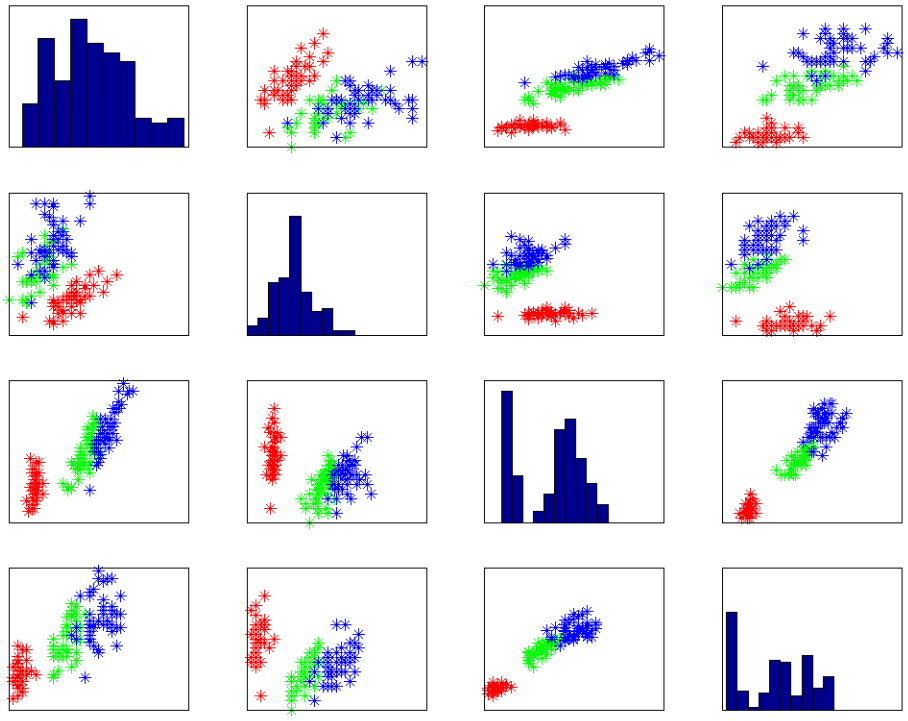


Figure B.1: A pairs plot shows all scatter or crossplots of all attributes displayed pair-wise. The center axis shows the histogram of the individual attributes. In this particular case, the data are fourdimensional with three classes. Color denotes class membership.

geometry in which coordinates are parallel rather than orthogonal. An example parallel coordinates plot is shown in Figure B.2. Since adding a dimension is simply a process of adding another axis parallel to the previous axes, parallel coordinates can be expanded to an arbitrary number of dimensions, though practical considerations regarding screen resolution do serve as a limiting factor.

Parallel coordinates shows a number of interesting dualities including the fact that lines in the Euclidean space are inter-axial points of co-incidence in parallel coordinate space. This however illustrates the major limitations of parallel coordinates. Firstly, the view shown by parallel coordinates is order dependent, based upon how one

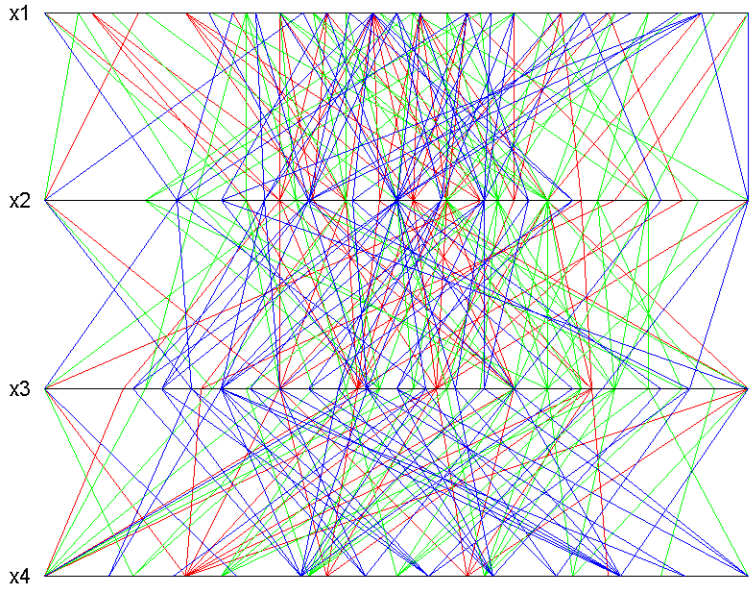


Figure B.2: A parallel coordinates plot makes the axes parallel instead of orthogonal. Each observation is thus encoded as a piecewise linear curve. In this particular case, the data are four dimensional with three classes. Color denotes class membership.

chooses to arrange the axes. Furthermore, seeing structure in more than a pair-wise fashion is difficult, and even then, this capability is limited by the ordering of the axes.

B.3 Andrews' curves

One means of plotting observations in non-Euclidean space is Andrews' curve plots Andrews (1972) which encode the observations as the coefficients of a Fourier transform plotted on the range of [-π, π]. As with parallel coordinates plot, each observation is represented as a curve, but the curve is smooth instead piecewise linear.

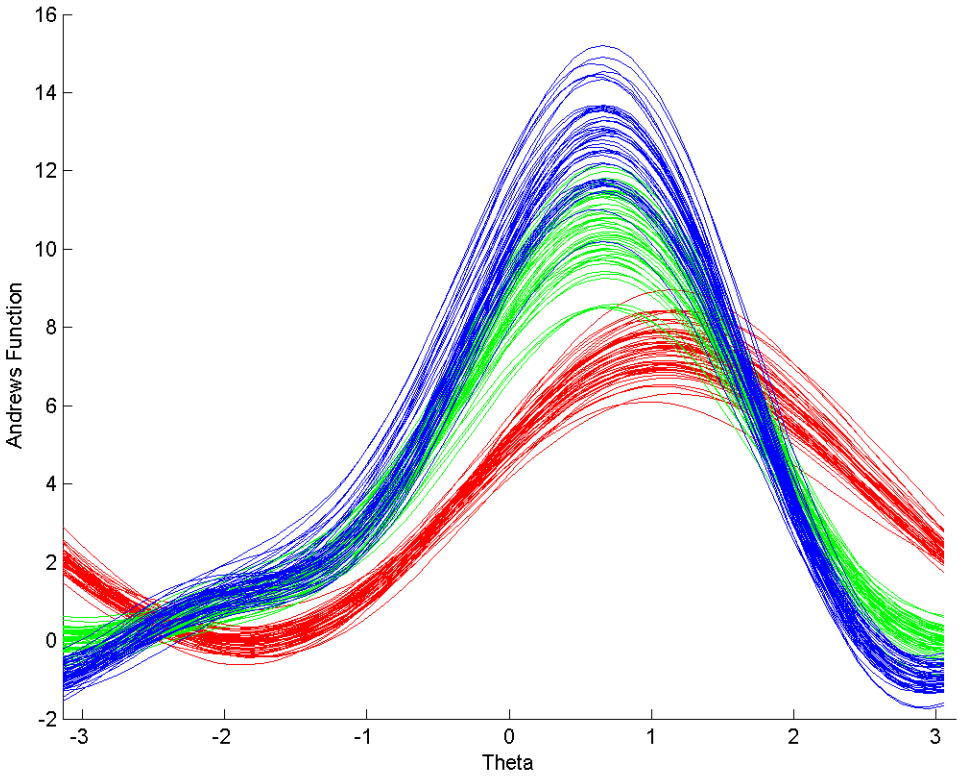


Figure B.3: Andrews curves encode multidimensional attributes as the coefficients of a Fourier series. In this particular case, the data are four dimensional with three classes. Color denotes class membership.

An example Andrews curve plot is shown in Figure B.3. Also, as with parallel coordinates, Andrews' curve plots are attribute-order dependent. Andrews' coordinate plots lack the duality of parallel coordinates plots and thus they are not as useful for examining higher dimensional structure. However, the Andrews' curves plots are more globally oriented and are thus more powerful for clustering.

B.4 Chernoff faces

Chernoff faces Chernoff (1973) is another multivariate visualization method developed to facilitate visual clustering. The idea behind Chernoff faces is to exploit the

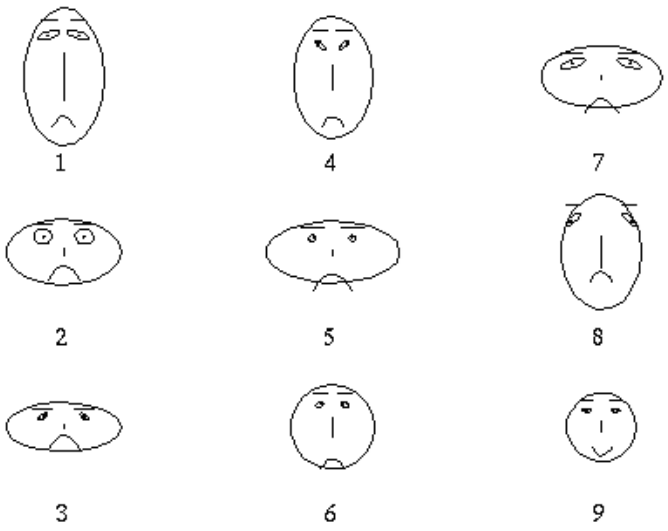


Figure B.4: Chernoff faces plots encode each d-dimensional observation as a face with each of d attributions defining the shape or size of a particular feature of the face.

human brain's expertise in facial recognition. In Chernoff faces, each observation is represented as an individual cartoon of a human face. Each attribute is encoded as a portion of the face such as nose length, face obliquity, and mouth expression. An example Chernoff face plot is shown in Figure B.4. While Chernoff faces are an interesting approach, in practice, other methods are generally better at presenting the same information.

B.5 Summary

The above methods are far from an exhaustive list of ways to graphically present multi-attribute (multivariable) data. They do, however, give a feel for the broad range of methods that are widely used for exploratory data analysis (EDA). As previously noted, all of these methods have a limitation in their applicability for seismic data in that they completely ignore the inherent lattice nature of the problem.